2006.2.7

Study of the CP violation angle ϕ_3 using DK decay modes of B meson

Department physics, Tohoku Univercity
Naoki Kikuchi

Abstract

In this thesis, I report the study of $B \to DK$ decay, using a data sample of 366 million $B\bar{B}$ pairs recorded at the $\Upsilon(4S)$ resonance with the Belle detector at the KEKB asymmetric e^+e^- storage ring. Several suppressed $B \to DK$ decays are measured. And the constraints for ϕ_3 by these measurements are discussed.

Contents

Chapter 1

Introduction

CP violation in the standard model is explained by Cabibbo-Kobayashi-Masukawa model. Its effects are able to be parametalized by unitarity triangle on $\rho-\eta$ plane. These angels and sides are related to physics process which fortunately appear in B decays. So measurements of these are the precise test for the standard model(SM).

1.1 CKM model

The violation of symmetry between matter and anti-matter attract many physicists and had not be able to solve. But Kobayashi and Maskawa solve that problem by introducing 6 quarks of 3 generations within the SM framework.

The interaction lagrangian is given by

$$\mathcal{L}_{int}(x) = -\frac{g}{\sqrt{2}}\overline{\mathcal{U}_{L,i}}\gamma^{\mu}V_{CKM,ij}\mathcal{D}_{L,j}W_{\mu} + h.c.$$

where

$$\bar{\mathcal{U}} = \begin{pmatrix} u & c & t \end{pmatrix}, \mathcal{D} = \begin{pmatrix} d \\ s \\ b \end{pmatrix}$$

, subscript L means light-handed part of these quark states, and

$$V_{CKM} = \begin{pmatrix} V_{ud} & V_{us} & V_{ub} \\ V_{cd} & V_{cs} & V_{cb} \\ V_{td} & V_{ts} & V_{tb} \end{pmatrix}.$$

In the above formalism quark states are states which diagonalize electro-weak interaction. But generally mass eigenstates($\acute{\mathcal{U}}$ and $\acute{\mathcal{D}}$) differs from them and are given by

$$\acute{\mathcal{U}} = U_u{}^{\dagger}\mathcal{U},\ \acute{\mathcal{D}} = U_d{}^{\dagger}\mathcal{D}$$

and U is related to V_{CKM} through

$$V_{CKM} = {U_u}^{\dagger} U_d$$

which gives quark-mixing.

There are many parameterization methods which define relative quark phase of V_{CKM} matrix elements. One of popular approximation methods is that of Wolfenstein which is

$$V_{CKM} = \begin{pmatrix} 1-\frac{\lambda^2}{2} & \lambda & A\lambda^3(\rho - i\eta) \\ -\lambda & 1-\frac{\lambda^2}{2} & A\lambda^2 \\ A\lambda^3(1-\rho-i\eta) & -A\lambda^2 & 1 \end{pmatrix} \tag{1.1}$$

where λ, A, ρ and η are real parameter. In this parametarization λ is Cabibo-supression-factor and related to Cabibo angle as

$$\lambda \equiv \sin\theta_c$$

λ and A are experimentally well measured. But ρ and η have not been measured with accurately. So its measurements is main subject of B-factory experiment, Belle and BaBar.

In the SM, CKM matrix should be unitary for probability conservation law. The orthogonality of d-column and b-column lead to a relation as

$$V_{ud}V_{ub}^* + V_{cd}V_{cb}^* + V_{td}V_{tb}^* = 0.$$

Since terms are generally complex numbers, this relation can be represented as a triangle in a complex plane. Usually the triangle is defined as bellow

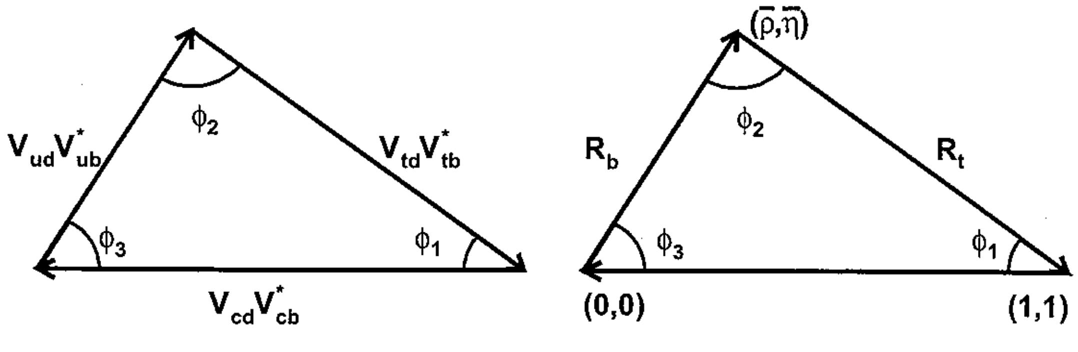

Figure 1.1: Unitarity triangle

where

$$\phi_1 \equiv \pi - \arg(\frac{V_{td}V_{tb}^*}{V_{cd}V_{cb}^*})$$

$$\phi_2 \equiv \arg(\frac{V_{td}V_{tb}^*}{-V_{ud}V_{ub}^*})$$
$$\phi_3 \equiv \arg(\frac{V_{ud}V_{ub}^*}{-V_{cd}V_{cb}^*}).$$

If Wolfenstein parametarization is used that converts to the triangle on $\rho - \eta$ plane as shown in Figure 1.1(right) where

$$\bar{\rho} \equiv (1 - \frac{\lambda^2}{2})\rho \tag{1.2}$$
$$\bar{\eta} \equiv (1 - \frac{\lambda^2}{2})\eta. \tag{1.3}$$

and sides are represented as

$$R_b \equiv \sqrt{\bar{\rho}^2 + \bar{\eta}^2} \tag{1.4}$$
$$R_t \equiv \sqrt{(1-\bar{\rho})^2 + \bar{\eta}^2}. \tag{1.5}$$

All these elements are determined from B decays such as shown in Table 1.1.

elements		decay mode
	ϕ_1	$B^0 \to J/\psi K^0$
angle	ϕ_2	$B^0 \to \pi^+\pi^-$
	ϕ_3	$B^- \to DK^-$
	V_{td}	$B \to \rho\gamma$
slide	V_{ub}	$B \to X_u l\nu$
	V_{cb}	$B \to X_c l\nu$

Table 1.1: Relationship between CKM elements and B decays

1.1.1 $B^0 - \bar{B}^0$ mixing and Time-dependent CP violation

Assuming a time-evolutions of state are given by only linear-convination of basis, B^0 and $\bar{B}^0$, it should be written as

$$i\frac{d}{dt}\begin{pmatrix} B^0 \\ \bar{B}^0 \end{pmatrix} = H\begin{pmatrix} B^0 \\ \bar{B}^0 \end{pmatrix} = \begin{pmatrix} H_{11} & H_{12} \\ H_{21} & H_{22} \end{pmatrix}\begin{pmatrix} B^0 \\ \bar{B}^0 \end{pmatrix}$$

Assuming the eigenstes of H are

$$B_H = pB^0 + q\bar{B}^0$$

$$B_L = pB^0 - q\bar{B}^0$$

and their eigenvalues are

$$\lambda_H = m_H - i\frac{\gamma_H}{2}$$
$$\lambda_L = m_L - i\frac{\gamma_L}{2}.$$

Then their time-evolution are given by

$$i\frac{d}{dt}B_{H,L} = \lambda_{H,L}B_{H,L} \quad (1.6)$$
$$\to B_{H,L}(t) = e^{-i\lambda_{H,L}t}B_{H,L}(0) \quad (1.7)$$

and these can be converted to

$$B^0 = \frac{1}{2p}(B_H + B_L) \to B^0(t) \equiv \frac{1}{2p}(e^{-i\lambda_H t}B_H + e^{-i\lambda_L t}B_L) \quad (1.8)$$
$$\bar{B}^0 = \frac{1}{2q}(B_H + B_L) \to B^{\bar{0}}(t) \equiv \frac{1}{2q}(e^{-i\lambda_H t}B_H - e^{-i\lambda_L t}B_L) \quad (1.9)$$

and

$$B^0(t) = \frac{1}{2}[(e^{-i\lambda_H t} + e^{-i\lambda_L t})B^0 + \frac{q}{p}(e^{-i\lambda_H t} - e^{-i\lambda_L t})\bar{B}^0] \quad (1.10)$$
$$\overline{B^0(t)} = \frac{1}{2}[(e^{-i\lambda_H t} + e^{-i\lambda_L t})B^0 + \frac{p}{q}(e^{-i\lambda_H t} - e^{-i\lambda_L t})\bar{B}^0]. \quad (1.11)$$

In this line if we assume $\gamma_H \simeq \gamma_L \simeq \gamma$,

$$\bar{m} \equiv \frac{m_H + m_L}{2}, \qquad \delta m \equiv m_H - m_L \quad (1.12)$$
$$\to e^{-i\lambda_H t} \pm e^{-i\lambda_L t} = e^{-imt}e^{-\frac{\gamma}{2}t}(e^{-i\frac{\delta m}{2}t} \pm e^{i\frac{\delta m}{2}t}) \quad (1.13)$$
$$= e^{-imt}e^{-\frac{\gamma}{2}t}\begin{pmatrix} 2\cos\frac{\delta m}{2}t \\ -2i\sin\frac{\delta m}{2}t \end{pmatrix} \quad (1.14)$$

$$B^0(t) = e^{-\frac{\gamma}{2}t}(B^0\cos\frac{\delta m}{2}t - i\frac{q}{p}\bar{B}^0\sin\frac{\delta m}{2}t) \quad (1.15)$$
$$\overline{B^0(t)} = e^{-\frac{\gamma}{2}t}(\bar{B}^0\cos\frac{\delta m}{2}t - i\frac{p}{q}B^0\sin\frac{\delta m}{2}t) \quad (1.16)$$

This shows $B^0 - \bar{B}^0$ mixing.

Next let's consider time-dependent CP violation. In this case we assume B^0 and $\bar{B}^0$ decay to same final state

$$A \equiv < f|H|B^0 > \quad (1.17)$$
$$\bar{A} \equiv < f|H|\bar{B}^0 > . \quad (1.18)$$

Then the amplitude of B^0 decay to f in t, $A_{B^0\to f}(t)$, is given by

$$A_{B^0\to f}(t) = e^{-\frac{\gamma}{2}t}(A\cos\frac{\delta m}{2}t - i\frac{q}{p}\bar{A}\sin\frac{\delta m}{2}t) \quad (1.19)$$
$$= Ae^{-\frac{\gamma}{2}t}(\cos\frac{\delta m}{2}t - i\rho\bar{A}\sin\frac{\delta m}{2}t) \quad (1.20)$$
$$A_{\bar{B}^0\to f}(t) = e^{-\frac{\gamma}{2}t}(\bar{A}\cos\frac{\delta m}{2}t - i\frac{p}{q}A\sin\frac{\delta m}{2}t) \quad (1.21)$$
$$= \bar{A}e^{-\frac{\gamma}{2}t}(\cos\frac{\delta m}{2}t - i\rho^{-1}\sin\frac{\delta m}{2}t) \quad (1.22)$$

where

$$\rho \equiv \frac{q\bar{A}}{pA}.$$

We define

$$A \equiv \frac{|\rho|^2-1}{|\rho|^2+1}, S \equiv \frac{2\text{Im}\rho}{|\rho|^2+1}$$

and then decay rates are calculated as

$$\Gamma_{B^0\to f} = \frac{|A|^2}{2}(|\rho|^2+1)e^{-\gamma t}[1 - A\cos\delta mt + S\sin\delta mt] \quad (1.23)$$
$$\Gamma_{\bar{B}^0\to f} = \frac{|A|^2}{2}|\frac{p}{q}|^2(|\rho|^2+1)e^{-\gamma t}[1 + A\cos\delta mt - S\sin\delta mt]. \quad (1.24)$$
$$(1.25)$$

This equation shows time-dependent CP violation (experimentally $|\frac{p}{q}|^2 \sim 1$,).

1.1.2 Direct CP violation

Direct CP violation means $\Gamma_{B\to f} \neq \Gamma_{\bar{B}\to \bar{f}}$. It is occurred by interference of multiple decay diagrams which have different weak-phase as shown in Figure 1.2.

In this case these amplitudes are written as

$$A_{B\to f} = A_1 + A_2 e^{i\theta_W} e^{i\delta} \quad (1.26)$$
$$A_{\bar{B}\to\bar{f}} = A_1 + A_2 e^{-i\theta_W} e^{i\delta} \quad (1.27)$$

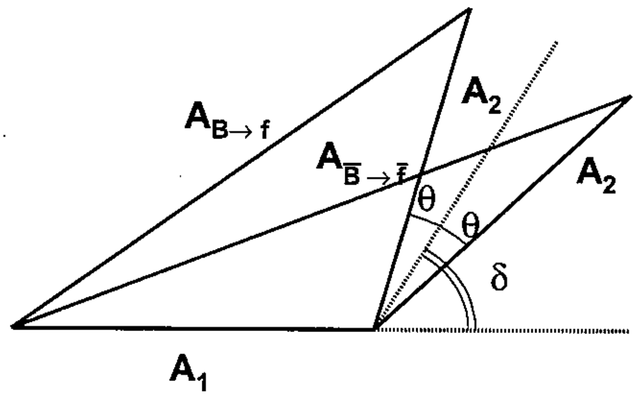

Figure 1.2: Mechanism of direct CP violation

where θ_W is the relative CP violating weak phase between two diagrams and δ is the non-CP violating strong phase.

Then the decay rates is calculated as

$$\Gamma(B \to f) = |A_1|^2 + |A_2|^2 + 2|A_1||A_2|\cos(\delta + \theta_W) \quad (1.28)$$

$$\Gamma(\bar{B} \to \bar{f}) = |A_1|^2 + |A_2|^2 + 2|A_1||A_2|\cos(\delta - \theta_W) \quad (1.29)$$

This shows direct CP violation.

In a measurement of direct CP violation if those amplitude (A_1 and A_2) are comparable, large CP violation effect is expected.

1.2 Determination of ϕ_3

The determination of ϕ_3 is still challenging, even if we use high luminisity B-factory. This is because ϕ_3 measurements needs a diagram which includes V_{ub} and it strongly suppresses a decay amplitude.

1.2.1 GWL method

For determination of ϕ_3, a method using interference between $b \to u$ and $b \to c$ decay processes is suggested, where we use $B^- \to D^0 K^-$ and $B^- \to \bar{D}^0 K^-$ that decay to common final states.

One of interesting final state of D decays is CP eigenstate such as K^+K^-, $\pi^+\pi^-$ (CP-even eigenstates called D_1) and $K_s\pi^0$, $K_s\omega$, $K_s\phi$, $K_s\eta$ (CP-odd eigenstate called D_2). Since CP phase convention is arbitrary, following the phase convention $CP(D^0) = \bar{D}^0$, CP eigenstate D mesons are represented as

$$D_{1,2} = \frac{D^0 \pm \bar{D}^0}{\sqrt{2}}$$

So amplitude of $B^- \to D_{1,2}K^-$ is given by

$$A(B^- \to D_{1,2}K^-) = \frac{1}{\sqrt{2}}[A(B^- \to D^0K^-) \pm A(B^- \to \bar{D}^0K^-)]$$

In this equation, the angle between these amplitudes is given by (without strong phase δ)

$$\theta = \arg(-\frac{V_{ub}V_{cs}^*}{V_{cb}V_{us}}) \sim \arg(-V_{ub})$$

where noted that in Wolfenstein parametarization (1.1), $V_{ub}$is the only one in the expression that has a complex phase. In same way, ϕ_3 is also written as

$$\phi_3 \equiv \arg(\frac{V_{ud}V_{ub}^*}{-V_{cd}V_{cb}^*}) \sim \arg(-V_{ub}).$$

So amplitudes of $B^\mp \to D_{1,2}K^\mp$ are written as

$$A(B^- \to D_1K^-) = \frac{1}{\sqrt{2}}[|A(B^- \to D^0K^-)| + e^{-i\phi 3}e^{+i\delta}|A(B^- \to \bar{D}^0K^-)|] \quad (1.30)$$

$$A(B^+ \to D_1K^+) = \frac{1}{\sqrt{2}}[|A(B^+ \to D^0K^+)| + e^{+i\phi 3}e^{+i\delta}|A(B^+ \to \bar{D}^0K^+)|] \quad (1.31)$$

$$A(B^- \to D_2K^-) = \frac{1}{\sqrt{2}}[|A(B^- \to D^0K^-)| - e^{-i\phi 3}e^{+i\delta}|A(B^- \to \bar{D}^0K^-)|] \quad (1.32)$$

$$A(B^+ \to D_2K^+) = \frac{1}{\sqrt{2}}[|A(B^+ \to D^0K^+)| - e^{+i\phi 3}e^{+i\delta}|A(B^+ \to \bar{D}^0K^+)|] \quad (1.33)$$

where $\delta(\equiv \delta_D - \delta_{barD})$ is strong phase difference between $B^- \to D^0K^-$ and $B^- \to \bar{D}^0K^-$ decay.

By these amplitude observable values which have sensitivity for CP violation are derived as bellow

$$A_{1,2} \equiv \frac{B(B^- \to D_{1,2}K^-) - B(B^+ \to D_{1,2}K^+)}{B(B^- \to D_{1,2}K^-) + B(B^+ \to D_{1,2}K^+)} \quad (1.34)$$

$$= \frac{2r_B \sin\delta' \sin\phi_3}{1 + r_B^2 + 2r_B\cos\delta'\cos\phi_3} \quad (1.35)$$

$$R_{1,2} \equiv \frac{R^{D_{1,2}}}{R^{D^0}} \quad (1.36)$$

$$= 1 + r_B^2 + 2r_B\cos\delta'\cos\phi_3 \quad (1.37)$$

where

$$r_B \equiv |\frac{A(B^- \to D^0 K^-)}{A(B^- \to \bar{D}^0 K^-)}| \quad (1.38)$$

$$\delta' \equiv \begin{cases} \delta & \text{for } D_1 \\ \delta + \pi & \text{for } D_2 \end{cases} \quad (1.39)$$

$$R^{D_{1,2}} \equiv \frac{B(B^\pm \to D_{1,2} K^\pm)}{B(B^\pm \to D_{1,2} \pi^\pm)} \quad (1.40)$$

$$R^{D^0} \equiv \frac{B(B^\pm \to \bar{D}^0 K^\pm)}{B(B^\pm \to \bar{D}^0 \pi^\pm)}. \quad (1.41)$$

In these formalism we have 3 unknown values, r, δ' and ϕ_3, and experimentally can get 3 independent observable values (We can measure A_1, A_2, R_1 and R_2, but one value is not independent because of the relation, $A_1 R_1 = -A_2 R_2$). So in principle we can solve this equation.

1.2.2 ADS method

A method which has more sensitivity of CP violation using other D decay mode is suggested. It is doubly-Cabbibo-supressed decay mode such as $D^0 \to K^+\pi^-$. Considering $B \to D[K^+\pi^-]K^-$ there are two diagrams as shown in Figure 1.3.

Its CP asymmetry depends on the difference of decay amplitude between $B \to D^0[K^+\pi^-]K^-$ and $B \to \bar{D}^0[K^+\pi^-]K^-$. Actually its ratio is given by

$$\frac{B(B \to D^0[K^+\pi^-]K^-)}{B(B \to \bar{D}^0[K^+\pi^-]K^-)} \approx \lambda_c |\frac{V_{cb}V_{us}^*}{V_{ub}V_{cs}^*}|^2 \frac{B(D^0 \to K^+\pi^-)}{B(\bar{D}^0 \to K^+\pi^-)} \approx 1$$

where λ_c is color-suppression-factor($\simeq 0.26$) and $\frac{B(D^0 \to K^+\pi^-)}{B(\bar{D}^0 \to K^+\pi^-)} = 0.0060$ from other experiment. As Figure 1.3 in this decay mode since two diagrams are comparable the interference effect is expected to be sizable. And these branching fractions are calculated as

$$B(B^- \to [K^+\pi^-]K^-) = (r_B^2 + r_D^2 + 2r_B r_D \cos(\delta - \phi_3))|A_B|^2|A_D|^2 \quad (1.42)$$

$$B(B^+ \to [K^-\pi^+]K^+) = (r_B^2 + r_D^2 + 2r_B r_D \cos(\delta + \phi_3))|A_B|^2|A_D|^2 \quad (1.43)$$

where

$$r_B \equiv |\frac{A(B^- \to \bar{D}^0 K^-)}{A(B^- \to D^0 K^-)}| \quad (1.44)$$

$$r_D \equiv |\frac{A(D^0 \to K^+\pi^-)}{A(D^0 \to K^-\pi^+)}| \quad (1.45)$$

$$A_B \equiv A(B^- \to D^0 K^-) \quad (1.46)$$

$$A_D \equiv A(D^0 \to K^-\pi^+) \quad (1.47)$$

$$\delta \equiv \delta_B + \delta_D \quad (1.48)$$

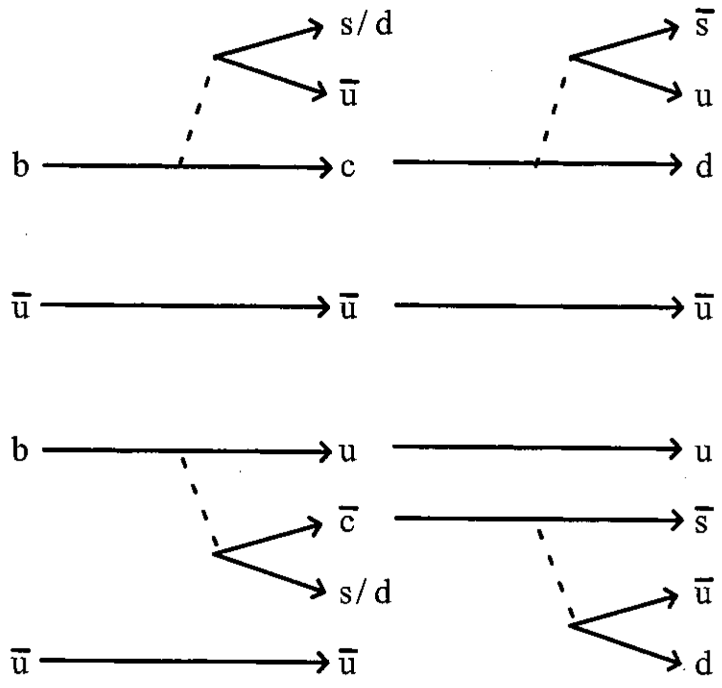

Figure 1.3: Feynman diagram of $B \to D[K^+\pi^-]K^-$ decay

$\delta_B(\delta_D)$ is the strong phase difference between the two $B(D)$ decays.

We have already know r_D, A_B, A_D from other measurements and essentially the values we want to know are ϕ_3, r_B and δ. if we combine another result of D decay mode we can get 4 equation. So we can solve this equation. Moreover if we combine more modes we can give more constraint for ϕ_3.

Chapter 2

Belle detector and KEKB accelerator

We need large $B\bar{B}$ samples to study slides and angles of CKM unitarity triangles thorough B-meson decays. Asymmetric e^+e^- collider KEKB at KEK(High energy Research Organization) can produce $B\bar{B}$ pairs with high luminocity. The Belle detector is a large-solid-angle spectrometer to accumulate the B-meson decays and have been constructed at the interaction point(IP) of KEKB.
In this chapter, details of the KEKB accelerator and the Belle detector are described.

2.1 KEKB accelerator

The KEKB is designed to specialize B-meson production with high luminocity. To determine the time-dependent CP violation we have to measure the time difference between cp-side and tag-side of B-meson decays. Since this time difference is too small to directly measure it, we measure it using Lorentz boost. So the KEKB is asymmetric e^+e^- collider. The energy of electron and positron beams are 8 GeV and 3.5 GeV, respectively. This is concern to avoid ion trapping, which happens only at low energy, of electron ring. Therefore its center-of-mass energy is 10.58 GeV, just $\Upsilon(4S)$ resonance, and the Lorentz boost parameter $\beta\gamma$ is 0.425. By this Lorentz boost B-meson can typically flight 200 μm which is measurable for experimentalists. The KEKB has two beam rings as shown in Figure 2.1. The electron ring is so-called HER(High Energy Ring) and the positron ring is so-called LER(Low Energy Ring). These rings located in TRINSTAN tunnel with circumstance of about 3 km. A only interection point is located in Tsukuba Area. And KEKB has a finite crossing angle of 11 mrad to avoid parasitic collision neat the interaction point.

In Decemmber 19th 2005, we archive $1.6270 \times 10^{34}\text{cm}^{-2}\text{s}^{-1}$ and our accumurated lunocity exceeded 0.5ab^{-1}.

	LER	HER	unit
Horizontal Emittance	18	24	nm
Beam current	1730	1261	mA
Number of bunches	1388		
Bunch current	1.25	0.909	mA
Bunch spacing	2.1		m
Bunch trains	1		
Total RF volatage Vc	8	15	MV
Synchrotron tune	−0.0249	−0.0226	
Betatron tune	45.505/43.535	44.511/41.577	
beta's at IP	59/0.65	56/0.62	cm
Estimated vertical beam size at IP	2.1	2.1	mm
beam-beam parameters	0.110/0.092	0.073/0.056	
Beam lifetime	140@1700	179@1261	min.@mA
Peak luminosity	15.62		$10^{33}/cm^2/sec$
Luminosity records	per day / 7days/ 30days 1.178/7.358/29.02		fb^{-1}

Table 2.1: The machine parameters of KEKB

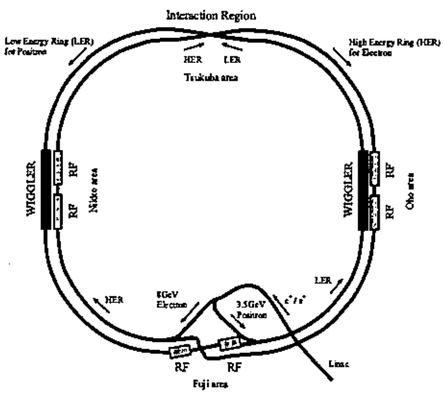

Figure 2.1: KEKB accelerator

Detector	Device	Configuration	Readout	Performance
Beam pipe	Beryllium double-wall	Cylindrical r=2.0→1.5cm		Helium gas cooling Be/He/Be
SVD1	Double Sideed Si Strip	3 layers, 300μm-thick r=3.0∼5.8cm $23° < \theta < 139°$	81.92K	$\sigma_{r-\phi} = 19 \oplus 54/p\beta \sin^{3/2}\theta \mu$m $\sigma_z = 42 \oplus 44/p\beta \sin^{5/2}\theta \mu$m
⇓ SVD2		4 layers, 300μm-thick r=2.0∼5.8cm $17° < \theta < 150°$	110.59K	$\sigma_{r-\phi} = 22 \oplus 36/p\beta \sin^{3/2}\theta \mu$m $\sigma_z = 28 \oplus 32/p\beta \sin^{5/2}\theta \mu$m
CDC	Small Cell Drift Chamber	Anode: 50 layers Cathode: 3 layers r=8∼88cm z=-79∼+160cm	A: 8.4K C: 1.5K	$\sigma_t/p_t = (0.20p_t \oplus 0.29/\beta)\%$ $\sigma_{dE/dx} = 7\%$
ACC	Silica Aerogel n=1.01∼1.03	Barrel: 960 Endcap: 228 FM-PMT readout	1,788	K/π:$1.2 < p < 3.5$GeV/c
TOF	Scintillator	ϕ:128 segmentation r=120cm Length=3m	128×2	$\sigma_t = 100$ps K/π:$p < 1.2$GeV/c
TSC		ϕ:64 segmentation	64	
ECL	CsI(Tl)	Barrel:r=125∼162cm Endcap: z=-102/+196cm	6624 1152(FWD) 960(BWD)	$\sigma_E/E = 1.3\%/\sqrt{E}$ $\sigma_{pos} = 0.5\text{cm}/\sqrt{E}$
Solenoid magnet		r=170cm		Nb-Ti-Cu alloy B=1.5T
KLM	RPC	Barrel:14 layers Endcap: 15 layers	θ:16K ϕ:16K	K_L:$\Delta\theta, \Delta\phi = 30$mrad
EFC	BGO	2×1.5×12cm^3	θ:5 ϕ:32	

Table 2.2: Sub-detectos of Belle detector

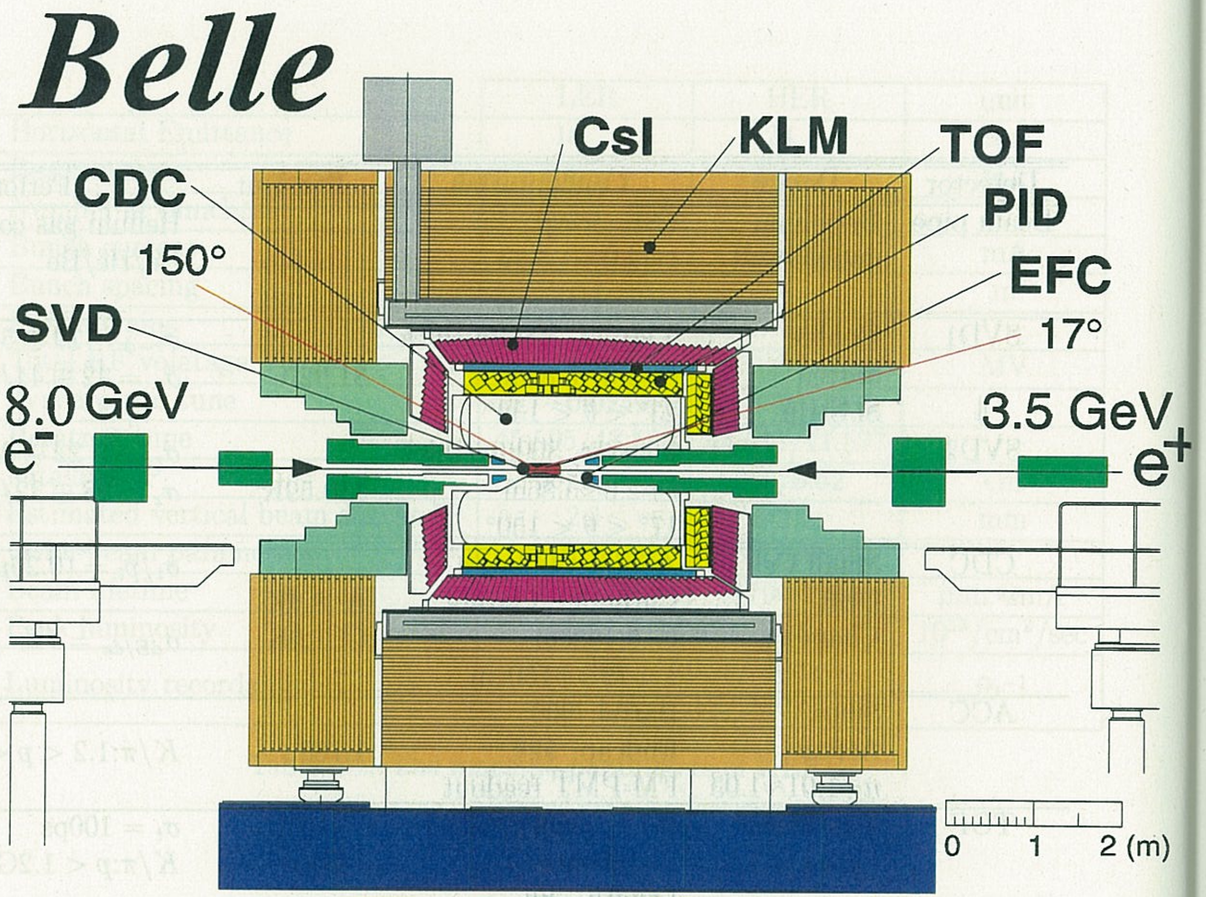

Figure 2.2: Side view of Belle detector

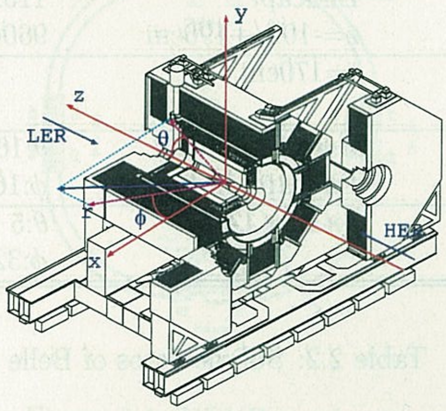

Figure 2.3: The definition of belle coordinate

2.2 Silicon Vertex Detector / SVD

SVD is located in most inner part of Belle. Its main purposes are vertexing of B-meson decay points. SVD is most important detector to measure time-dependent CP violation. We measure time-dependent CP violation through measurements of z position difference in two B-mesons decays.

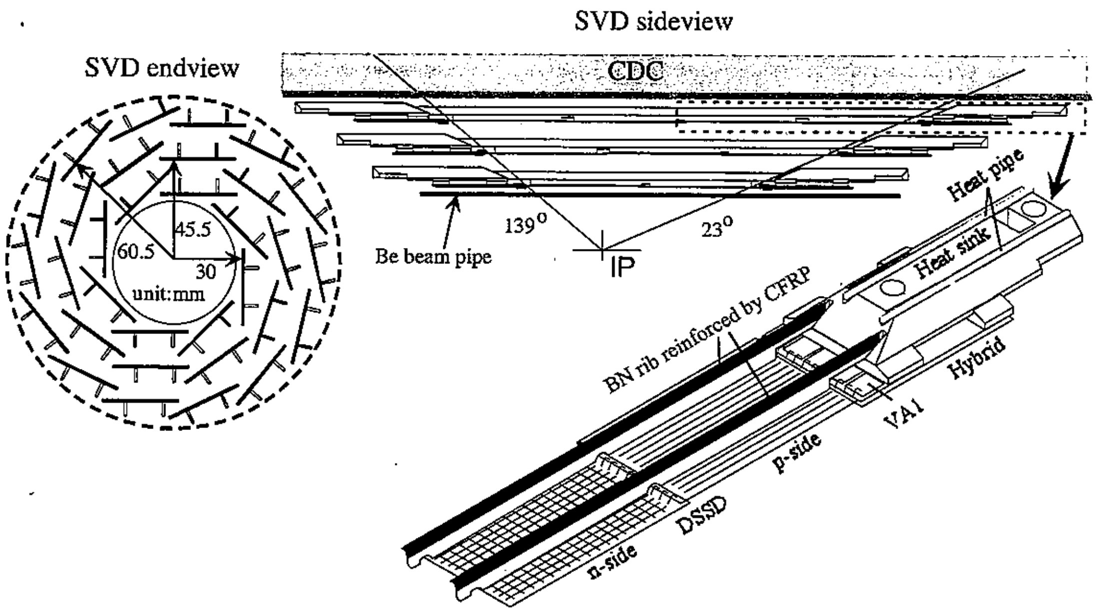

Figure 2.4: SVD1 configuration

Belle used SVD1 and is using SVD2. SVD1 is designed to have radiation tolerance up to 1 MRad. Since in summer of 2002 their radiation exceeds its limitation, SVD is replaced. In that time some up-grade is also applied for SVD. Its main future is not only increase of radiation tolerance but also close to IP in oder to improve vertex resolution.

	SVD1	SVD2
number of layers	3	4
radius of inner layer	3.0 cm	2.0 cm
acceptance	$23° < \theta < 139°$	$23° < \theta < 139°$

Table 2.3: Comparison of SVD1 and SVD2

Figure 2.5 and Figure 2.6 shows a configuration of SVD2. SVD2(SVD1) has 4(3) cylindrical detectino layers consisting units of Double-sided Silicon Strip Detectors(so-called

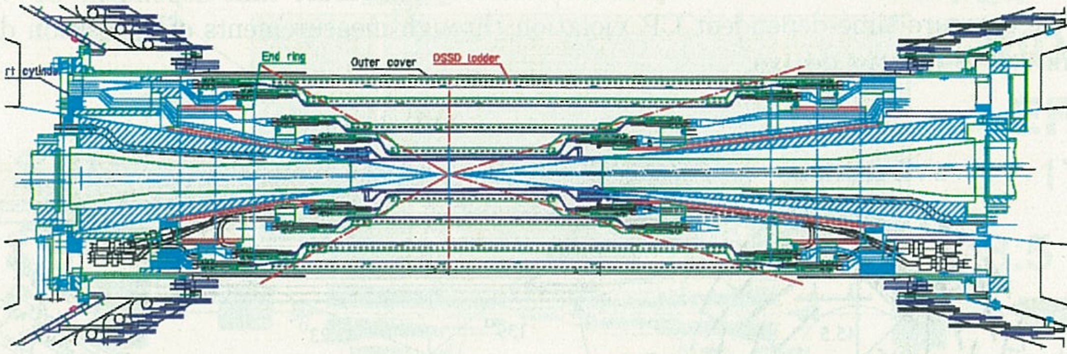

Figure 2.5: Side view of SVD2

Figure 2.6: End view of SVD2

DSSD) with 300 μm thickness. As shown in Figure 2.7 the impact parameter resolution at IP for SVD1 is

$$\sigma_{r-\phi} = (19.2 \oplus \frac{54.0}{p\beta}\sin^{3/2}\theta)\mu\text{m}$$

$$\sigma_z = (42.2 \oplus \frac{31.9}{p\beta}\sin^{5/2}\theta)\mu\text{m}$$

and in the case of SVD2 one is

$$\sigma_{r-\phi} = (21.9 \oplus \frac{35.5}{p\beta}\sin^{3/2}\theta)\mu\text{m}$$

$$\sigma_z = (27.8 \oplus \frac{31.9}{p\beta}\sin^{5/2}\theta)\mu\text{m}$$

where the first term is detector native resolution, the second term is an effect of coulomnb mulitiple scattering and $\oplus$ stands for quadratic-sum.

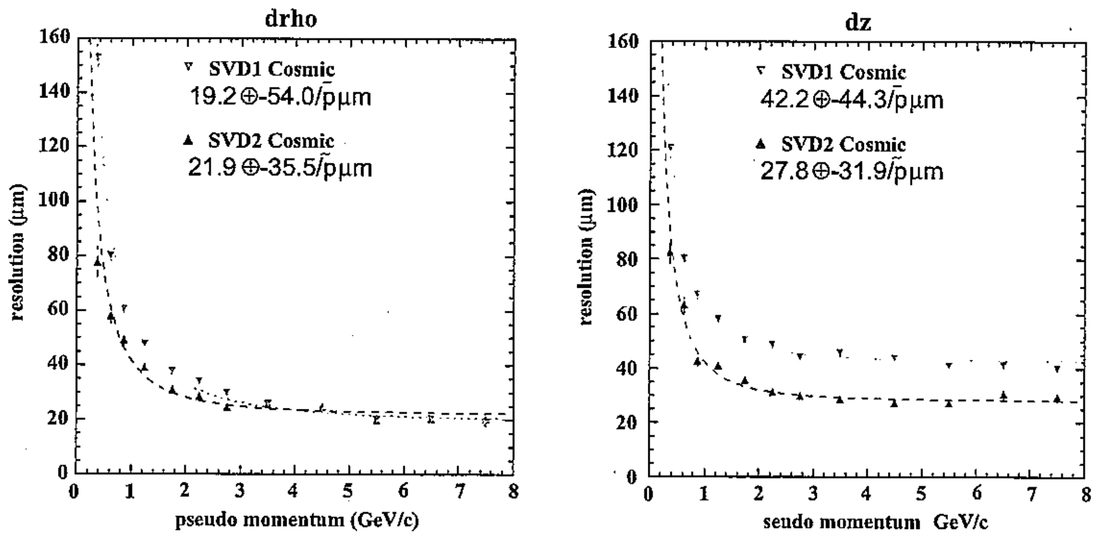

Figure 2.7: Impact parameter resolution of SVDfor $r-\phi$ and z

2.3 Central Drift Chamber / CDC

Roles of CDC are tracking, momentum measuremnts and particle identification(PID) using dE/dx measurements of charged tracks.

Figure 2.8 shows configuration of CDC. CDC covers the poler angle region $17° < \theta < 150°$ and the region from 8cm to 88cm in the directino of radial. CDC has a total of 50

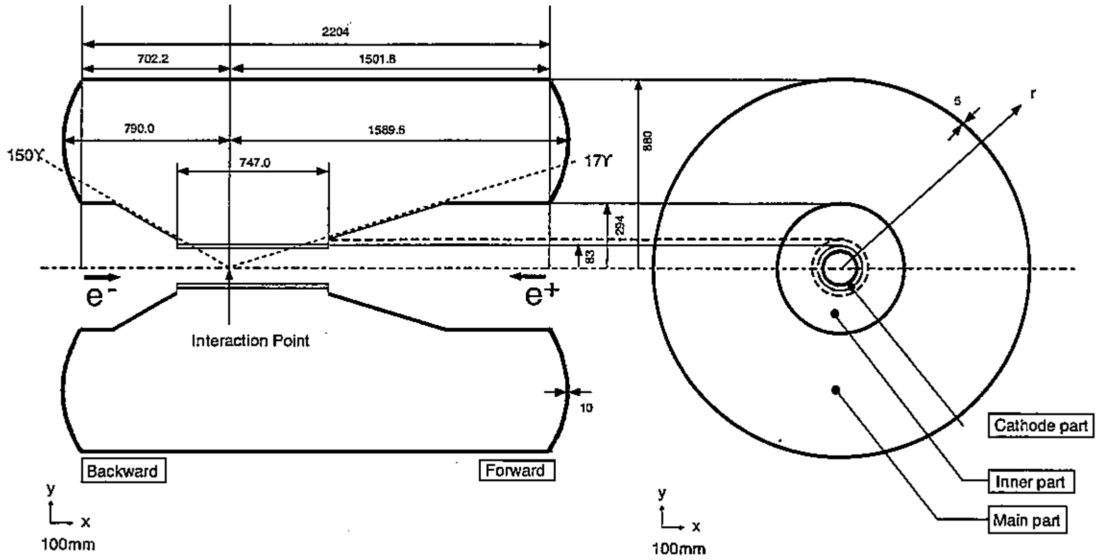

Figure 2.8: CDC configuration

sense wire layers (32 axial wire layers and 18 stereo wire layers) and 3 cathode strip layers. The stereo angles range from 42.5 mrad to 72.1 mrad. A 50% helium-50% ethane gas mizture is used in CDC. In oder to minimize Coulomb multiple scatterings, a gas which has low atomic number is selected. It contribute to good momentum determinations.

The spatial resolution is about 130 μm. The tranceverse momentum resolution is

$$\sigma_t/p_t = (0.20p_t \oplus 0.29/\beta)\%$$

In CDC the measurement of dE/dx plays a important role for particle identification. The kind of particles are distinguished by the difference of energy loss in the drift chamber which is given by Bethe-Broch formula as

$$-\frac{dE}{dx} = \frac{4\pi N_0 z^2 e^4}{mv^2}\frac{Z}{A}[\ln(\frac{2mv^2}{I(1-\beta^2)}) - \beta^2]$$

where

N_0 : Avogadro's number
Z : atomic number
A : the atoms mass number of gas
I : effective ionization potential
m : mass of passing particle

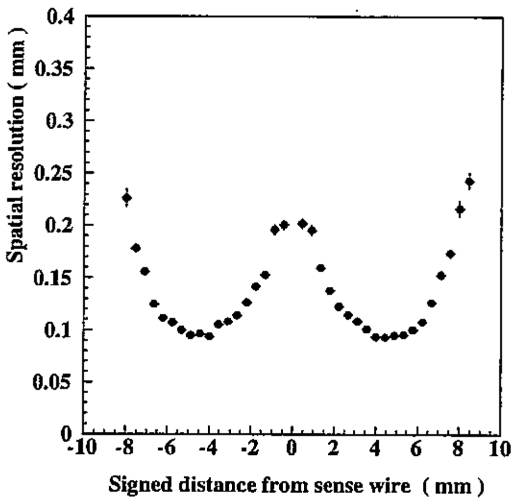

Figure 2.9: CDC spatial resolution

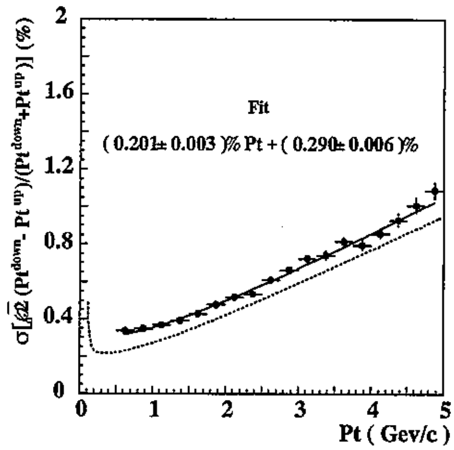

Figure 2.10: CDC momentum resolution

Actually some kind of particles are separated by dE/dx measurements as shown in Figure 2.11. Of cource, CDC also has enough dE/dx resolution to identify the kind of particle effectively as shown in Figure 2.12.

2.4 Aerogel Čherenkov Counter / ACC

ACC is a threshold Čherenkov Counter. ACC is also the sub-dtector for particle identification and compensate lack of PID ability of CDC(dE/dx measurement) and TOF(Time-of-flight) as shown in Figure 2.13.

Figure 2.14 shows configuration of ACC and Figure 2.15 shows a module of ACC. ACC has 960 modules for barrel region and 228 modules for forward endcap region. Due to KEKB asymmetric beams, final state particles which have high momentum are emitted with large poler angle and one which have low momentum are emitted with small poler angle. So ACC take into account of this condition and is optimized by varying refraction indices depending on the position of each ACC module.

In general when a particle passes a medium by the velocity which is faster than light speed in the medium a cone of Čherenkov radiation is emitted. The half angle, θ_c, of it is given by

$$\cos\theta_c = \frac{1}{n\beta} = \frac{1}{n}\sqrt{1+(\frac{m}{p})^2}$$

where $\beta = v/c$(v is velocity of a particle), n is refraction index, m is mass of a particle and p is momentum of a particle. In ACC fine-mesh photo multi multiplier(FM-PMT)

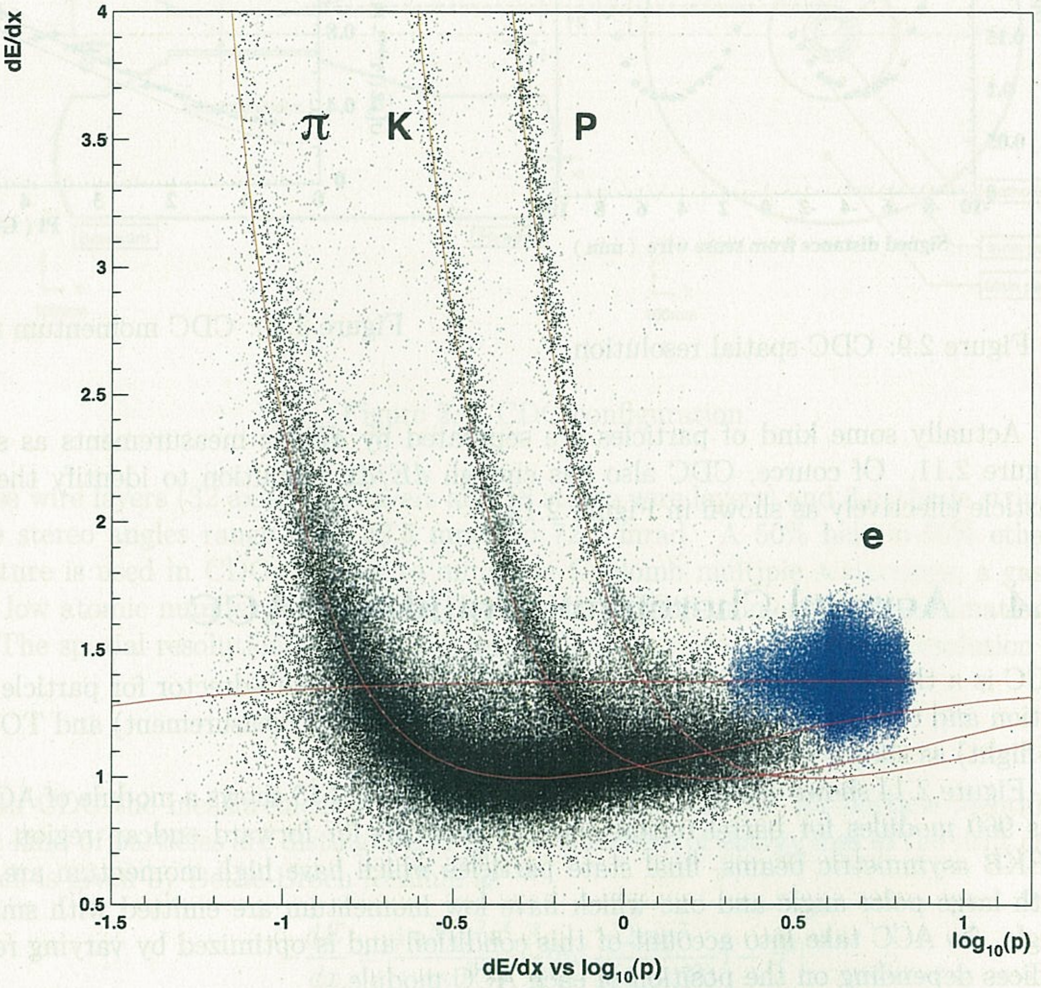

Figure 2.11: CDC dE/dx measurement

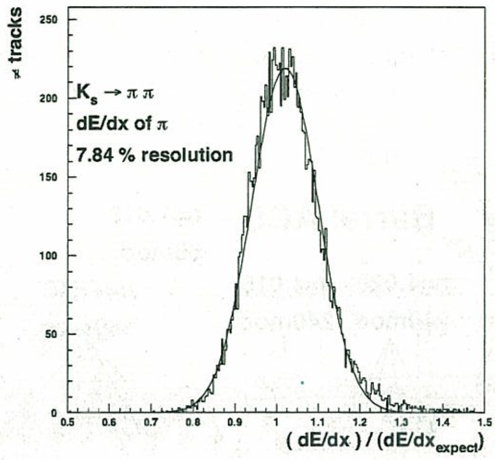

Figure 2.12: CDC dE/dx resolution

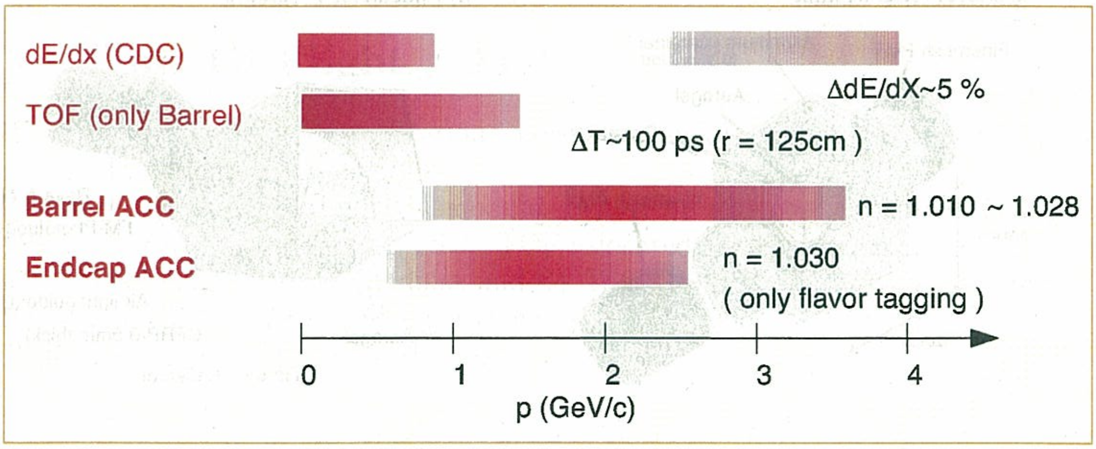

Figure 2.13: PID coverage momentum region of each sub-detector

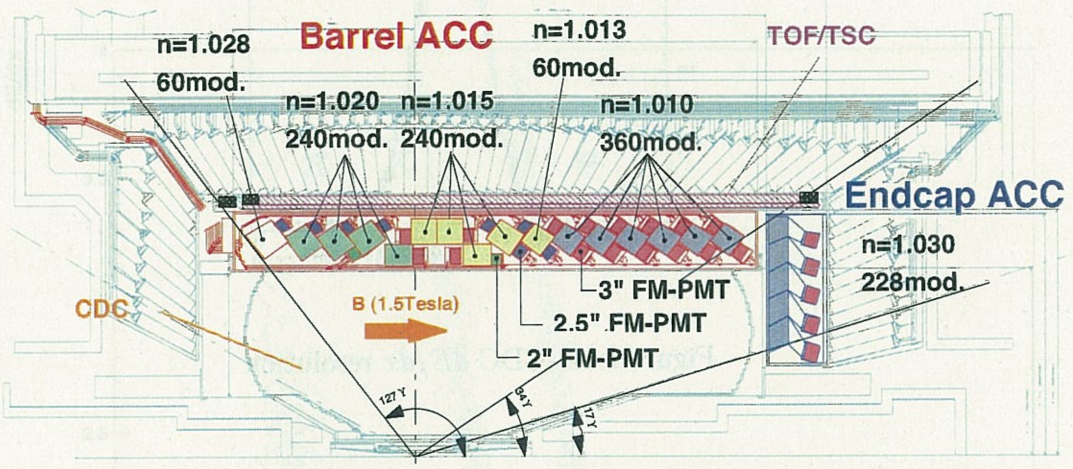

Figure 2.14: ACC configuration

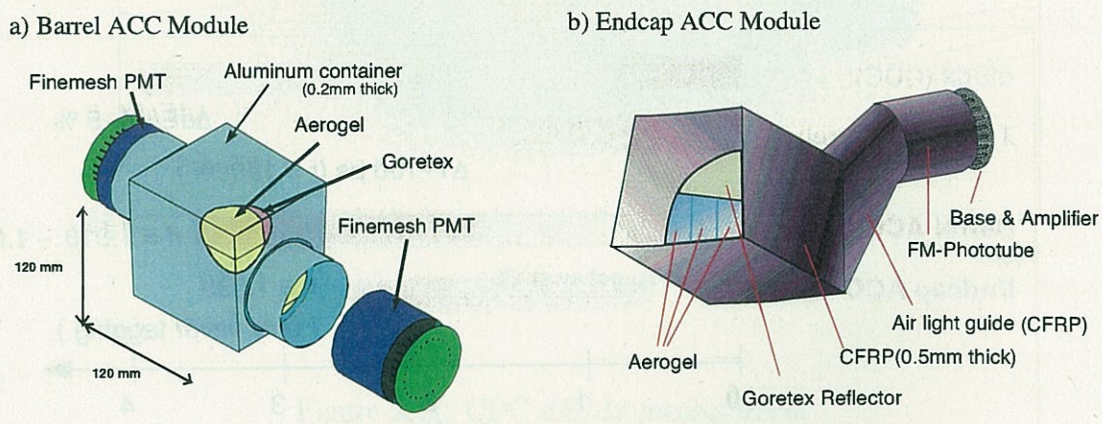

Figure 2.15: ACC module

is employed for the operation in magentic field, since usual photo multiplier doesn't work in magnetic field. It's schematic view is shown in Figure 2.16. And its performance is certainly confirmed in magnetic filed as shown in Figure 2.17.

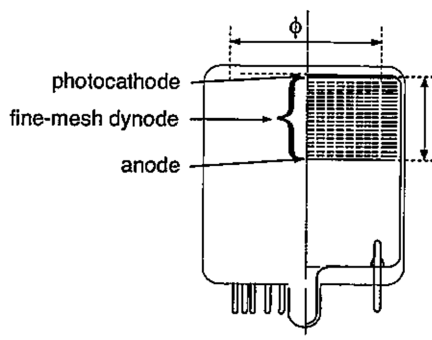

Figure 2.16: FM-PMT schematic view

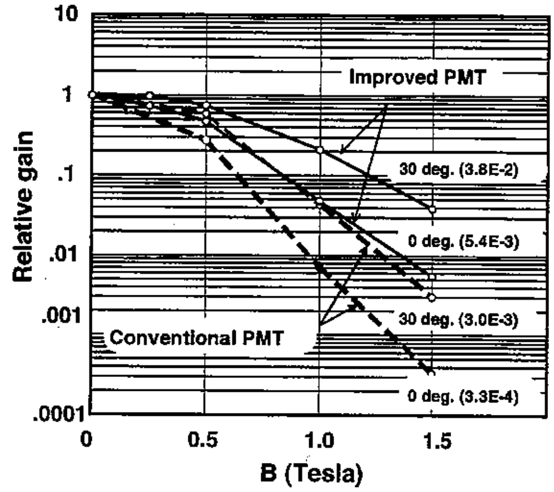

Figure 2.17: FM-PMT performance with magnetic field

Actually for particle separation ACC uses light yield of FM-PMT as shown in Figure 2.18. And for K/π separation ACC works well in over 1 GeV/c momentum region as shown in Figure 2.19 and provide low fake rate as shown in Figure 2.20.

2.5 Time Of Flight / TOF

TOF provides us with K/π separation information in the low momentum region below about 1.2 GeV/c.

Figure 2.21 shows TOF and TSC module. Belle TOF subdetector consists TOF module and Trigger Scintillation Counter(TSC). TOF is located at the position of 120 cm in radius from IP. TOF has 128 TOF modules and 64 TSC modules which are segmented in the direction of ϕ. TSC is used for trigger timing signal of Belle.

TOF determine mass of a particle as

$$m^2 = (\frac{1}{\beta^2} - 1)p^2 = ((\frac{cT_{TOF}}{L_{path}})^2 - 1)p^2$$

where T_{TOF} is a measurements of TOF and L_{path} and p^2 are determined by CDC. Figure 2.22 and Figure 2.23 shows particle identification performance of TOF.

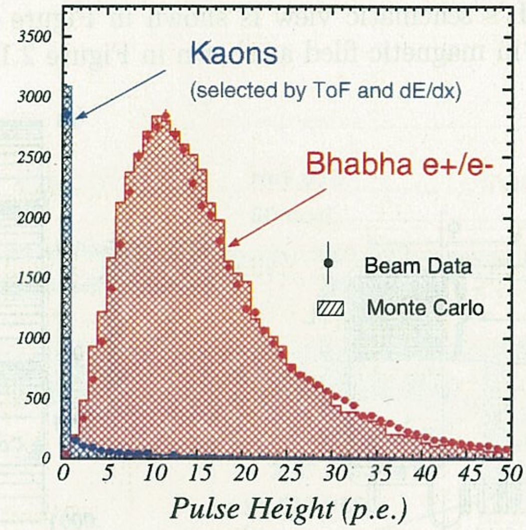

Figure 2.18: Light yield difference between K and e

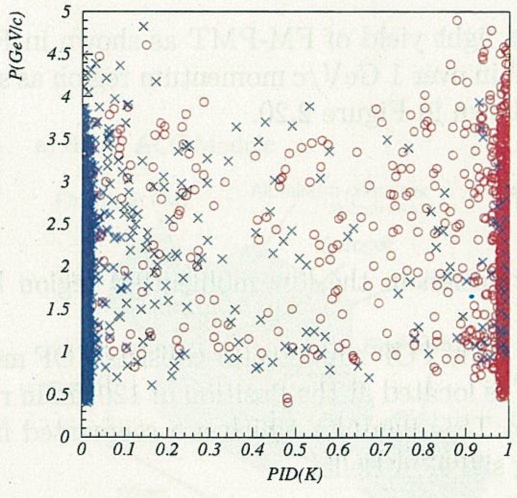

Figure 2.19: ACC PID performance for K/π separation. Red points show K tracks and blue point show π tracks

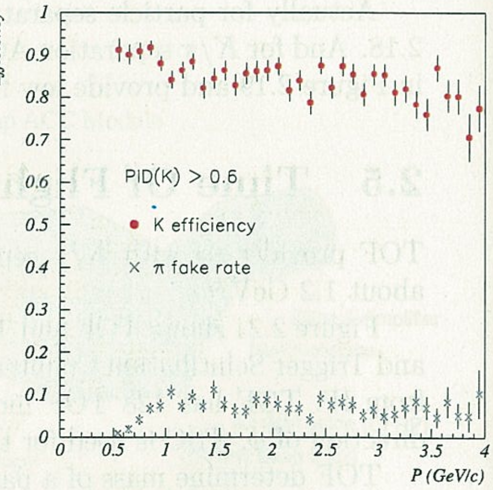

Figure 2.20: K efficiency and π fake rate of ACC

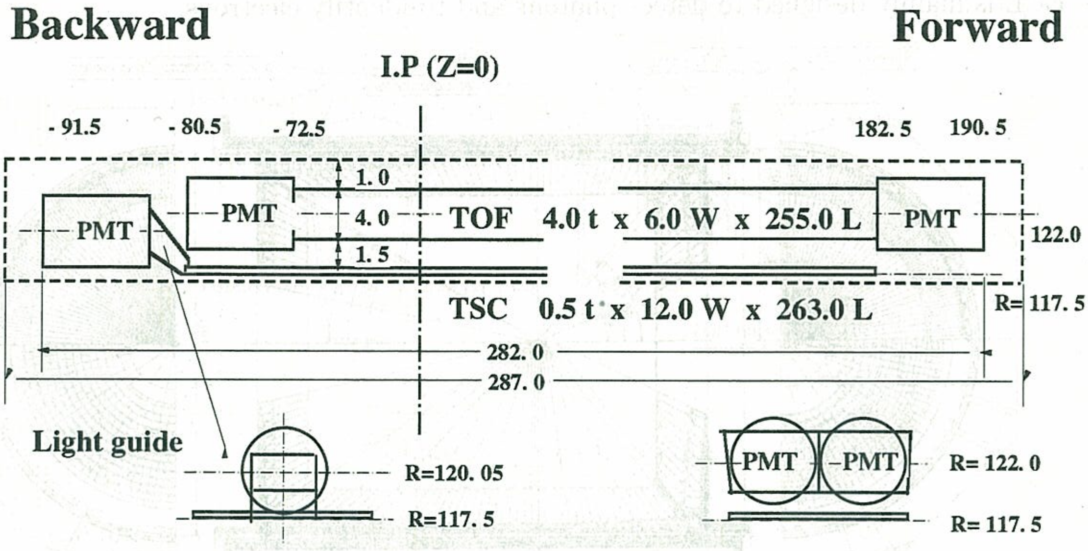

Figure 2.21: TOF and TSC

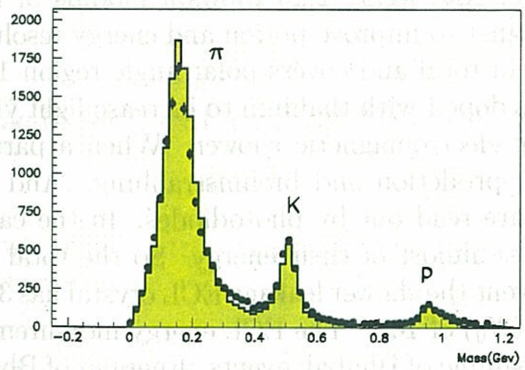

Figure 2.22: TOF PID performance

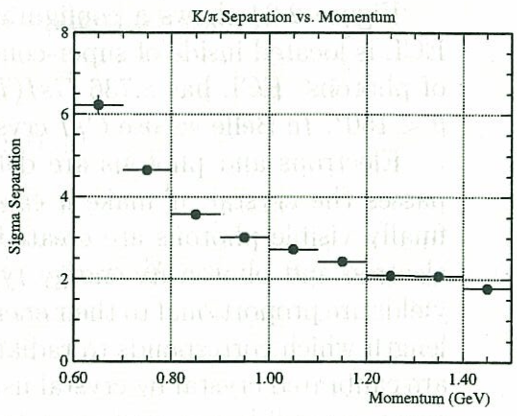

Figure 2.23: K/π separation of TOF PID

2.6 Electromagnetic Calorimeter / ECL

ECL is mainly designed to detect photons and to identify electrons.

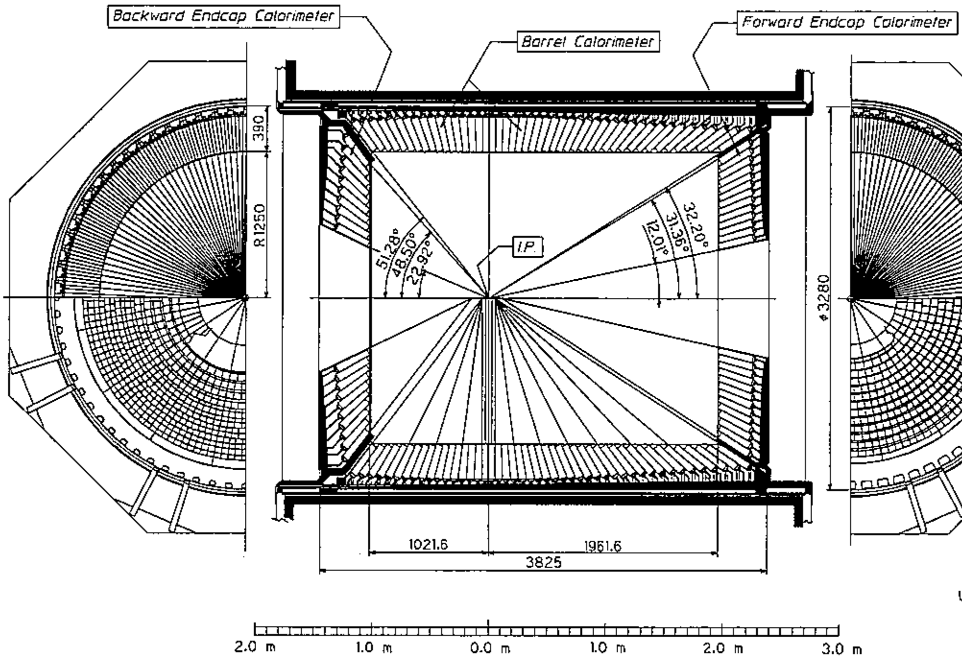

Figure 2.24: ECL configuration

Figure 2.24 shows a configuration of ECL. And figure 2.25 shows a module of ECL. ECL is located inside of super-conducting magnet to improve potion and energy resolution of photons. ECL has 8,736 $CsI(Tl)$ crystals in total and covers polar angle region $17° < \theta < 150°$. In Belle we use CsI crystal which is doped with thallium to increase light yields.

Electrons and photons are detected using electromagnetic shower. When a particles passes the crystal, it make a cascade of pair-prodction and brehmstrahlung. And then finally visible photons are created and they are read out by photodiodes. In the case of electron and photon its energy typically losses almost of their energy. So the total light yields are proportional to their energy. To prevent the shower leakage ECL crystal has 30 cm length which corresponds to radiation length (X_0) of 16.1. The ECL energy measurements are calibrated crystal by crystal using a large sample of Bhabah events. Energies of Bhabah event are well known and given by a function of scatter angle. Actually its resolution is

$$\sigma_E/E = (0.066/E \oplus 0.81/E^{1/4} \oplus 1.34)\%$$

and position resolution is

$$\sigma_x = (3.4/E \oplus 1.8/E^{1/4} \oplus 0.27)\mathrm{mm}$$

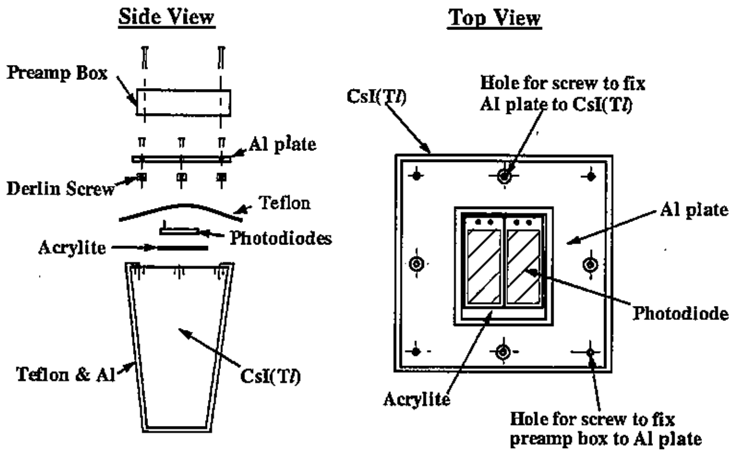

Figure 2.25: ECL module

where the unit of energy, E, is GeV.

2.7 Solenoid Magnet

To measure momentums of particle using curvature of particle's trajectory Super-conducting Magnet provides Belle with 1.5 T magnetic field in the direction of z-axis, beam.

Belle Super-conducting Magnet is made of supre-conducting niobium-titanium-copper. And its cooling is provided by liquid helium circulating.

Using a curvature we determine a momentum of charged particle as

$$p_T = qBr$$

and if we use SI units it's able to change to useful formula as

$$p_T = 0.3qBr$$

where p_T is transverse momentum, q is charges of particle, B is magnetic field and r is curvature.

2.8 K_L/μ Detector / KLM

KLM is designed to identify μ and detect K_L. In addition to these purpose KLM also works as a return-yoke of Solenoid Magnet.

Figure 2.28 shows a configuration of KLM. And Figure 2.29 shows a construction of super-layer RPC(Resistive Plate Chamber). KLM has 14 or 15 layers for Barrel and Endcap

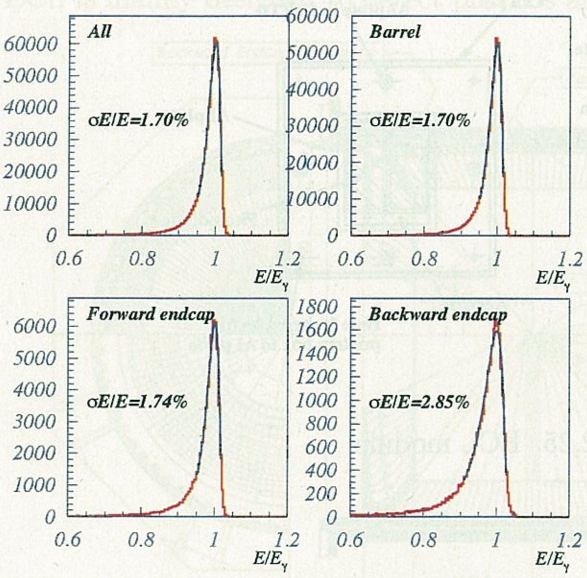

Figure 2.26: ECL energy resolution

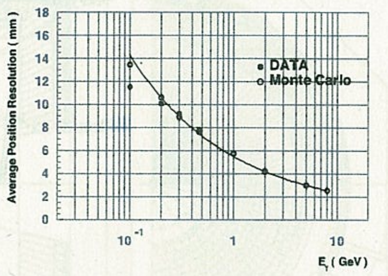

Figure 2.27: ECL spatial resolution

Figure 2.28: KLM configuration

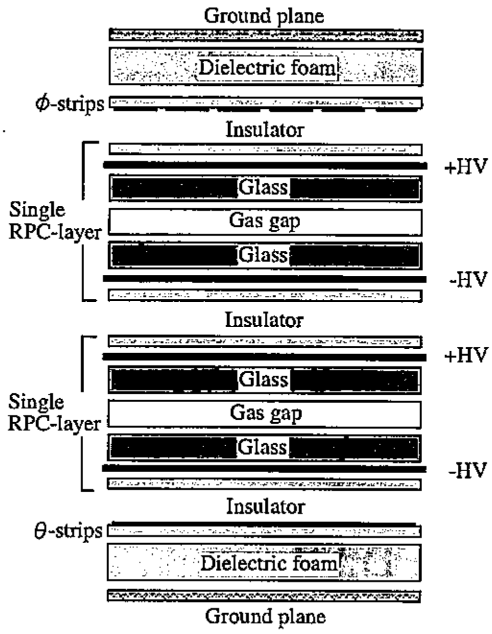

Figure 2.29: Structure of super-layer

part, respectively. In each region different shape RPC layers are used as shown in Figure 2.30 and Figure 2.31. Each layer consists super-layer RPC and 4.7 cm iron plate. KLM covers polar angle region of $20° < \theta < 150°$.

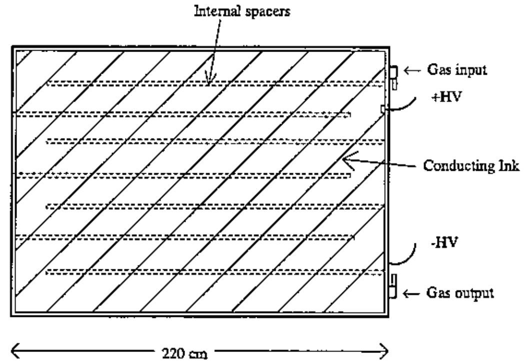

Figure 2.30: Barrel RPC

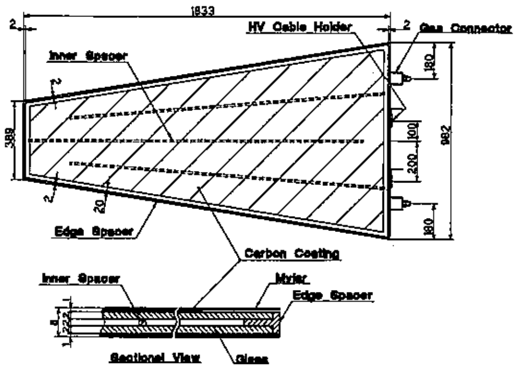

Figure 2.31: Endcap RPC

Because a difference of mass between μ (106MeV) and π (140MeV) is too close to distinguish by other sub-detectos we need a special μ detector. But μ identification is important. Because the golden-mode of $\sin 2\phi_1$ measurements is $B^0 \to J/\psi K_s$.

In KLM we mainly distinguish μ from π using number of penetrated KLM laeyers. And because K_L is neutral hadrons detections of it is difficult. But K_L sometimes plays important role in B physics (e.g. $B^0- > J/\psi K_L$. This mode is used for extraction of $\sin 2\phi_1$). So we detect K_L using hadron shower.

2.9 trigger and DAQ

The Belle trigger system has 3 layers, hardware trigger(Level 1), on-line software trigger(Level 3) and off-line software trigger(Level 4).

The central trigger system of hardware trigger is called as Global Decision Logic(GDL). GDL combines trigger signals from sub-detectors as Figure 2.32. In this stage events are selected mainly based on track and energy deposit information. GDL roughly categorizes events and makes a decision to take data within 2.2 μsec from a beam crossing. GDL has some flexibility to keep the trigger rate within tolerance of the DAQ system. For example basically we don't have spacial reason to take Bhabha events for physic analysis. But we need a few events for a luminosity measurement and ECL calibration. So we set the trigger condition to take these events sometimes, not always. But its rate is suppressed not to disturb data taking of physical interesting events. if GDL decide to take a event it provide sub-detectors with common stop signals of TDCs and gate signals of ADC. Then readout data is transferred to the event builder.

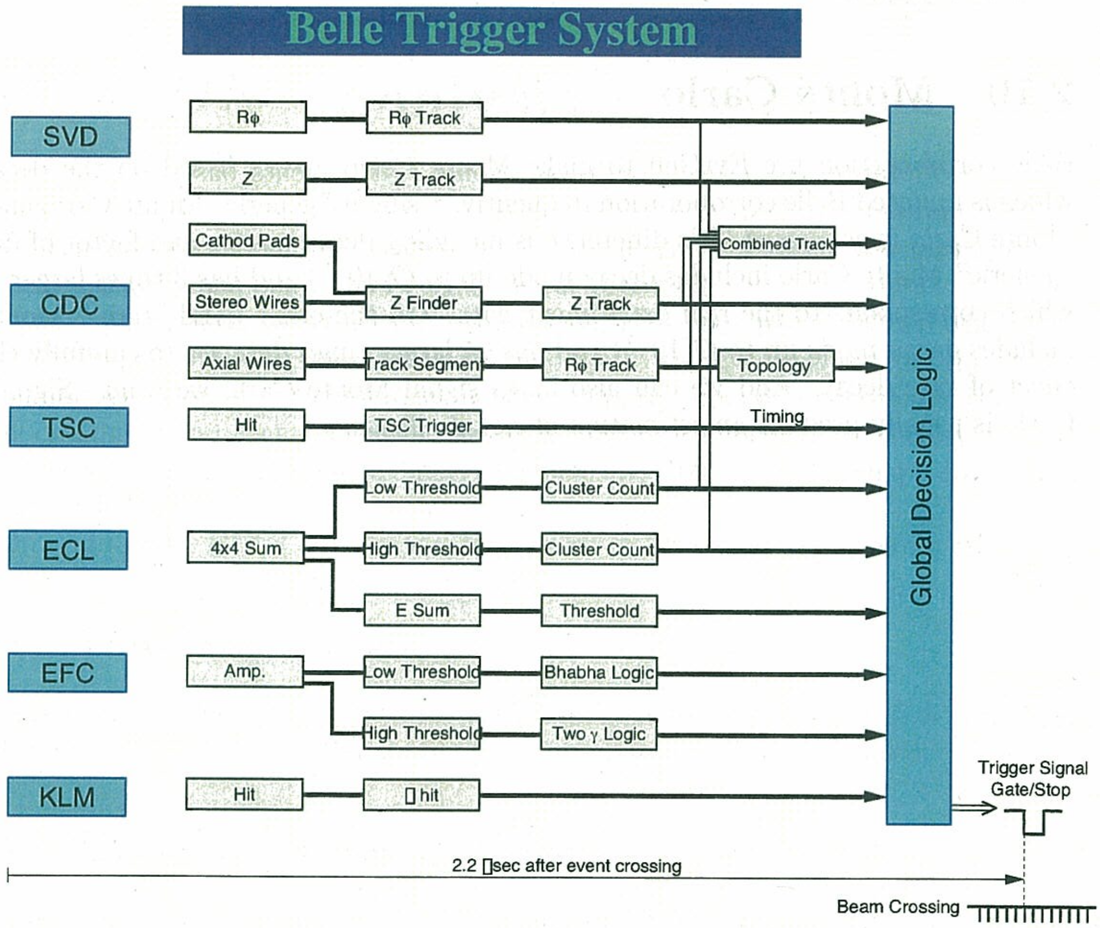

Figure 2.32: Trigger scheme

Shipped data from the event builder is selected by on-line software trigger. On-line software trigger consists ultra fast tracking finder which select about 60% events based on the z vertex position. Then the selected events are sent to Offline Computing Farm.

The recored events are processed using more precise filter, off-line software trigger. The events passing off-line software trigger are send to the Data Storage Tape(DST) production chain. I n this stage tables of tracking, gamma energy, PID information and etc, are made for physic analysis.

2.10 Monte Carlo

Belle corroboration use EvtGen to make Monte Carlo events based on the decay table which is updated Belle corroboration frequently. Using it "generic" Monte Carlo and "rare" Monte Carlo is generated. It's difference is including decay modes and factor of data size. "generic" Monte Carlo includes decay mode up to $\mathcal{O}(10^{-5})$ and has 3 times larger data set which corresponds to the real experiment data. On the other hand "rare " Monte Carlo includes decay mode up to $\mathcal{O}(10^{-7})$ and has 25 larger times data set to carefully check the effect of rare decay. And we can also make signal Monte Carlo we want. Signal Monte Carlo is usually used for an estimation of signal efficiency.

Chapter 3

$B^- \to DK^-$ analysis

In this chapter the procedure of $B^- \to DK^-$ reconstruction which consists event selection criteria, backgrounds, and signal extraction, is described.

Although our interest is the suppressed decay, $B^- \to D_{sup}[K^+\pi^-]K^-$, the favored decay, $B^- \to D_{fav}[K^-\pi^+]K^-$ whose statistics is enough to suppress systematics uncertainties, is also analyzed. Because the difference between suppressed and favored mode is only charge of D daughters and their kinematics are same, by taking the ratio of these yields, most of systematic uncertainties such as detection efficiency, PID cut, event shape LR cut and etc. are cancelled.

In addition to $B^- \to DK^-$ mode $B^- \to D\pi^-$ is also analyzed for cross check.

3.1 Data set

In this analysis, 366 fb^{-1} of data set (experiment number 7 $\sim$ 41) which corresponds to 386 million $B\bar{B}$ pairs recorded at the $\Upsilon(4S)$ resonance with Belle is used.

3.2 Event selection criteria

Firstly a list of event selection criteria is shown. Then the detail description of that is shown below the list. The same style is used for each selection criteria in this thesis.

3.2.1 Primary charged tracks

- $|dr| < 5$ mm, $|dz| < 5$ cm

To suppress beam backgrounds, charged tracks are required to have a point of closest approach to the beam line within $\pm$ 5 mm of IP in the direction perpendicular to beam axis, dr, and $\pm$ 5 cm in the direction parallel to the beam axis, dz.

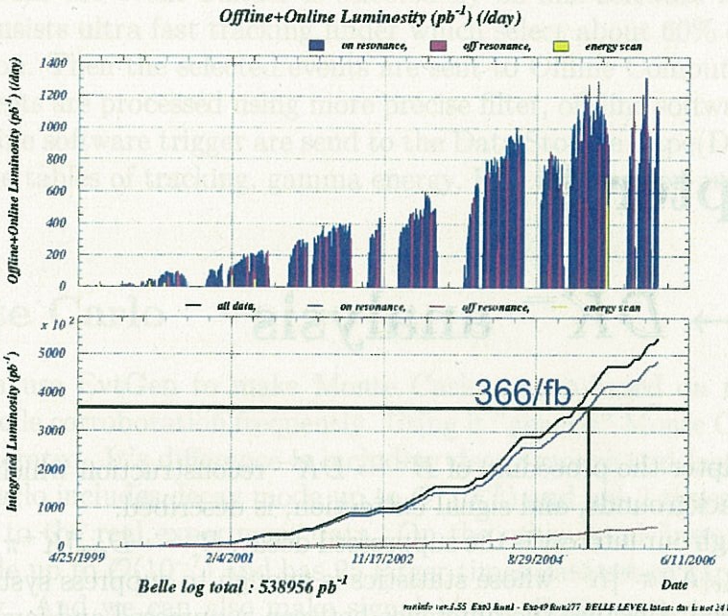

Figure 3.1: Belle luminosity

3.2.2 D reconstruction

- K tracks : $LR(K/\pi) > 0.4$
- π tracks : $LR(K/\pi) < 0.7$
- $1.850 < M(K\pi) < 1.879[\mathrm{GeV}/c^2](2.5\sigma)$

D mesons are reconstructed by combining two oppositely charged tracks.

To distinguish K tracks from π tracks, we use likelihood ratio between K and π which is constructed using Kaon(pion) likelihoods, $\mathcal{L}_K(\mathcal{L}_\pi)$, based on dE/dX measurements, Čerenkov counter(ACC) information and Time-of-Flight(TOF) and calculated as

$$LR(K/\pi) = \mathcal{L}_K/\mathcal{L}_\pi \quad (3.1)$$

$$\mathcal{L}_{K,\pi} = \mathcal{L}_{K,\pi}^{dE/dx} \times \mathcal{L}_{K,\pi}^{ACC} \times \mathcal{L}_{K,\pi}^{TOF} \quad (3.2)$$

In this case we require $LR(K/\pi) = \mathcal{L}_K/\mathcal{L}_\pi > 0.4$ for K and $LR(K/\pi) < 0.7$ for π. And in this momentum region K and π efficiencies are 0.987 and 0.986, and their fake rate(the probability that $\pi(K)$ tracks are identified as $K(\pi)$) are 0.051 and 0.079, respectively.

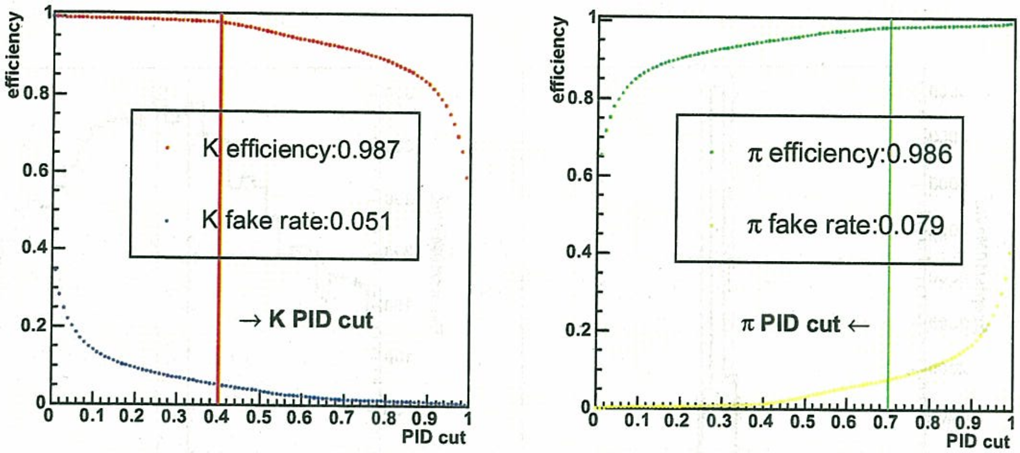

Figure 3.2: PID performance of D daughters, K(left) and π(right). This shows the efficiency and fake rate as a function of PID cut value. This data set is taken from Monte Carlo.

D candidates are required to have an invariant mass within $\pm 2.5\sigma$ of the nominal D mass, $1.850 < M(K\pi) < 1.879[\mathrm{Gev}/c^2]$. And to suppress contaminations from favored decay if K and π mass assignments are exchanged and its mass is within D mass signal region, the event is vetoed.

To improve the momentum determination of B mesons, tracks of D candidates are refitted by constraining the invariant mass to the nominal D mass and the track origin to the reconstructed vertex position (mass-vertex fit).

3.2.3 B^- reconstruction

- prompt K tracks : $LR(K/\pi) > 0.6$
- prompt π tracks : $LR(K/\pi) < 0.2$
- $5.27 < M_{bc} < 5.29[\mathrm{GeV}/c^2]$
- $|\Delta E| < 0.05[\mathrm{GeV}]$

B^- candidates are reconstructed by combining the D candidate which satisfies the condition and a prompt particle candidate. For prompt particles, PID LR cut is tighter than daughter tracks of D^0 candidates to suppress the contamination from $B \to D\pi^-$ mode for $B \to DK^-$ mode.

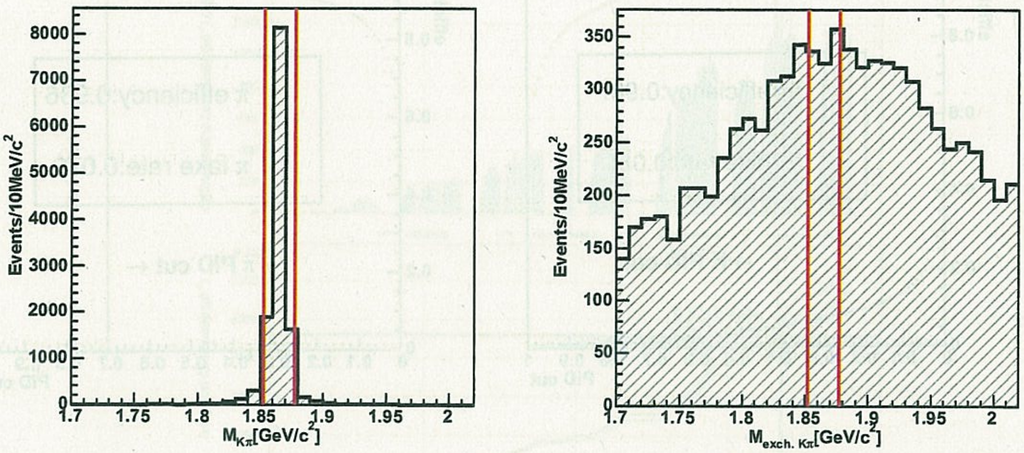

Figure 3.3: The mass distribution of $K\pi$ pair(left) and the exchanged mass distribution(right).This data set is taken from Monte Carlo.

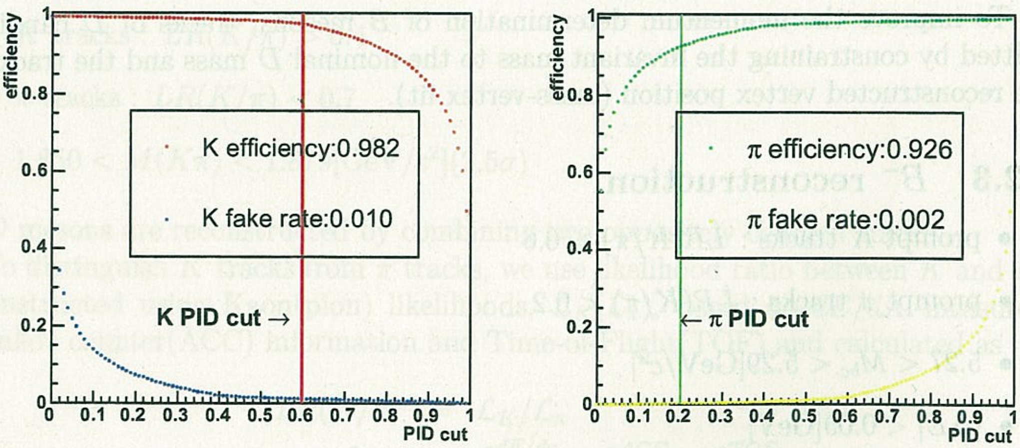

Figure 3.4: PID performance of prompt particles, K(left) and π(right).This data set is taken from Monte Carlo

In addition to these cuts, to identify the signal I use two kinematic variables, the energy difference

$$\Delta E \equiv E_D + E_{K(\pi)} - E_{beam}$$

and the beam-energy-constrained mass

$$M_{bc} \equiv \sqrt{E_{beam}^2 - (\vec{p}_D + \vec{p}_{K(\pi)})^2},$$

where E_D is the energy of the D candidates, $E_{K(\pi)}$ is the energy of the $K(\pi)$ and E_{beam} is the beam energy, all evaluated in the center of mass (CM) frame. $\vec{p}_D$ and $\vec{p}_{K(\pi)}$ are the momenta of the D and $K(\pi)$ in the cm frame. Figure 3.5 and Figure 3.6 show typical distributions of ΔE and M_{bc}.

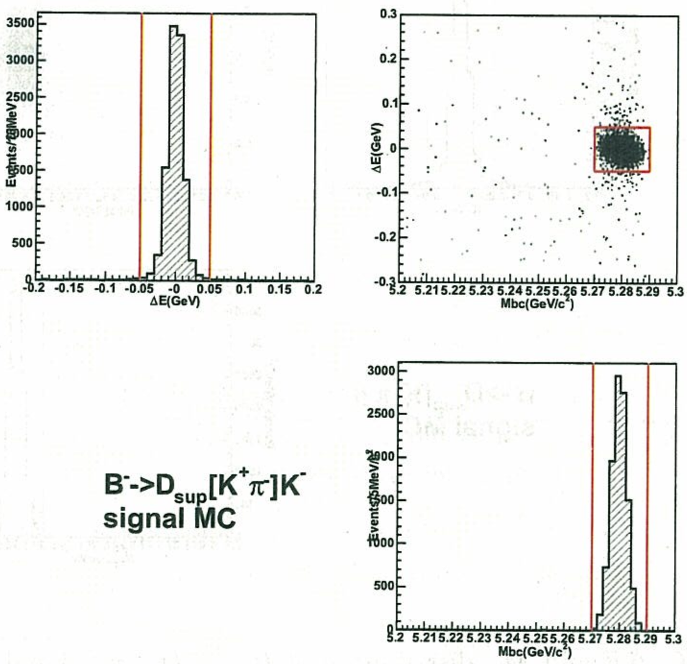

Figure 3.5: ΔE and M_{bc} distribution of $B^- \to D_{sup} K^-$ signal Mote carlo events

If there are multiple-candidates in a event, we choose the best candidate on the basis on χ^2 determined from

$$\chi^2 = (\frac{m_{k\pi} - m_{D^0 nominal}}{\sigma_D})^2 + (\frac{M_{bc} - 5.285}{\sigma_{M_{bc}}})^2$$

where σ represents experimental resolution.

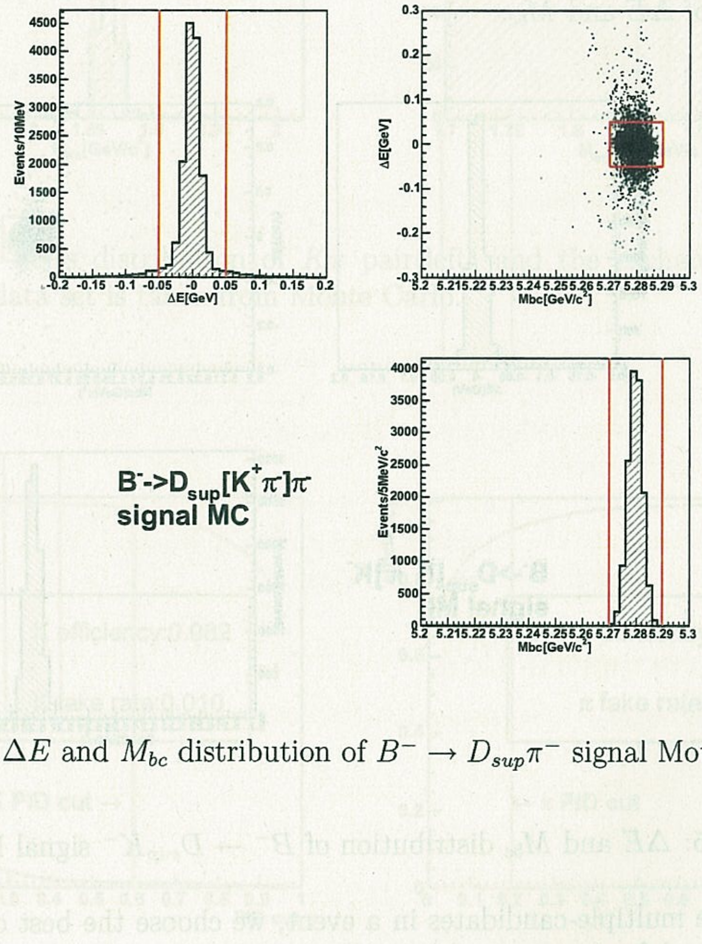

Figure 3.6: ΔE and M_{bc} distribution of $B^- \to D_{sup}\pi^-$ signal Mote carlo events

3.2.4 $q\bar{q}$ continuum backgrounds suppression

- DK mode: $LR_{(KSFW,cos\theta_B)} > 0.91$
- $D\pi$ mode: $LR_{(KSFW,cos\theta_B)} > 0.74$

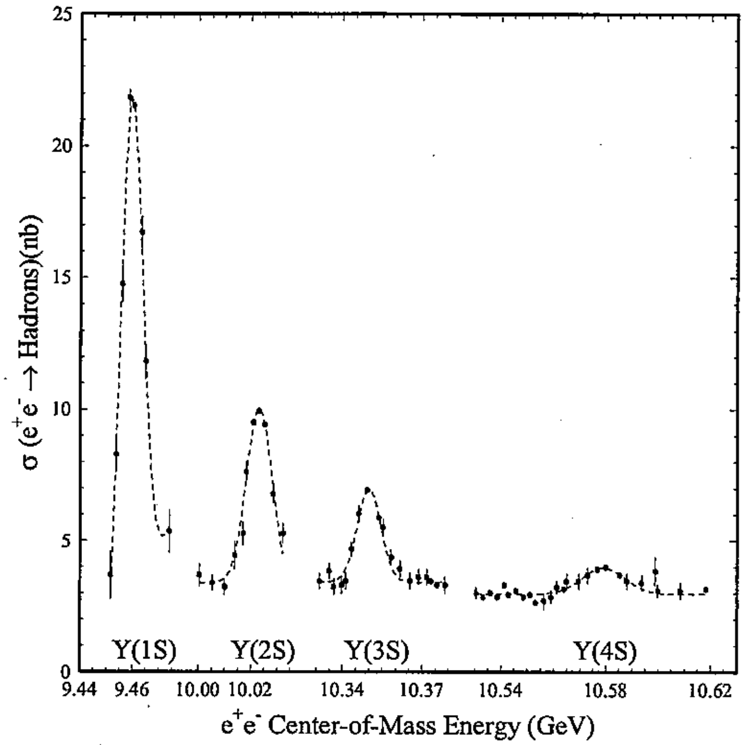

Figure 3.7: e^+e^- →hadron cross-section

As shown in Figure3.7, around $\Upsilon(4S)$ resonance there are 3 times lager $q\bar{q}$ background than $B\bar{B}$ events. Actually as shown in Figure 3.8 and Figure 3.9 large $q\bar{q}$ backgrounds are seen with "uds" and "charm" Monte Carlo. The difference between $B\bar{B}$ events and $q\bar{q}$ background is event topology. The decay shape of $q\bar{q}$ event is spherical, and one of $B\bar{B}$ is jet-like. To suppress this large backgrounds from two-jet like $e^+e^- \rightarrow q\bar{q}(q = u, d, s, c)$ continuum processes, variables that characterize the event topology are used. And for signal and background sample events, signal Monte Carlo events and M_{bc} sideband data, where qq events are dominant comparing to $B\bar{B}$ events, are used, respectively.

There are some methods to characterize it, thrust angle(Figure 3.10 left), super Fox Wolflam method(so-called SFW. Figure 3.10 right) and improved SFW technique(so-called KSFW. Figure 3.11).In detail, refer to Appendix A. So we compare these method as shown

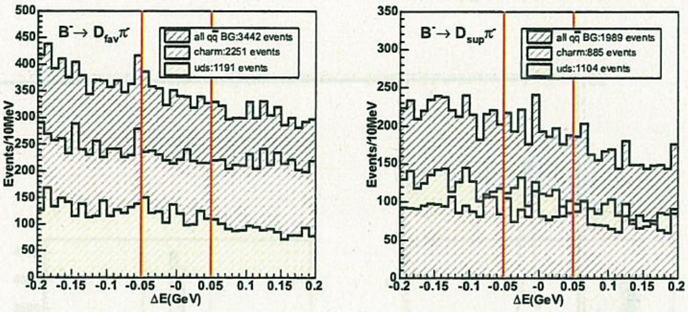

Figure 3.8: $q\bar{q}$ background for $B^- \to D\pi^-$ decay mode with "uds" and "charm" Monte Carlo. The numbers of events within ΔE signal region(inside of red lines) are shown.

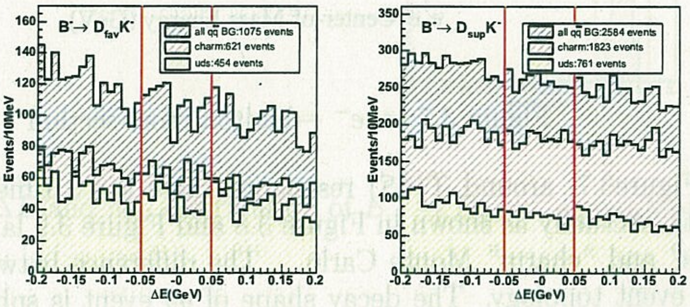

Figure 3.9: $q\bar{q}$ background for $B^- \to DK^-$ decay mode with "uds" and "charm" Monte Carlo. The numbers of events within ΔE signal region(inside of red lines) are shown.

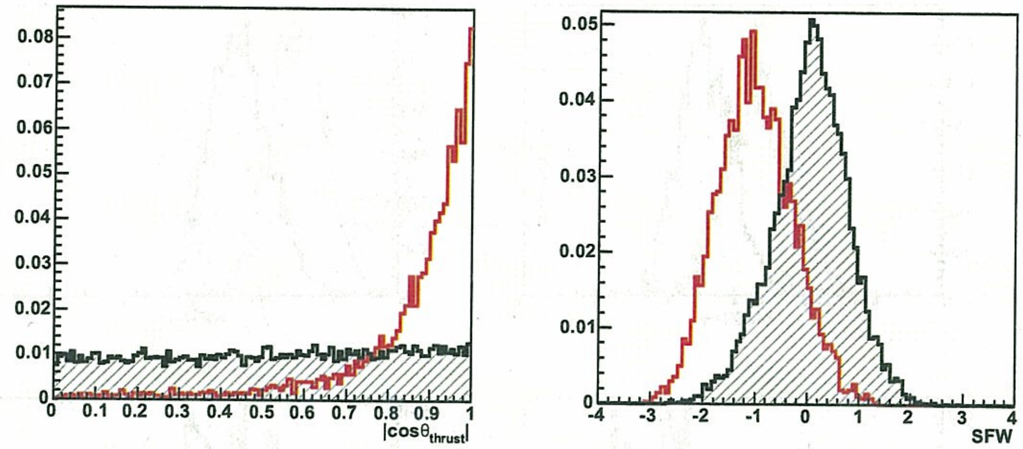

Figure 3.10: The $\cos\theta_{thrust}$ distribution(left) and SFW value distribution(right).In these plot hatched histogram is signal Monte Carlo and red histogram is M_{bc} sideband data.

in Figure3.12. By this result to suppress background and retain efficiency simultaneously KSFW method looks most preferable than other methods. So in this thesis KSFW method is used for event shape characterization.

Furthermore, $\cos\theta_B$, the angle in the CM system of the B flight direction with respect to the beam axis, is also used to distinguish $B\bar{B}$ events from continuum events. The angular distribution of $B\bar{B}$ pair is proportional to $\sin^2\theta_B$ because the spin and parity of $\Upsilon(4S)$ are $J^P = 1^-$, while one of continuum background is essentially uniform as shown in Figure3.13.

These two independent variables, KSFW and $\cos\theta_B$, are combined to form a likelihood ratio

$$LR_{(KSFW, cos\theta_B)} = \mathcal{L}_{sig}/(\mathcal{L}_{sig} + \mathcal{L}_{cont})$$

$$\mathcal{L}_{sig(cont)} = \mathcal{L}^{KSFW}_{sig(cont)} \times \mathcal{L}^{\cos\theta_B}_{sig(cont)}$$

where $\mathcal{L}_{sig}$ and $\mathcal{L}_{cont}$ are likelihoods defined from KSFW and $\cos\theta_B$ distributions for signal and continuum backgrounds, respectively.

We optimize the LR requirement by maximizing "figure of merit"(F.o.M) which is defined as

$$(F.o.M) \equiv \frac{S}{\sqrt{S+N}}$$

where S and N denote the expected number of signal and background events in the signal region.

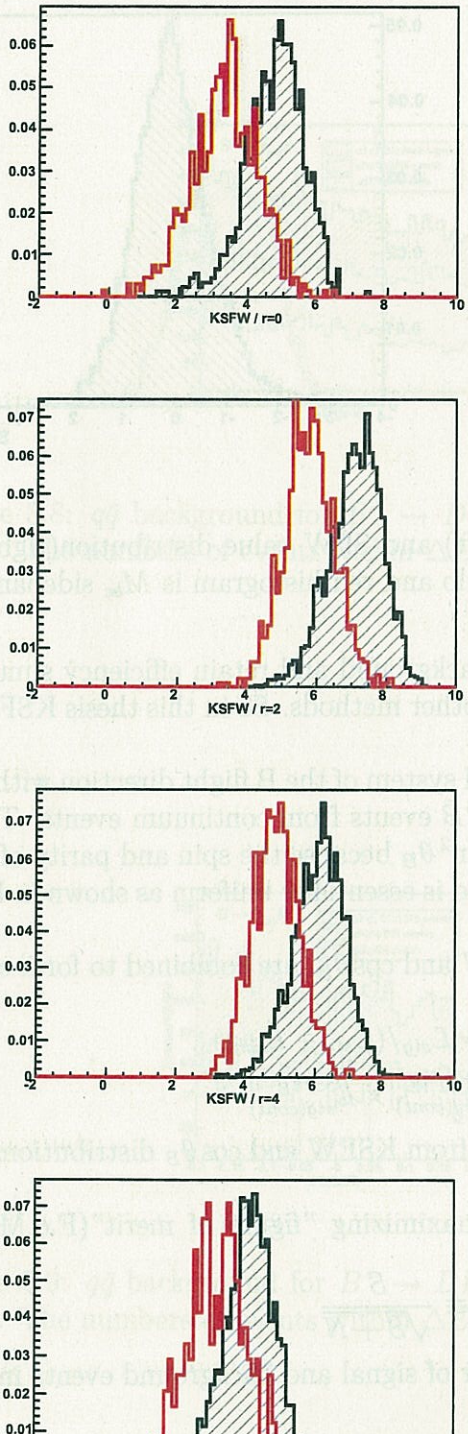

Figure 3.11: KSFW value distribution. These plot shows KSFW value distribution of each missing-mass-square bin.Hatched histogram is signal Monte Carlo and red histogram is M_{bc} sideband data.

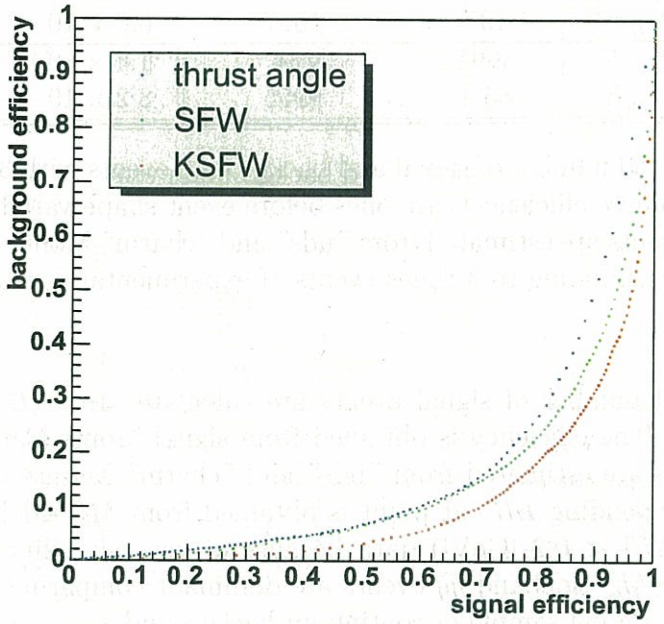

Figure 3.12: The comparison of continuum backgrounds suppression methods

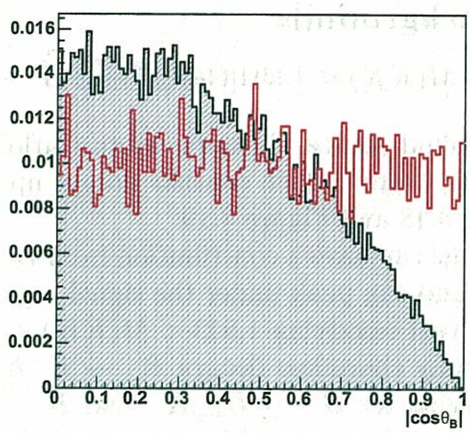

Figure 3.13: $\cos\theta_B$ distribution. θ_B is a B flight direction respect to beam axis. Hatched histogram is signal Monte Carlo and red histogram is M_{bc} sideband data.

Mode	#(signal)	#(background)	Expected $\mathcal{B}$	Efficiency(%)
$B^- \to D_{fav}\pi^-$	56154	2654	1.9×10^{-4}	38.3
$B^- \to D_{sup}\pi^-$	197	1507	6.6×10^{-7}	38.7
$B^- \to D_{fav}K^-$	3691	814	1.4×10^{-5}	34.2
$B^- \to D_{sup}K^-$	85.4	1955	3.2×10^{-7}	34.6

Table 3.1: Expected number of signal and background events with 366 fb^{-1} data set (386×10^6 $B\bar{B}$ pairs). These efficiencies are ones before event shape variable cut. These numbers of background events are estimated from "uds" and "charm" Monte Carlo events whose size are 532 fb^{-1} corresponding to 3 times events of experimental number 21 to 37(177.4fb^{-1}).

The expected number of signal events are calculated from $B^- \to D_{sup}K^-$ previous results by Belle. The efficiency is obtained from signal Monte Carlo. For background its number of events are estimated from "uds" and "charm" Momte Carlo. But background reduction rate depending LR cut point is obtained from M_{bc} sideband($5.2 < M_{bc} < 5.26$ [GeV/c^2] and $|\Delta E| < 0.2$ [GeV]) data because of low reliability for QCD dynamics in Monte Carlo. In M_{bc} sideband $q\bar{q}$ events are dominant comparing to $B\bar{B}$ events. So M_{bc} sideband data is a good sample of continuum background.

For $B^- \to D_{sup}K^-(\pi^-)$ we require $LR > 0.90(0.74)$, which retains 40.0% (65.7%) of the signal and removes 99.0% (94.3%) of the continuum background as Figure 3.14 and Figure 3.15. To cancel the systematics, same cut as the suppressed mode is applied to the favored mode.

3.2.5 Peaking backgrounds

- KK veto: $1.843 < M(KK) < 1.894$[GeV/c^2] for $B^- \to D_{sup}K^-$ decay

To check the background source, "generic Mote Carlo" which consists decays up to $\mathcal{O}(10^-5)$ and "rare Monte Calro" which consists decays up to $\mathcal{O}(10^{-7})$ are used as Figure 3.16, Figure 3.17, Figure 3.18 and Figure 3.19.

For $B^- \to D_{sup}K^-$, one can have a contribution from $B^- \to D\pi^-$, $D \to K^+K^-$, which has the same final state and can peak under the signal region of M_{bc} and ΔE. In order to reject these events, the event satisfying $1.843 < M(KK) < 1.894$[GeV/c^2] is vetoed.

Furthermore, three-body charmless decays $B^- \to K^+K^-\pi^-$ and $B^- \to K^+\pi^-\pi^-$ can peak inside the signal region for $B^- \to D_{sup}K^-$ and $B^- \to D_{sup}\pi^-$, respectively. These peaking backgrounds can not be removed by veto. So their effects are estimated from the ΔE distributions of events in a D mass sideband, corresponding to $\pm(2.5 - 10)\sigma$ away from the nominal D mass ($1.807 < M(K\pi) < 1.850$[GeV/c^2] and $1.879 < M(K\pi) < 1.937$[GeV/c^2]). We fit these distributions, which are shown in Figure3.20 and Figure3.21, using a procedure similar to that used for signal event candidates(described later).

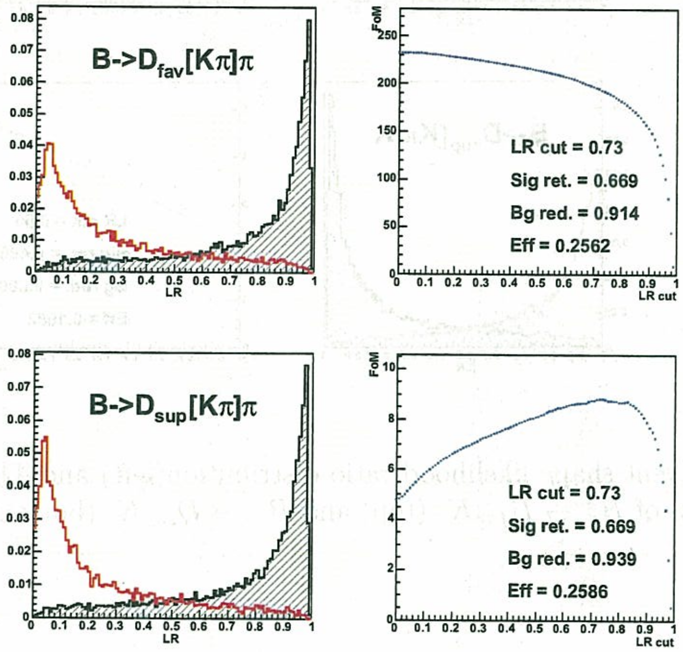

Figure 3.14: Event shape likelihood ratio distribution(left) and The "figure of merit" distribution(right) of $B^- \to D_{fav}\pi^-$(top) and $B^- \to D_{sup}\pi^-$(bottom)

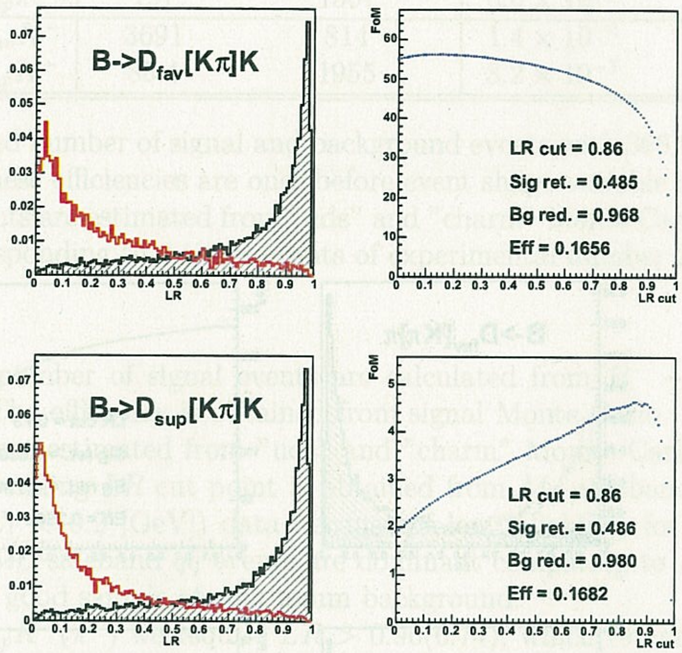

Figure 3.15: Event shape likelihood ratio distribution(left) and The "figure of merit" distribution(right) of $B^- \to D_{fav}K^-$(top) and $B^- \to D_{sup}K^-$(bottom)

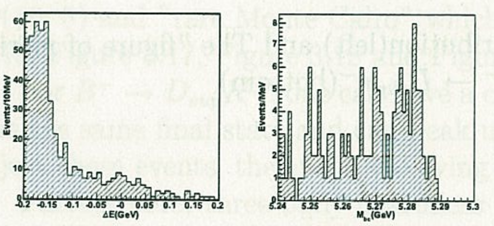

Figure 3.16: ΔE and m_{bc} distributions of generic Mote Carlo for $B^- \to D_{sup}\pi^-$

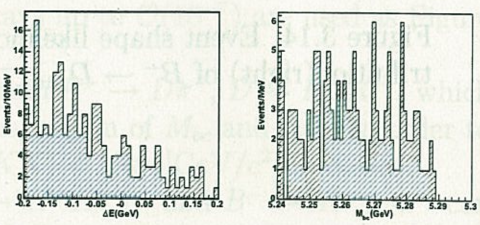

Figure 3.17: ΔE and m_{bc} distributions of generic Mote Carlo for $B^- \to D_{sup}K^-$

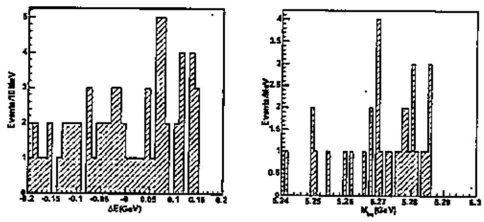

Figure 3.18: ΔE and m_{bc} distributions of rare Mote Carlo for $B^- \to D_{sup}\pi^-$

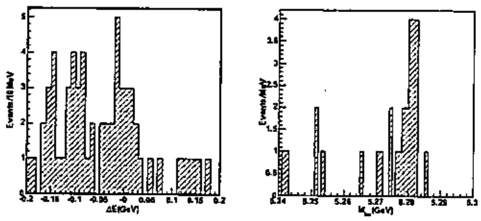

Figure 3.19: ΔE and m_{bc} distributions of rare Mote Carlo for $B^- \to D_{sup}K^-$

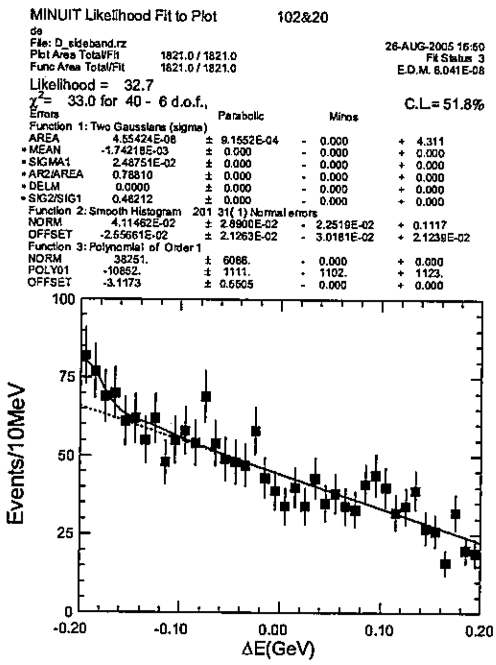

Figure 3.20: ΔE distribution of D mass sideband for $B^- \to D_{sup}\pi^-$ mode

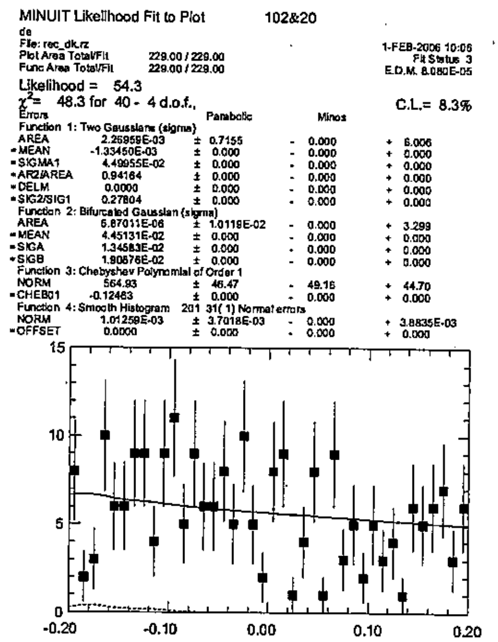

Figure 3.21: ΔE distribution of D mass sideband for $B^- \to D_{sup}K^-$ mode

For $B^- \to D_{sup}\pi^-$, the peaking background estimated by fitting the plot is consistent with zero. Since the Standard Model prediction for the $B^- \to D_{sup}\pi^-$ branching fraction is smaller than 10^{-11} [?], this background contribution is ignored.

For $B^- \to D_{sup}K^-$, its yield is also consistent with zero.

3.3 Results

3.3.1 Fitting the ΔE distributions

Component	Function	Parameter	Fit	$D\pi$	DK
Signal	Double-gaussian	area	float		
		mean	float→fix		
		σ_1	float→fix	○	○
		$\text{area}_2/\text{area}_1$	fix		
		σ_2/σ_1	fix		
$q\bar{q}$	Linear function	area	float	○	○
		slope	fix		
BB	Smoothed-histgram	area	float	○	○
feed-across	Bifurcated gaussian	area	float		
		mean	fix	×	○
		σ_1	fix		
		σ_2	fix		

Table 3.2: fitting component for $B^- \to D\pi^-/K^-$

To extract sinal yield ΔE fit is done assuming some fitting components as shown in Table 3.2. Regarding signal although its shape is naturally Breight-Wigner function, it is convoluted by experimental resolution as Gaussian. So in this case, double Gaussian which is sum of narrow width and wide width Gaussian, is good approximation. The mean and width are floated in favored mode fitting. In the suppressed mode, hese values are fixed to corresponding the favored mode results. The ratio of area and width are fixed to the value of corresponding signal Monte Carlo.

Regarding $q\bar{q}$ background its shape is modeled as a linear function. And its slope is determined from "uds" and "charm" Monte Carlo.

Backgrounds from other B decays, distribute as shown in Figure 3.22 and 3.23 . $B^- \to D\rho^-$and $B^- \to D^*\pi^-$ distribute in the negative ΔE region and make a small contribution to the signal region. These background shape is modeled as a smoothed histogram from generic Monte Carlo.

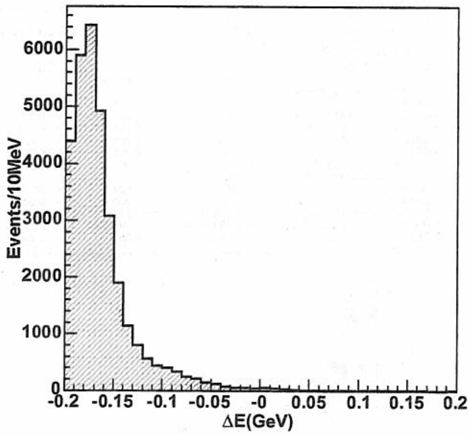

Figure 3.22: $B\bar{B}$ background of $B^- \to D_{fav}\pi^-$

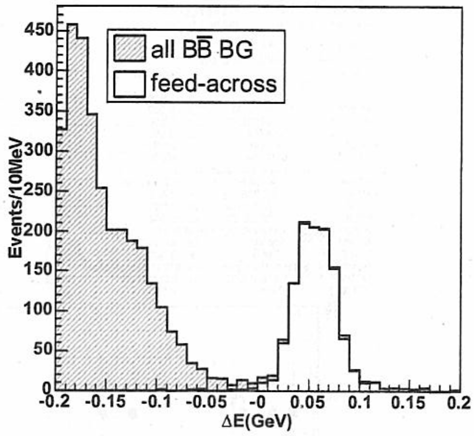

Figure 3.23: $B\bar{B}$ background of $B^- \to D_{fav}K^-$

For the $B^- \to DK^-$ decay mode, there is an additional component due to feed-across from $D_{fav}\pi^-$ as shown in Figure 3.23 by particle miss identification. Its contribution is modeled as a Gaussian shape that has different widths on the left and right sides of the peak(so-called Bifurcated gaussian), since the shift caused by wrong mass assignment makes the shape asymmetric. The widths and mean are determined by $B^- \to D_{fav}\pi^-$ data reconstruction with changing mass assignment for K.

The fit results are shown in Figure 5.26, Figure 5.27, Figure 3.26 and Figure 3.27. The numbers of events for $B^- \to D_{sup}h^-$ and $B^- \to D_{fav}h^-$ are given in Table 5.1.

Mode	Efficiency(%)	Signal Yield
$B^- \to D_{fav}\pi^-$	25.6 ± 0.3	15051 ± 126.8
$B^- \to D_{sup}\pi^-$	25.9 ± 0.3	52.2 ± 10.5
$B^- \to D_{fav}K^-$	16.6 ± 0.2	723 ± 31
$B^- \to D_{sup}K^-$	16.8 ± 0.2	10.1 ± 5.9

Table 3.3: Efficiency and signal yields.For the $B^- \to D_{sup}K^-$ signal yield, the second value is after subtraction of the peaking background.

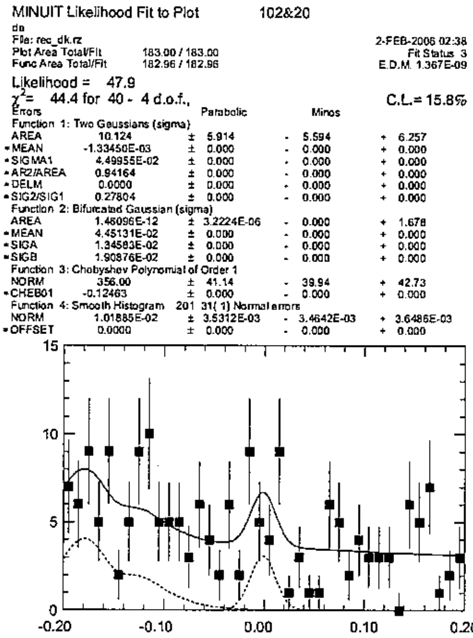

Figure 3.24: $B^- \to D_{sup}K^-$ ΔE-fit result

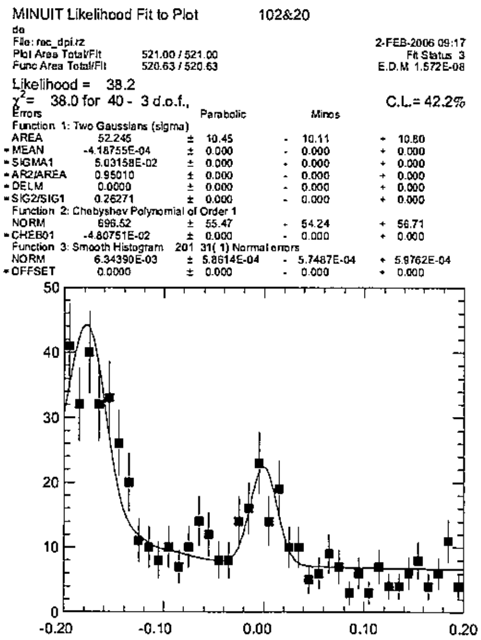

Figure 3.25: $B^- \to D_{sup}\pi^-$ ΔE-fit result

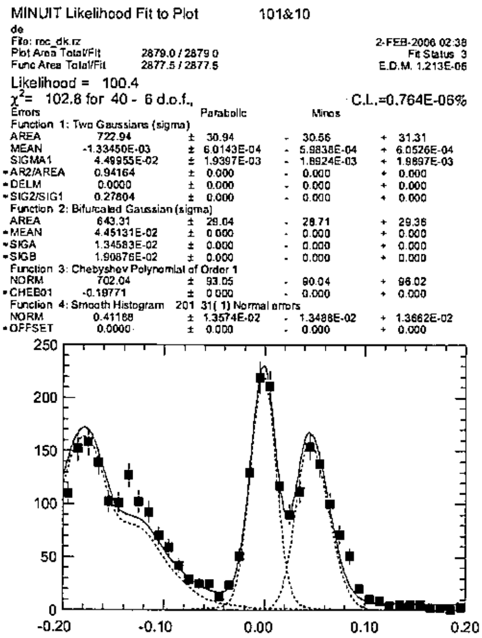

Figure 3.26: $B^- \to D_{fav}K^-$ ΔE-fit result

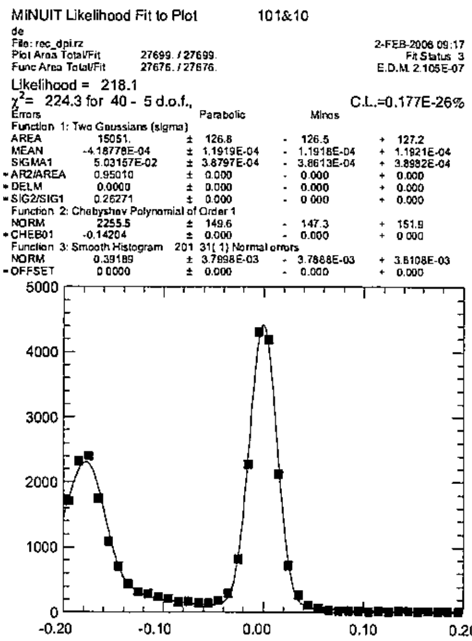

Figure 3.27: $B^- \to D_{fav}\pi^-$ ΔE-fit result

3.3.2 Ratio of branching fractions R_{Dh}

Ratios of product branching fractions, defined as

$$R_{Dh} \equiv \frac{\mathcal{B}(B^- \to D_{sup}h^-)}{\mathcal{B}(B^- \to D_{fav}h^-)} = \frac{N_{D_{sup}h^-}/\epsilon_{D_{sup}h^-}}{N_{D_{fav}h^-}/\epsilon_{D_{fav}h^-}},$$

are calculated where $N_{D_{sup}h^-}$ ($N_{D_{fav}h^-}$) and $\epsilon_{D_{sup}h^-}$ ($\epsilon_{D_{fav}h^-}$) are the number of signal events and the reconstruction efficiency for the decay $B^- \to D_{sup}h^-$ ($B^- \to D_{fav}h^-$), and are given in Table 5.1. I obtain

$$R_{DK} = (1.4 \pm 0.8(stat) \pm 0.1(syst)) \times 10^{-2},$$

$$R_{D\pi} = (3.5 \pm 0.7(stat)) \times 10^{-3}.$$

Since the signal for $B^- \to D_{sup}K^-$ is not significant, we set an upper limit as

$$R_{DK} < 2.8 \times 10^{-2} \quad 90\% \text{ confidence level}$$

where I take the likelihood function as a Gaussian distribution with width given by the quadratic sum of statistical and systematic errors, and the area is normalized in the physical region of positive branching fraction.

Most of the systematic uncertainties from the detection efficiencies and the particle identification are canceled by taking the ratios, since the kinematics of the $B^- \to D_{sup}h^-$ and $B^- \to D_{fav}h^-$ processes are similar. The systematic errors are due to uncertainties in the yield extraction and the efficiency difference between $B^- \to D_{sup}h^-$ and $B^- \to D_{fav}h^-$ as listed in Table 3.4.

Mode	$B^- \to D_{fav}K^-$	$B^- \to D_{sup}K^-$
signal shape	±0.4%	±4.6%
$q\bar{q}$ background	±0.2%	±1.3%
feed-across shape	±1.1%	±0.1%
$B\bar{B}$ background	±0.7%	±0.8%
efficiency	±0.4%	±0.4%
total	±1.4%	±4.9%

Table 3.4: Systematic uncertainties for $B^- \to D_{fav}K^-$ and $B^- \to D_{sup}K^-$ signal yield

The uncertainties in the signal shapes, the $q\bar{q}$ background shapes and feed-across shape are determined by varying the shape of the fitting function by $\pm 1\sigma$ which is fitting-error of reference . The uncertainties in the $B\bar{B}$ background shapes are determined by fitting the ΔE distribution in the region $-0.07 < \Delta E < 0.20$ [GeV] ignoring the $B\bar{B}$ background contributions. The uncertainties in the efficiency differences are determined using signal MC.

The total systematic error is the sum in quadrature of the above uncertainties. The ratio R_{DK} is related to ϕ_3 by the follwing equation

$$R_{DK} = r_B^2 + r_D^2 + 2 r_B r_D \cos\phi_3 \cos\delta \tag{3.3}$$

where [?]

$$r_B \equiv |\frac{A(B^- \to \bar{D}^0 K^-)}{A(B^- \to D^0 K^-)}|, \ \delta \equiv \delta_B + \delta_D,$$

$$r_D \equiv |\frac{A(D^0 \to K^+\pi^-)}{A(D^0 \to K^-\pi^+)}| = 0.060 \pm 0.003[PDG]$$

and δ_B (δ_D) are the strong phase differences between the two B (D) decay amplitudes, respectively. Using the above result, a limit on r_B is obtained. The least restrictive limit is obtained allowing $\pm 2\sigma$ variation on r_D and assuming maximal interference ($\phi_3 = 0°$, $\delta = 180°$ or $\phi_3 = 180°$, $\delta = 0°$) and is found to be

$$r_{B,DK} < 0.23 \text{ at the 90\% confidence level}$$

as shown in Figure 4.12.

3.3.3 Charge separated yield

CP violating asymmetry is searched in the $B^\pm \to D_{sup}K^\pm$ mode. The B^+ and B^- yields separately are determined as shown in Figure 3.29 and Figure 3.30. That yields are found to be 9.64 ± 4.8 events for $B^- \to D_{sup}K^-$ and 0.00 ± 3.4 events for $B^+ \to D_{sup}K^+$. And expediently quantities which related to these yields are defined as

$$A_{DK}^{\pm} \equiv \frac{\mathcal{B}(B^\pm \to D_{sup}K^\pm)}{(\mathcal{B}(B^- \to D_{fav}K^-) + \mathcal{B}(B^+ \to D_{fav}K^+))/2} \tag{3.4}$$

$$A_{DK}^{+} = (0.0 \pm 0.9(stat) \pm 0.1(syst)) \times 10^{-2} \tag{3.5}$$

$$A_{DK}^{-} = (1.3 \pm 0.9(stat) \pm 0.1(syst)) \times 10^{-2}. \tag{3.6}$$

(3.7)

Where systematic uncertainties arise from the B^+ and B^- yield extraction (4%; determined as for R_{DK}), detector charge asymmetry (2.5%; determined from the $B^- \to D_{fav}\pi^-$ sample [?]), and PID efficiency of prompt K(1%). The total systematic error is obtained by taking the quadratic sum.

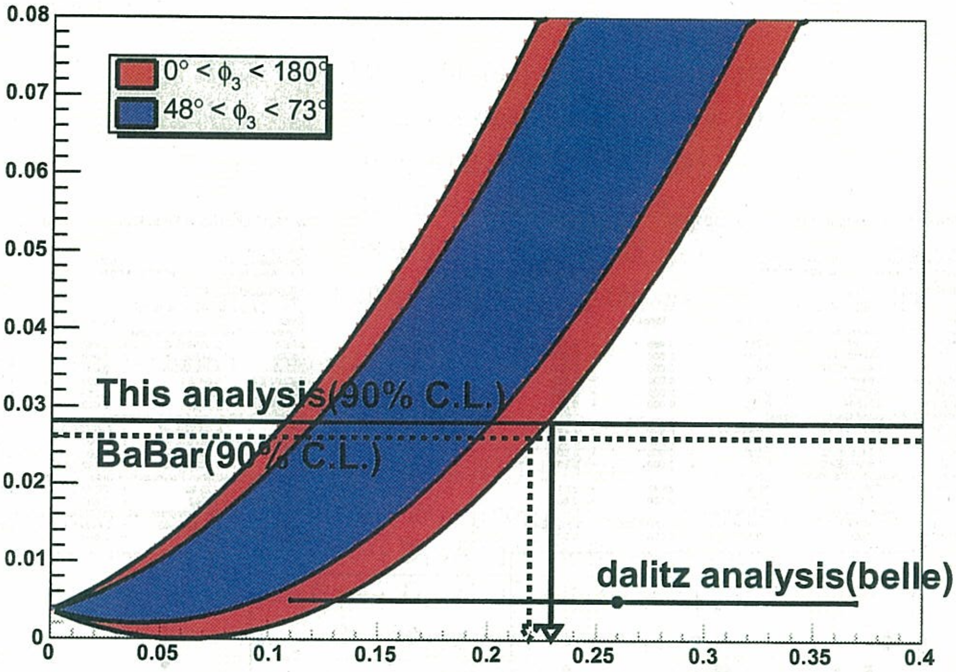

Figure 3.28: r_B dependence of R_{DK}

Yield extraction	±4%
Intrinsic detector bias	±2.5%
PID efficiency of prompt K	±1%
Total	±4.8%

Table 3.5: Systematic uncertainties for $A^{\pm}_{DK}$

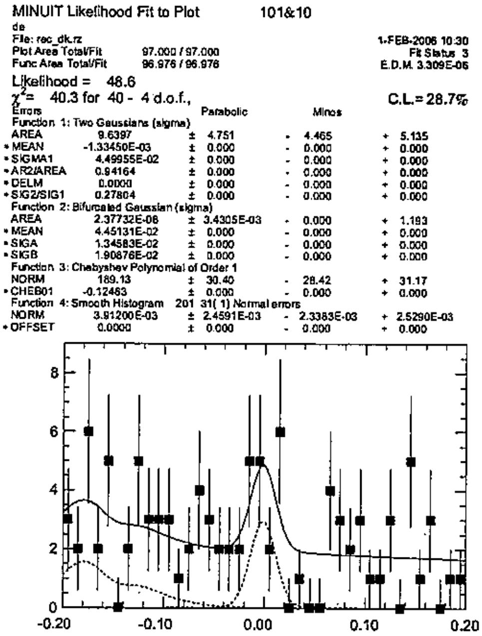

Figure 3.29: charge separated ΔE distribution of $B^- \to D_{sup}K^-$ mode

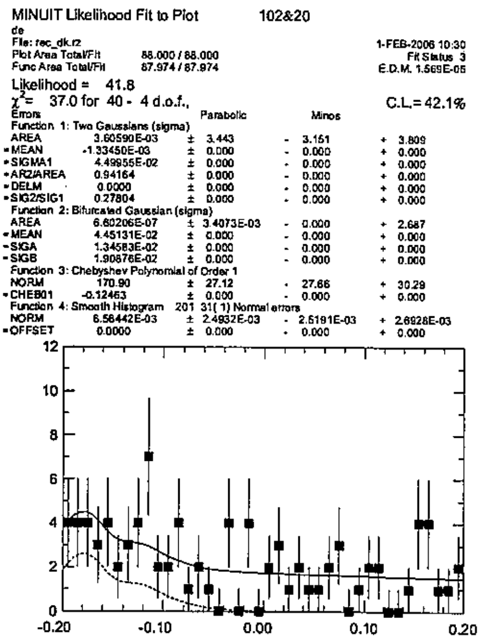

Figure 3.30: charge separated ΔE distribution of $B^+ \to D_{sup}K^+$ mode

3.3.4 Constraint for ϕ_3

The constraint for ϕ_3 is determined with the result of $B^- \to D_{CP}K^-$ analysis. To give a constraint the result of Belle previou
these data is used.

$$
\begin{aligned}
A^+_{DK} &= (0.0 \pm 0.9(stat) \pm 0.1(syst)) \times 10^{-2} && (3.8)\\
A^-_{DK} &= (1.3 \pm 0.9(stat) \pm 0.1(syst)) \times 10^{-2} && (3.9)\\
A_1 &= 0.07 \pm 0.14(stat) \pm 0.06(sys) && (3.10)\\
A_2 &= -0.11 \pm 0.14(stat) \pm 0.05(sys) && (3.11)\\
R_1 &= 0.98 \pm 0.18(stat) \pm 0.10(sys) && (3.12)\\
R_2 &= 1.29 \pm 0.16(stat) \pm 0.08(sys) && (3.13)
\end{aligned}
$$

Those observable are represented as

$$
\begin{aligned}
A^\pm_{DK} &\equiv \frac{\mathcal{B}(B^\pm \to D_{sup}K^\pm)}{(\mathcal{B}(B^- \to D_{fav}K^-) + \mathcal{B}(B^+ \to D_{fav}K^+))/2} && (3.14)\\
&= r_B^2 + r_D^2 + 2r_B r_D \cos(\delta \pm \phi_3) && (3.15)\\
A_{1,2} &\equiv \frac{B(B^- \to D_{1,2}K^-) - B(B^+ \to D_{1,2}K^+)}{B(B^- \to D_{1,2}K^-) + B(B^+ \to D_{1,2}K^+)} && (3.16)\\
&= \frac{2r_B \sin\delta'_{cp} \sin\phi_3}{1 + r_B^2 + 2r_B \cos\delta'_{cp} \cos\phi_3} && (3.17)\\
R_{1,2} &\equiv \frac{R^{D_{1,2}}}{R^{D^0}} && (3.18)\\
&= 1 + r_B^2 + 2r_B \cos\delta'_{cp} \cos\phi_3 && (3.19)\\
\delta'_{cp} &\equiv \begin{cases} \delta_{cp} & \text{for } D_1 \\ \delta_{cp} + \pi & \text{for } D_2 \end{cases} && (3.20)
\end{aligned}
$$

In these equation unknown values are ϕ_3, r_B, δ and δ_{cp}. Changing these parameters χ^2 between measured value and equation is obtained in each parameter space. Then using $\Delta\chi^2 = \chi^2 - \chi^2_{min}$ 1σ and 2σ favored region for each parameter is determined. And the result is shown in Figure 3.31.

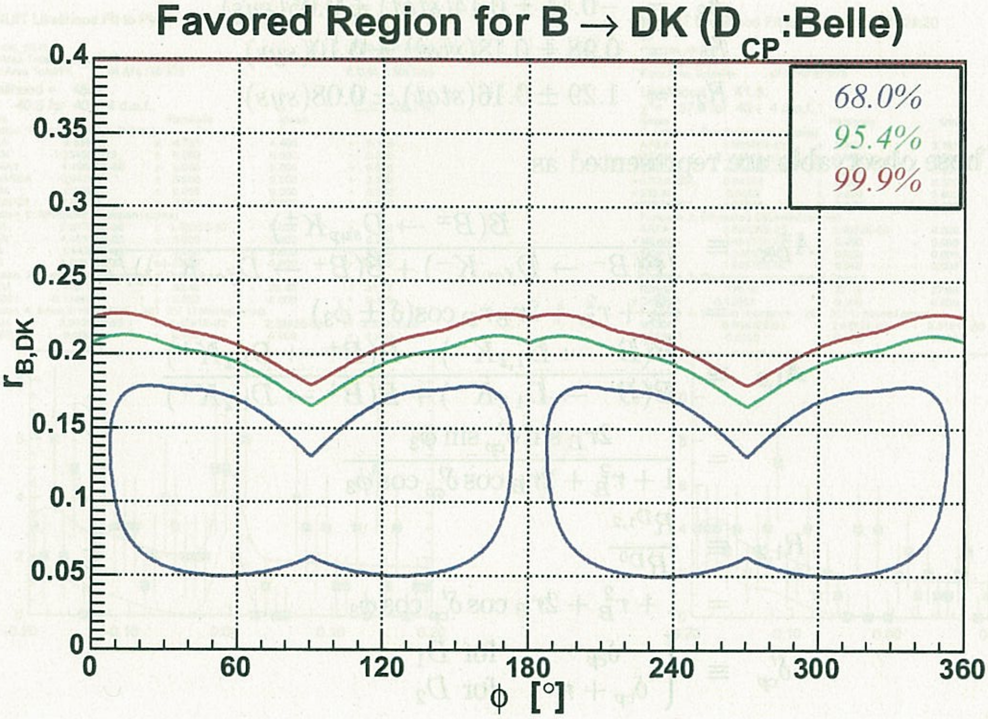

Figure 3.31: Constraint for ϕ_3 and r_B

Chapter 4

$B^- \to DK^{*-}$ analysis

In this chapter the procedure of $B^- \to DK^{*-}$ reconstruction is described. But almost of analysis procedures are same as $B^- \to DK^-$ analysis. So the description of the same cuts is skipped.

Historically the discovery of $B^- \to DK^{*-}$ decay is earlier than the discovery of $B^- \to DK^-$ decay. Even if $B^- \to D_{sup}[K^+\pi^-]K^-$ decay is not found, we may find $B^- \to D_{sup}[K^+\pi^-]K^{*-}$ decay.

4.1 Event selection criteria

4.1.1 K^{*-} reconstruction

- π tracks : $LR(K/\pi) < 0.7$
- Ks mass : $489 < M_{\pi^+\pi^-} < 507$ [MeV/c^2](3σ)
- good K_s : Depending on momentum range these cuts are applied.

Momentum[GeV/c]	dr[cm]	$d\phi$[cm]	z_{dist}[cm]	l_{flight}[cm]
< 0.5	> 0.05	< 0.3	< 0.8	-
$0.5 - 1.5$	> 0.03	< 0.1	< 1.8	> 0.08
> 1.5	> 0.02	< 0.03	< 2.4	> 0.22

where these parameters are defined as

- dr : This is the smaller of distances from IP in the direction perpendicular to beam axis ($x - y$ plane).
- $d\phi$: This is the angle between Ks and Ks daughter's momentum direction.

– z_{dist} : This is the distance between the two daughter tracks in IP.

– l_{flight} : This is the flight length of Ks candidate in $x-y$ plane.

- K^{*-} mass : $817 < M_{K_s\pi^-} < 967$ [MeV/c^2]

K^{*-} candidates are reconstructed by combining K_s and π^-. K_s candidates are required to have a mass within ± 9 MeV/c^2 (3σ) of its nominal mass value(Figure 4.1) and certain flight length depending its momentum. In K^{*-} reconstruction PID cut of π candidates are same as one of D daughter π. K^{*-} candidates are required to have a mass within ± 75 MeV/c^2 of its nominal mass value as shown in Figure 4.2.

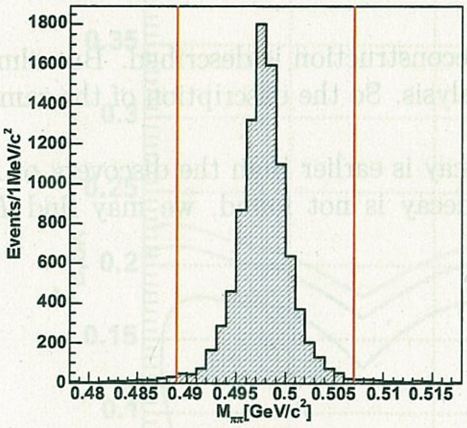

Figure 4.1: K_s mass distribution of signal Mote Carlo evnts

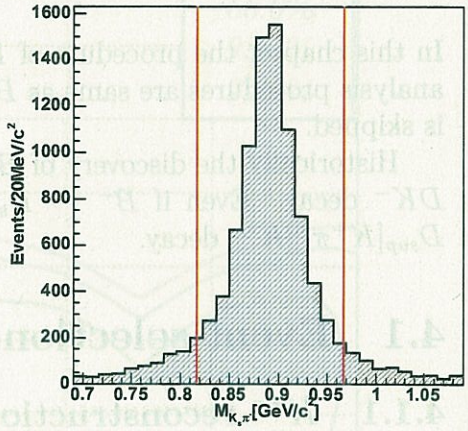

Figure 4.2: K^{*-} mass distribution of signal Mote Carlo events

4.1.2 B^- reconstruction

- $5.27 < M_{bc} < 5.29$[GeV/c^2]
- $|\Delta E| < 0.05$[GeV]
- $|\cos\theta_{hel}| > 0.4$

B^- candidates are reconstructed by combining D and K^{*-} candidate satisfying the condition. In addition to M_{bc} and ΔE cut B^- candidates are required to helicity angle cut, $|\cos\theta_{hel}| > 0.4$. Since $B^- \to DK^{*-}$ decay is a pseudoscaler to pseudoscaler-vector decay, the K^{*-} is polarized. The K^{*-} helicity angle, θ_{hel}, is defined as angle between the momentum direction of one K^{*-} daughter and B in K^{*-} rest frame. By pseudoscaler to pseudoscaler-vector decay that helicity angles have $\cos^2\theta_{hel}$ distribution as shown in Figure 4.3. And this cut is also effective for combinatoric background and $q\bar{q}$ continuum background supression because those distributions are essentially flat.

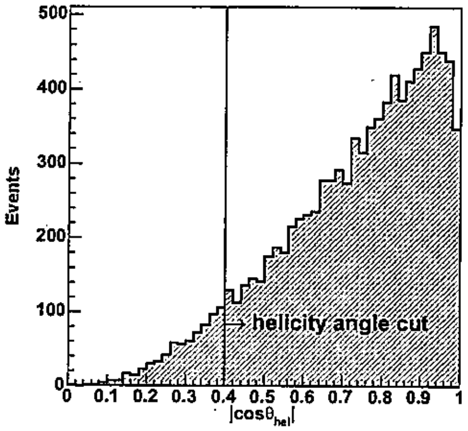

Figure 4.3: helicity angle distribution of signal Mote Carlo events

After applying all these cuts the distributions of ΔE and M_{bc} are shown in Figure 4.4, where the data set is signal Monte carlo events.

4.1.3 $q\bar{q}$ continuum background suppression

- $LR_{(KSFW,cos\theta_B)} > 0.88$

Mode	#(signal)	#(background)	Expected $\mathcal{B}$	Efficiency(%)
$B^- \to D_{fav}K^{*-}$	724	233	5.2×10^{-6}	18.0
$B^- \to D_{sup}K^{*-}$	33.7	247	1.9×10^{-8}	19.3

Table 4.1: Expected number of signal and background events with 366 fb^{-1} data set (386×10^6 $B\bar{B}$ pairs). These efficiencies are ones before event shape variable cut. These numbers of background events are estimated from "uds" and "charm" Monte Carlo events whose size are 532 fb^{-1} corresponding to 3 times events of experimental number 21 to 37(177.4fb^{-1}).

To suppress $q\bar{q}$ continuum background the event shape likelihood ratio cut is optimized for $B^- \to D_{sup}[K^+\pi^-]K^{*-}$ mode. In that optimization "figure of merit" is used as a indicator. Figure 4.5 shows likelihood ratio distribution of signal Monte Carlo and M_{bc}

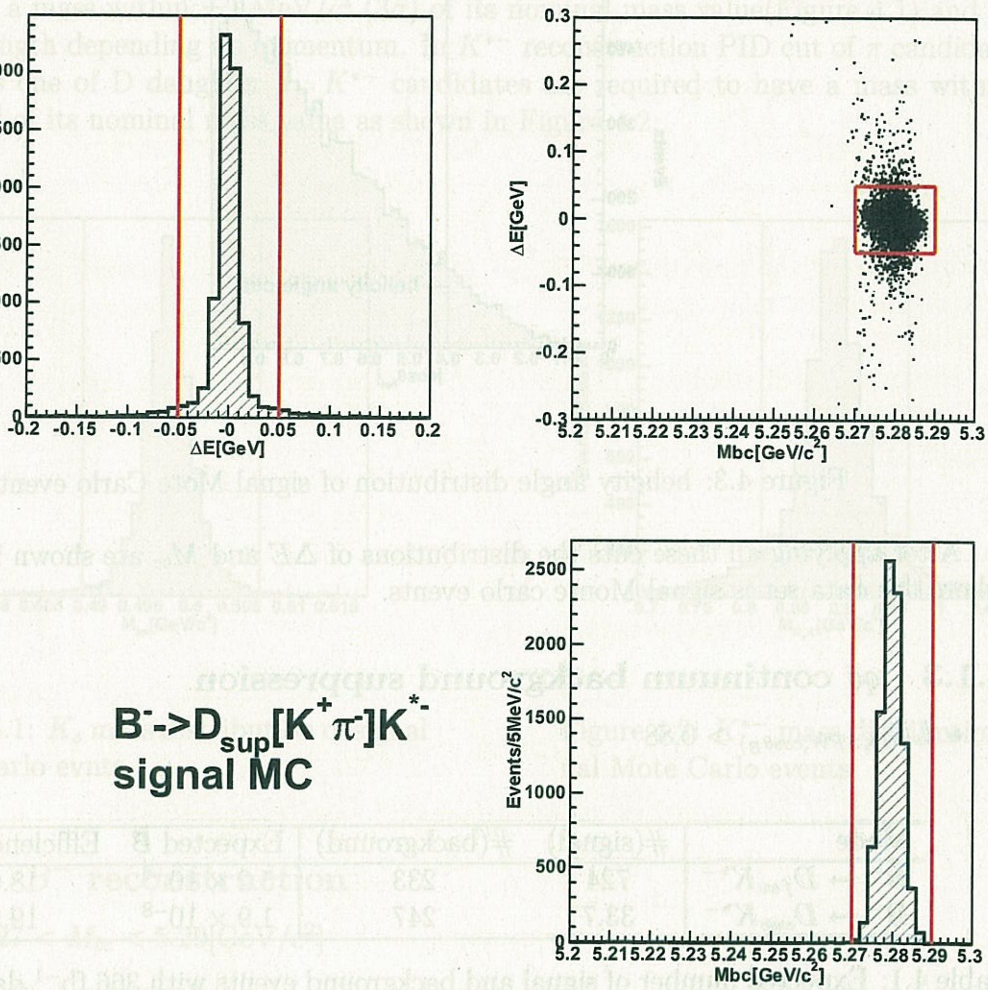

Figure 4.4: ΔE and M_{bc} distribution of signal Mote Carlo events

sideband data and "figure of merit"(F.o.M) distribution as a function of likelihood ratio cut point. The number of $q\bar{q}$ continuum background events is estimated from "uds" and "charm" Monte Carlo. On the other hand the number of signal events is estimated from central value of BaBar's result (R_{DK^*}) and PDG product branching fraction as

$$\begin{aligned}
\mathcal{B}(B^- \to DK^{*-}) &= 6.1 \times 10^{-4} \\
\mathcal{B}(D^0 \to K^-\pi^+) &= 3.8 \times 10^{-2} \\
\mathcal{B}(K^{*-} \to K^0\pi^-) &= \frac{2}{3} \\
\mathcal{B}(K^0 \to K_s \to \pi^+\pi^-) &= \frac{1}{2} \times \frac{2}{3} \\
R_{DK^*} &= \frac{\mathcal{B}(B^- \to D_{sup}K^{*-})}{\mathcal{B}(B^- \to D_{fav}K^{*-})} \\
&= 0.046
\end{aligned}$$

4.1.4 Peaking background

To check the peaking background "generic Monte Carlo" events and "rare Monte Carlo" events are used. The results for ΔE and M_{bc} distributions are shown in Figure 4.6 and Figure 4.7.

But for $B^- \to D_{sup}[K^+\pi^-]K^{*-}$ mode particular background source is not found in signal region .

To check the effect of $B^- \to K^+\pi^-K^{*-}$ decay I also check the D mass sideband as shown in Figure 4.8. But there is no peak.

4.2 Results

4.2.1 Fitting the ΔE distributions

To extract sinal yield ΔE fit is done assuming some fitting components as shown in Table 4.2.

Backgrounds from other B decays distribute as shown in Figure 4.9. The treatments of background, $B\bar{B}$ background and continuum background, is same as $B^- \to DK^-$ analysis. But we need not pay attention for feed-across because there is no mode corresponding to $B^- \to DK^{*-}$ mode such as $B^- \to D\pi^-$ decay feed-across in $B^- \to DK^-$ reconstruction. For fit of signal the sum of two Gaussian distributions which have same mean are used where its these relative width and area are determined from signal Monte Carlo.

In the fit of the ΔE distribution for $B^- \to D_{fav}K^{*-}$ mode, the free parameters are the position, widths and area of the signal peak, the slope and normalization of the continuum component and the normalization of the $B\bar{B}$ background.

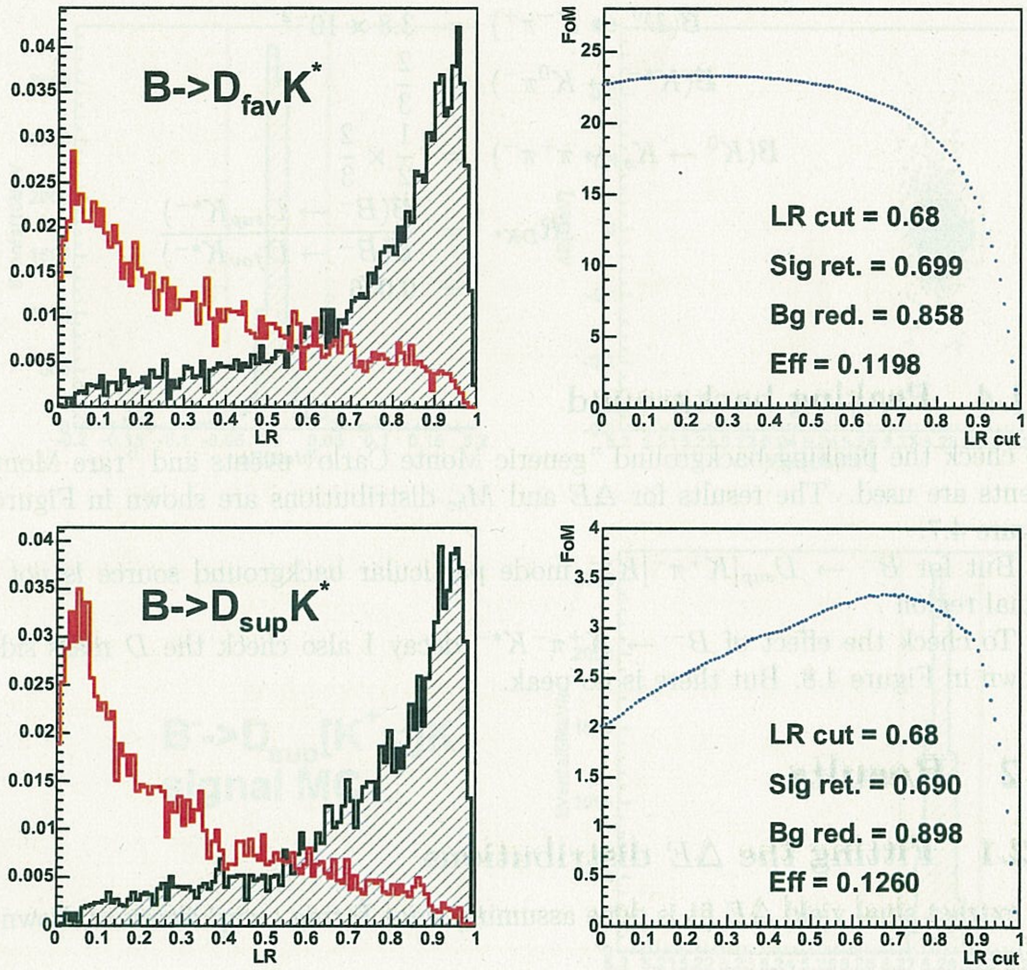

Figure 4.5: The event shape likelihood ratio distribution(left) and The "figure of merit" distribution(right)

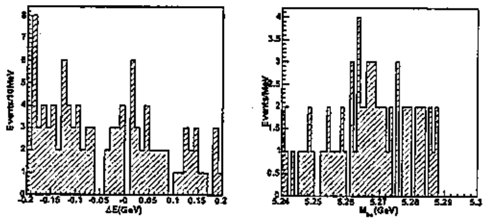

Figure 4.6: ΔE distribution of "generic Mote Carlo" evnts for $B^- \to D_{sup}[K^+\pi^-]K^{*-}$

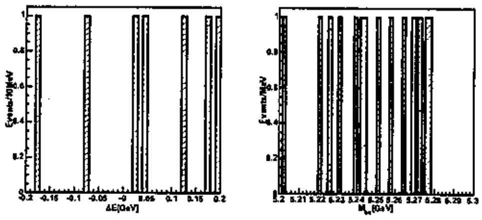

Figure 4.7: ΔE distribution of "rare Mote Carlo" evnts for $B^- \to D_{sup}[K^+\pi^-]K^{*-}$

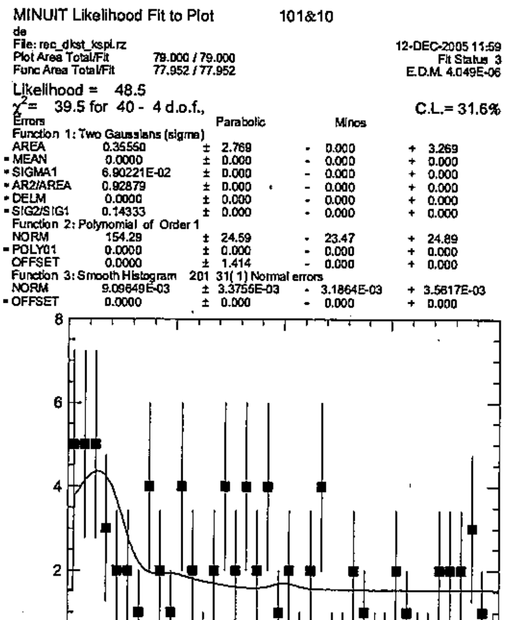

Figure 4.8: ΔE distribution of D mass sideband Data for $B^- \to D_{sup}[K^+\pi^-]K^{*-}$

Component	Function	Parameter	Fit
Signal	Double-gaussian	area	float
		mean	float→fix
		σ_1	float→fix
		$area_2/area_1$	fix
		σ_2/σ_1	fix
$q\bar{q}$	Linear function	area	float
		slope	fix
BB	Smoothed-histgram	area	float

Table 4.2: fitting components for $B^- \to DK^{*-}$

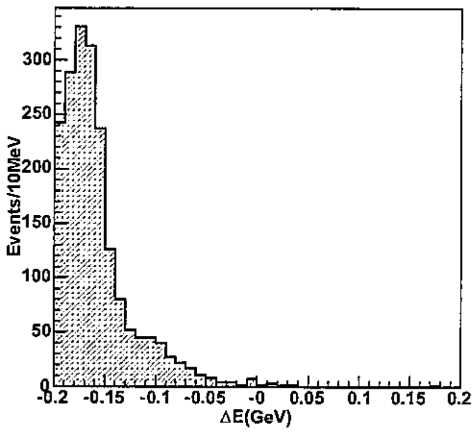

Figure 4.9: ΔE distribution of $B\bar{B}$ background for $B^- \to D_{fav}[K^-\pi^+]K^{*-}$

For $B^- \to D_{sup}K^{*-}$, the signal and $B\bar{B}$ background shapes are modeled using the results of the fits to the corresponding favored modes. The free parameters are the normalization of the three components, and the slope of the continuum.

The fit results are shown in Figure 4.10 and Figure 4.11. The numbers of signal yield are listed in Table 4.3

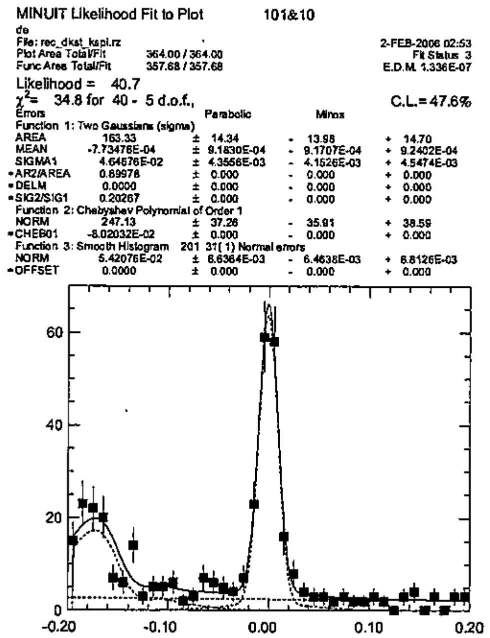

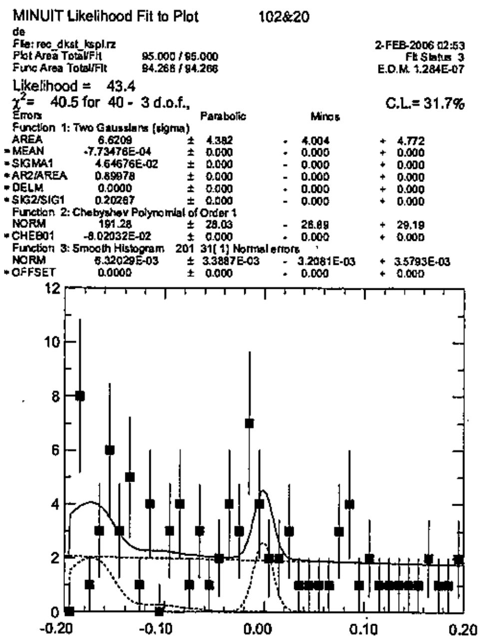

Figure 4.10: $B^- \to D_{fav}K^{*-}$ ΔE-fit result   Figure 4.11: $B^- \to D_{sup}K^{*-}$ ΔE-fit result

Mode	Efficiency(%)	Signal Yield
$B^- \to D_{sup}K^{*-}$	12.0 ± 0.2	163 ± 14.3
$B^- \to D_{fav}K^{*-}$	12.6 ± 0.2	6.2 ± 4.4

Table 4.3: Efficiency and signal yields of $B^- \to DK^{*-}$ mode

4.2.2 Ratio of branching fractions R_{Dh}

In $B^- \to DK^{*-}$ mode the ratio of product branching fraction is calcurated using the numer of signal events and efficiency listed in Table 4.3.

I obtain

$$R_{DK^*} = (3.9 \pm 2.7(stat) \pm 0.4(sys)) \times 10^{-2}.$$

Since the signal for $B^- \to D_{sup}K^{*-}$ is not significant, I set an upper limit as

$$R_{DK^{*-}} < 8.7 \times 10^{-2} \quad 90\% \text{ confidence level}$$

,where I take the likelihood function as a Gaussian distribution with width given by the quadratic sum of statistical and systematic errors. The systematic errors are due to uncertainties in the yield extraction and the efficiency difference between $B^- \to D_{fav}K^{*-}$ and $B^- \to D_{sup}K^{*-}$ as listed in Table 4.4.

Mode	$B^- \to D_{fav}K^-$	$B^- \to D_{sup}K^-$
signal shape	±0.6%	±18.5%
$q\bar{q}$ background	±0.2%	±6.9%
$B\bar{B}$ background	±1.9%	±1.7%
efficiency	±0.2%	±0.2%
total	±1.4%	±19.8%

Table 4.4: Systematic uncertainties for $B^- \to D_{fav}K^{*-}$ and $B^- \to D_{sup}K^{*-}$ signal yield

The ratio R_{DK^*} is related to ϕ_3 by following equation

$$R_{DK^*} = r_B^2 + r_D^2 + 2r_{B,DK^*}r^D \cos\phi_3 cos\delta,$$

where

$$r_{B,DK^*} \equiv |\frac{A(B^- \to \bar{D}^0K^{*-})}{A(B^- \to D^0K^{*-})}|$$

and with the same way as $B^- \to DK^-$ analysis the upper limit is obtained as

$$r_{B,DK^*} < 0.35 \text{ at the } 90\% \text{ confidence level}$$

, as shown in Figure 4.12.

4.2.3 Charge separated yield

CP violating asymmetry is searched in the $B^\pm \to D_{sup}K^{*\pm}$ mode. The B^+ and B^- yields separately are determined as shown in Figure 4.13 and Figure 4.14. That yields are found to be 4.8 ± 3.1 events for $B^- \to D_{sup}K^{*-}$ and 1.1 ± 3.1 events for $B^+ \to D_{sup}K^{*+}$. And

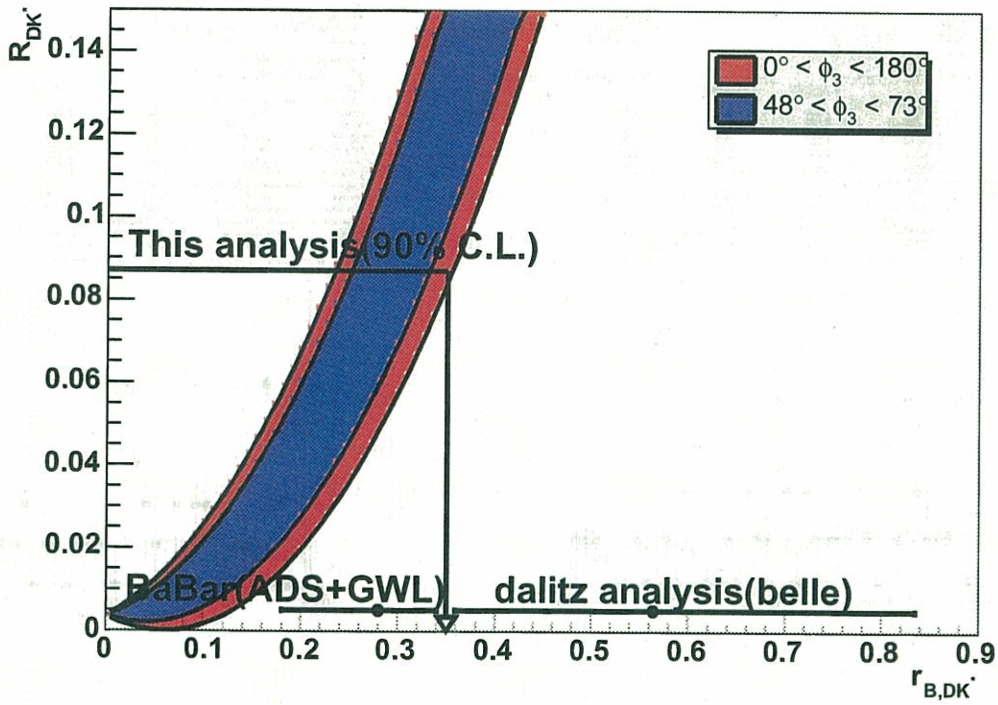

Figure 4.12: r_{B,DK^*} dependence of R_{DK^*}

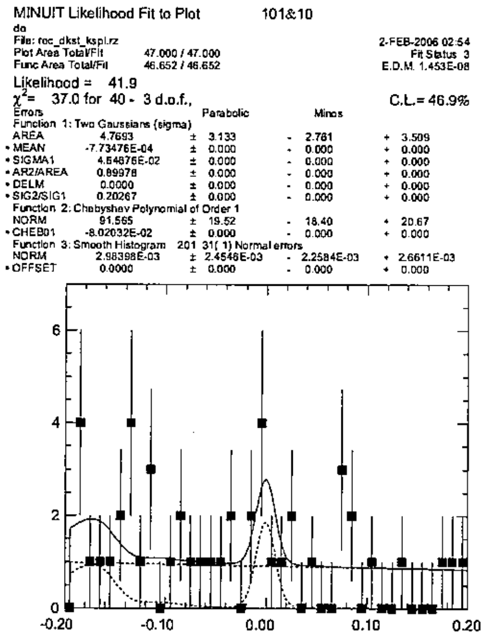

Figure 4.13: charge separated ΔE distribution of $B^- \to D_{sup}K^{*-}$ mode

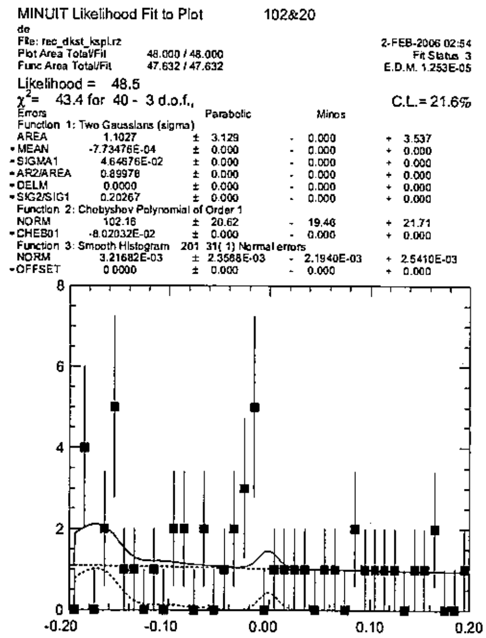

Figure 4.14: charge separated ΔE distribution of $B^+ \to D_{sup}K^{*+}$ mode

expediently quantities which related to these yields are defined as

$$A^{\pm}_{DK} \equiv \frac{\mathcal{B}(B^{\pm} \to D_{sup}K^{*\pm})}{(\mathcal{B}(B^{-} \to D_{fav}K^{*-}) + \mathcal{B}(B^{+} \to D_{fav}K^{*+}))/2} \quad (4.1)$$

$$A^{+}_{DK} = (1.4 \pm 3.8(sta) \pm 0.2) \times 10^{-2} \quad (4.2)$$

$$A^{-}_{DK} = (6.1 \pm 3.8(sta) \pm 0.9) \times 10^{-2}. \quad (4.3)$$

$$(4.4)$$

where systematic uncertainties arise from the B^+ and B^- yield extraction (11.1%; determined as for R_{DK^*}) and detector charge asymmetry (2.5%; determined from the $B^- \to D_{fav}\pi^-$ sample [?]). The total systematic error is obtained by taking the quadratic sum.

Yield extraction	±11.1%
Intrinsic detector bias	±2.5%
Total	±11.2%

Table 4.5: Systematic uncertainties for A_{DK^*}

4.2.4 Constraint for ϕ_3

Using result of this analysis and BaBar's measurement of $B^- \to D_{CP}K^{*-}$ as bellow, a constraint for ϕ_3 is determined.

$$A^{+}_{DK} = (1.4 \pm 3.8(sta) \pm 0.2) \times 10^{-2} \quad (4.5)$$

$$A^{-}_{DK} = (6.1 \pm 3.8(sta) \pm 0.9) \times 10^{-2} \quad (4.6)$$

$$A_1 = -0.08 \pm 0.19(stat) \pm 0.08(sys) \quad (4.7)$$

$$A_2 = -0.26 \pm 0.40(stat) \pm 0.12(sys) \quad (4.8)$$

$$R_1 = 1.96 \pm 0.40(stat) \pm 0.11(sys) \quad (4.9)$$

$$R_2 = 0.65 \pm 0.26(stat) \pm 0.08(sys) \quad (4.10)$$

The same method as $B^- \to DK^-$ analysis is used to give a constraint for $\phi - r_{B,DK^*}$. The result as shown in Figure 4.15 is obtained.

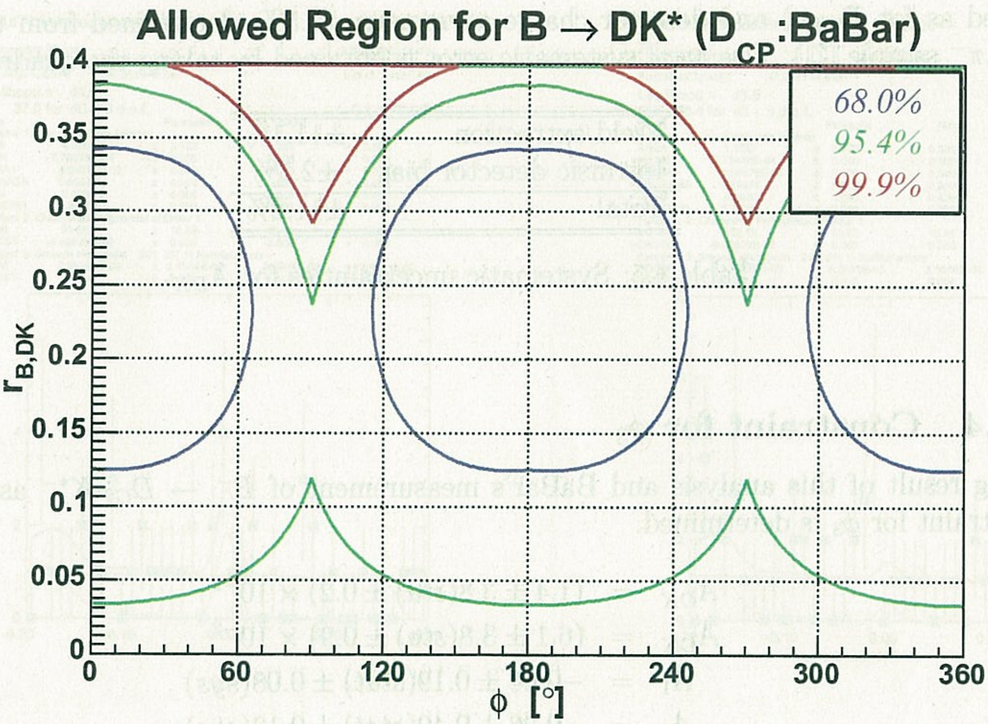

Figure 4.15: Constraint for ϕ_3 and r_{B,DK^*}

Chapter 5

$B^- \to D^*K^-$ analysis

In this chapter the procedure of $B^- \to D^*K^-$ reconstruction is described. But almost of analysis procedures are same as $B^- \to DK^-$ analysis. So the description of same cuts are skipped. To confirm my analysis method $B^- \to D^*\pi^-$ mode is also analyzed.

In this analysis product branching ratios, $R_{D^*[D\pi^0]K}$ and $R_{D^*[D\gamma]K}$, are measured. Since there is theoretical relation between product branching ratios and r_{B,D^*K} as $r_{B,D^*K}^2 = \frac{R_{D^*[D\pi^0]K}+R_{D^*[D\gamma]K}}{2} - r_D^2$, strong constraint for r_{B,D^*K} is extracted. That information of r_{B,D^*K} is important input for ϕ_3 determination.

5.1 Event selection criteria

5.1.1 D^{*-} reconstruction

- mass difference : $\Delta m \equiv m_{D^*} - m_D$
  - $139 < \Delta m < 145$ [MeV] (3σ) for $D\pi^0$ mode
  - $131 < \Delta m < 147$ [MeV] (2σ) for $D\gamma$ mode
- π^0 selection
  - γ energy : $E_\gamma > 30$ MeV
  - mass χ^2 : $\chi^2_{m_{\pi^0}} \equiv \frac{m_{\gamma\gamma} - m_{\pi^0}^{nominal}}{\sigma} < 25$
- γ selection (these cuts is not applied to π daughters)
  - γ energy : $E_\gamma > 150$ MeV
  - π^0 χ^2 : $\chi^2_{m_{\pi^0}} > 10$

D^* candidates are reconstructed by combination of $D\pi^0$ or $D\gamma$. To get D^*candidates effectively mass difference(Δm) is used instead of D^* mass. Its cut value corresponds to 3σ or 2σ of experimental resolution as Figure 5.1 and Figure 5.2 And in the case of $D\gamma$ mode its range is asymmetric because of shower leakage in the calorimeter(ECL).

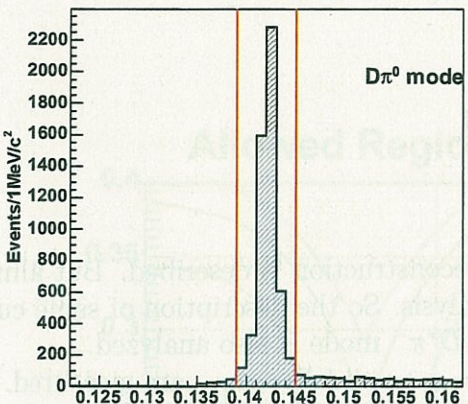

Figure 5.1: Δm distribution of signal Mote Carlo evnts in $D\pi^0$ mode

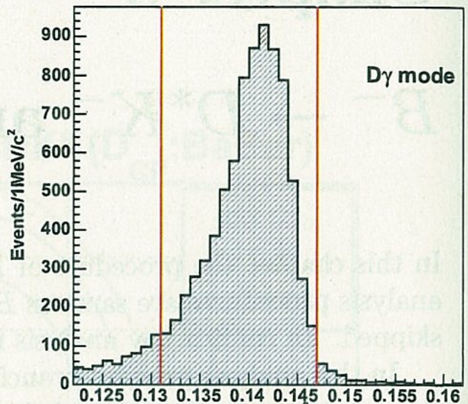

Figure 5.2: Δm distribution of signal Mote Carlo evnts in $D\gamma$ mode

π^0 candidates are reconstructed by combining of two γs whose energy is grater than 30 MeV to suppress low energy π^0 fake. And it's mass χ^2 is required to be smaller than 25.

By low energy γ background $B^- \to Dh^-$ makes background for $B^- \to D^*h^-$. But that fake γ events are distinguished by γ energy as shown in Figure 5.3. For γ from D^* its energy is required to be grater than 150 MeV. To suppress low energy γ background this cut is tighter than one of π^0 daughters. π^0 veto is also used to suppress the contamination. Checking the all combination of γs, one which can form π^0, $\chi^2_{m_{\pi^0}} < 10$, is rejected.

5.1.2 B^- reconstruction

- $5.27 < M_{bc} < 5.29[\mathrm{GeV}/c^2]$
- $|\Delta E| < 0.05[\mathrm{GeV}]$

B^- candidates are reconstructed by combination of D^*K^- or $D^*\pi^-$ candidate satisfying the condition.

Typical ΔE and M_{bc} distributions of $B^- \to D^*K^-$ modes are plotted in Figure 5.4 and 5.5 .

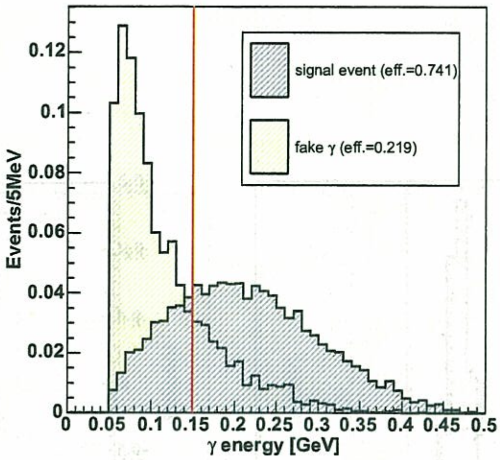

Figure 5.3: γ energy distributions of signal and fake γ events

5.1.3 $q\bar{q}$ continuum background suppression

- $D^*[D\pi^0]\pi^-$ mode :$LR_{(KSFW,cos\theta_B)} > 0.59$
- $D^*[D\pi^0]K^-$ mode : $LR_{(KSFW,cos\theta_B)} > 0.80$
- $D^*[D\gamma]\pi^-$ mode :$LR_{(KSFW,cos\theta_B)} > 0.89$
- $D^*[D\gamma]K^-$ mode : $LR_{(KSFW,cos\theta_B)} > 0.90$

To suppress $q\bar{q}$ continuum background the event shape likelihood ratio cut is optimized for each suppressed mode based on "figure of merit" (F.o.M) Figure 5.6 - 5.9 shows likelihood ratio distribution of signal Monte Carlo and M_{bc} sideband data and F.o.M distribution as a function of likelihood ratio cut point for each mode. The number of $q\bar{q}$ continuum background events is estimated from Monte Carlo. On the other hand the number of signal events is estimated from PDG product branching fraction as

$$\begin{aligned}
\mathcal{B}(B^- \to D^{*0}\pi^- \;/\; D^{*0}K^-) &= 4.6\times10^{-3} \;/\; 3.6\times10^{-4} \\
\mathcal{B}(D^{*0} \to D^0\pi^0 \;/\; D^0\gamma) &= \frac{2}{3} \;/\; \frac{1}{3} \\
\mathcal{B}(D^0 \to K^-\pi^+ \;/\; K^+\pi^-) &= 3.8\times10^{-2} \;/\; 1.38\times10^{-4}
\end{aligned}$$

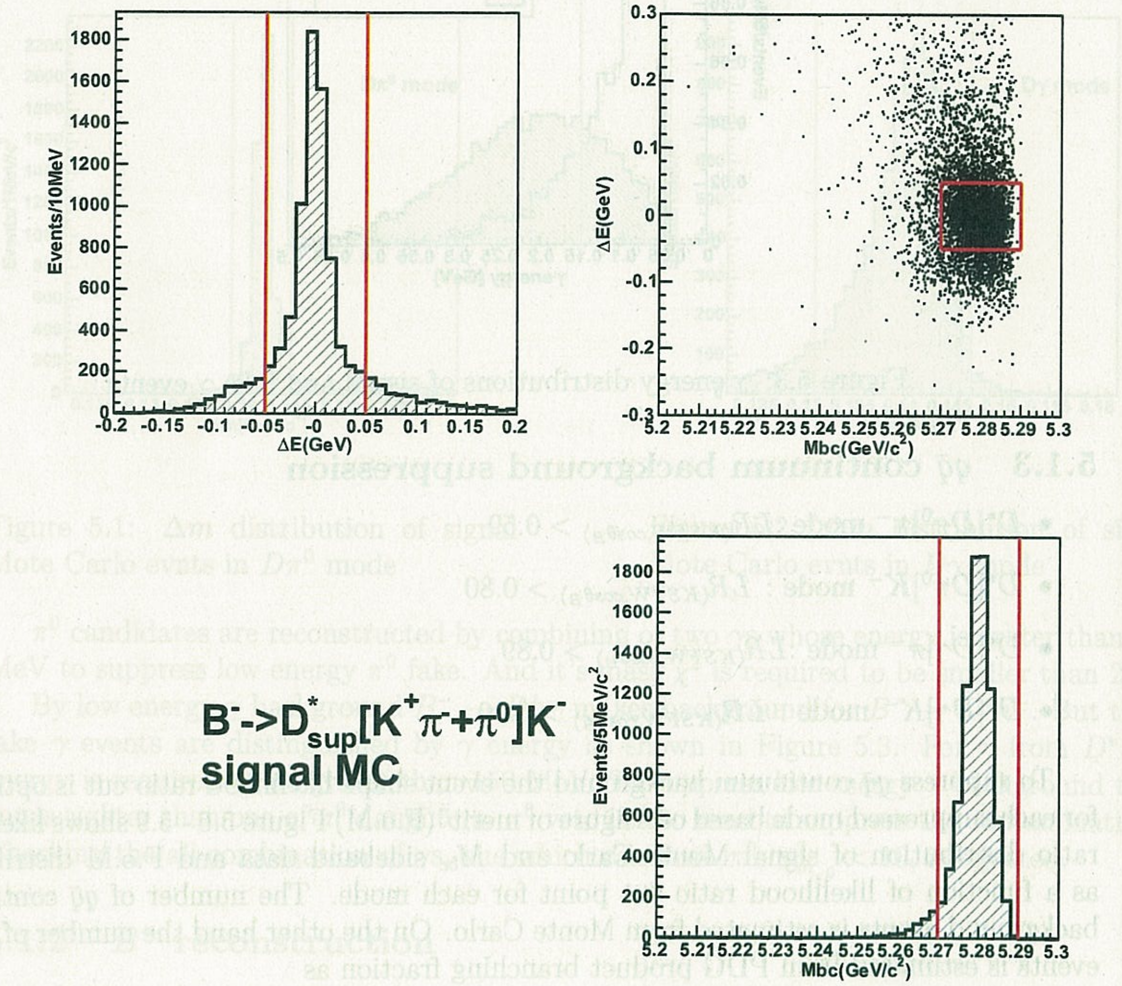

Figure 5.4: ΔE and M_{bc} distribution of signal Mote Carlo events in $B^- \rightarrow D^*[D\pi^0]K^-$ mode

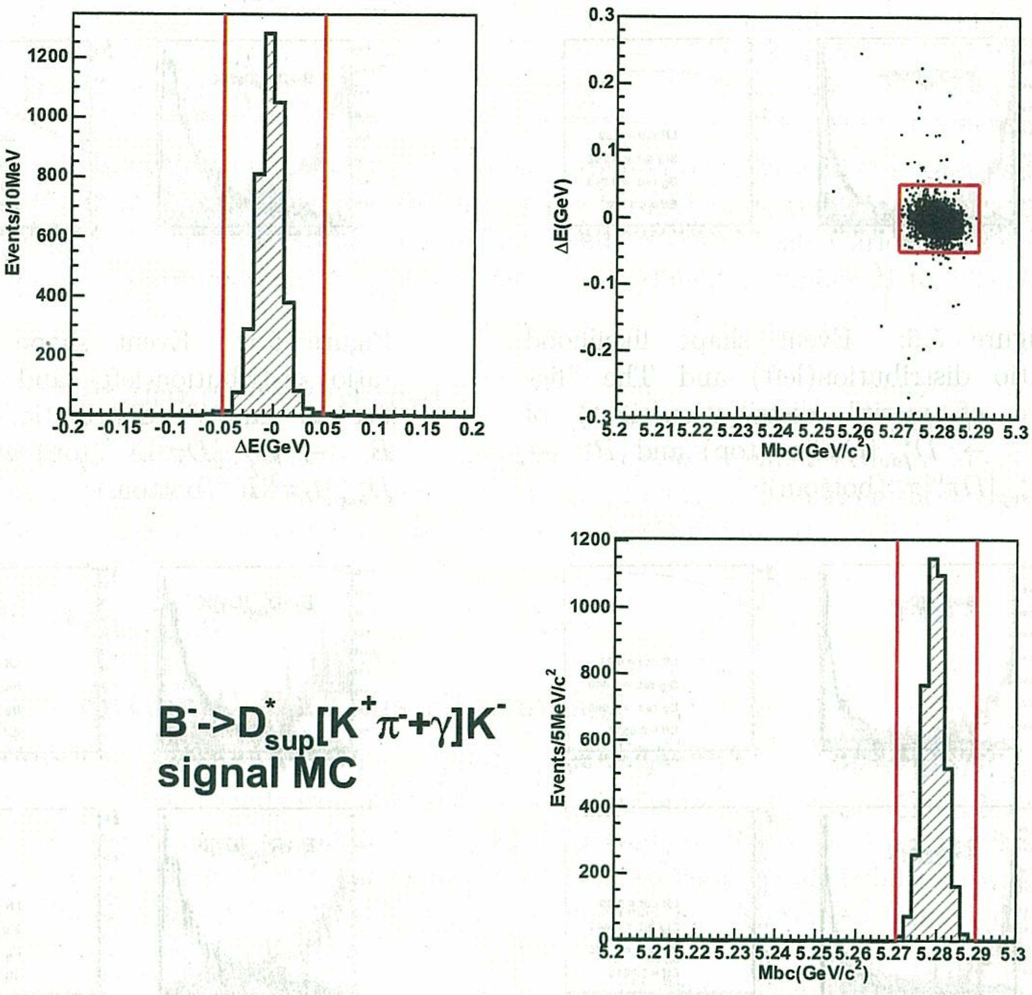

Figure 5.5: ΔE and M_{bc} distributions of signal Mote Carlo events in $B^- \to D^*[D\gamma]K^-$

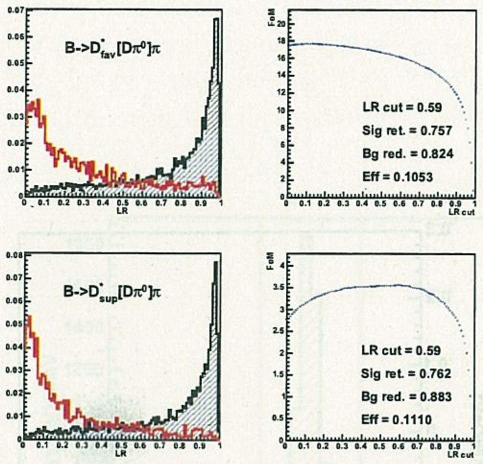

Figure 5.6: Event shape likelihood ratio distribution(left) and The "figure of merit" distribution(right) of $B^- \rightarrow D^*_{fav}[D\pi^0]\pi^-$(top) and $B^- \rightarrow D^*_{sup}[D\pi^0]\pi^-$(bottom)

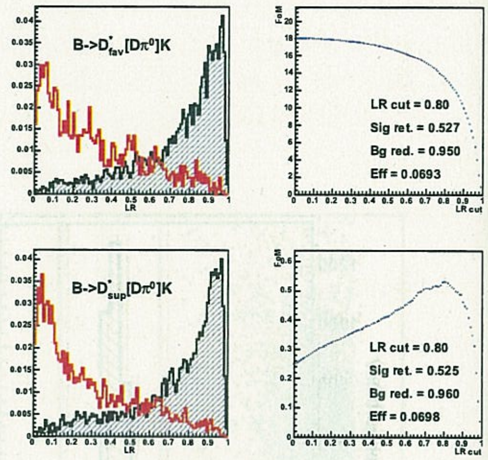

Figure 5.7: Event shape likelihood ratio distribution(left) and The "figure of merit" distribution(right) of $B^- \rightarrow D^*_{fav}[D\pi^0]K^-$(top) and $B^- \rightarrow D^*_{sup}[D\pi^0]K^-$(bottom)

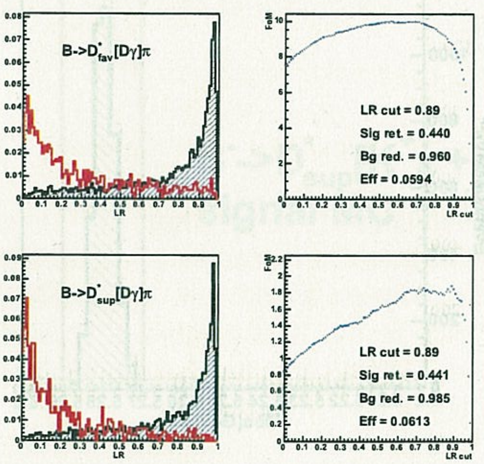

Figure 5.8: Event shape likelihood ratio distribution(left) and The "figure of merit" distribution(right) of $B^- \rightarrow D^*_{fav}[D\gamma]\pi^-$(top) and $B^- \rightarrow D^*_{sup}[D\gamma]\pi^-$(bottom)

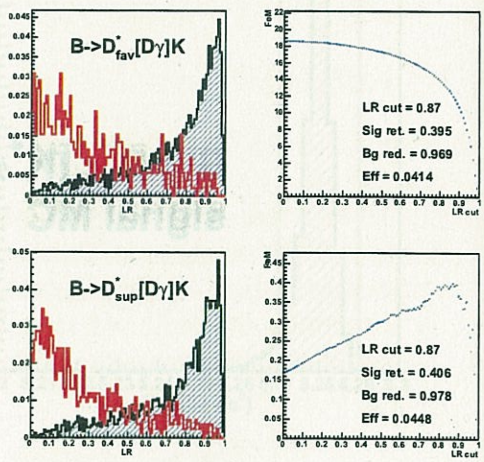

Figure 5.9: Event shape likelihood ratio distribution(left) and The "figure of merit" distribution(right) of $B^- \rightarrow D^*_{fav}[D\gamma]K^-$(top) and $B^- \rightarrow D^*_{sup}[D\gamma]K^-$(bottom)

Mode	#(signal)	#(background)	Expected $\mathcal{B}$	Efficiency(%)
$B^- \to D^*_{fav}[D\pi^0]\pi^-$	12825	136	1.2×10^{-4}	13.8
$B^- \to D^*_{sup}[D\pi^0]\pi^-$	47.4	57	4.2×10^{-7}	14.6
$B^- \to D^*_{fav}[D\pi^0]K^-$	911	48	9.1×10^{-6}	13.0
$B^- \to D^*_{sup}[D\pi^0]K^-$	3.3	121	3.3×10^{-8}	13.0
$B^- \to D^*_{fav}[D\gamma]\pi^-$	10270	487	5.8×10^{-5}	22.9
$B^- \to D^*_{sup}[D\gamma]\pi^-$	37.2	237	2.1×10^{-7}	23.0
$B^- \to D^*_{fav}[D\gamma]K^-$	721	138	4.5×10^{-6}	20.7
$B^- \to D^*_{sup}[D\gamma]K^-$	2.8	343	1.7×10^{-8}	21.4

Table 5.1: Expected number of signal and background events with 366 fb^{-1} data set (386×10^6 $B\bar{B}$ pairs). These efficiencies are ones before event shape variable cut. These numbers of background events are estimated from "uds" and "charm" Monte Carlo events whose size are 532 fb^{-1} corresponding to 3 times events of experimental number 21 to 37(177.4fb^{-1}).

5.1.4 Peaking background

To check the peaking background "generic Monte Carlo" events and "rare Monte Carlo" events are used as shown in Figure 5.10 - 5.13 and Figure 5.14 - 5.17, respectively.

But in signal region particular background source is not found.

5.2 Results

5.2.1 Fitting the ΔE distributions

In $B^- \to D^*_{fav}[D\pi^0]\pi^-$, $B^- \to D^*_{fav}[D\pi^0]K^-$, $B^- \to D^*_{fav}[D\gamma]\pi^-$ and $B^- \to D^*_{fav}[D\gamma]K^-$ decay mode, backgrounds from other B decays distribute as shown in Figure 5.19 - 5.21.

The treatments of background, $B\bar{B}$ background and continuum background, is same as $B^- \to DK^-$ analysis. For fit of signal the sum of two Gaussian distributions which have same mean are used where its relative width and area are determined from signal Monte Carlo.

In the fit of the ΔE distribution for $B^- \to D^*_{fav}h^-$ mode, the free parameters are the position, widths and area of the signal peak, the slope and normalization of the continuum component and the normalization of the $B\bar{B}$ background.

For $B^- \to D^*_{sup}h^-$, the signal and $B\bar{B}$ background shapes are modeled using the results of the fits to the corresponding favored modes. The free parameters are the normalization of the three components, and the slope of the continuum.

The fit results are shown in Figure 5.22 - 5.29. The numbers of signal yield are listed in Table 5.2

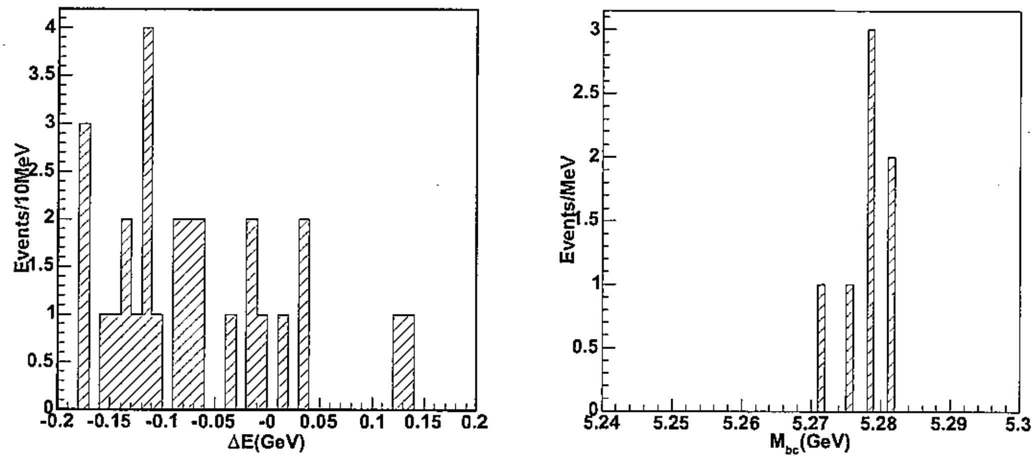

Figure 5.10: ΔE and m_{bc} distributions of "generic Mote Carlo" evnts for $B^- \to D^*_{sup}[D\pi^0]\pi^-$

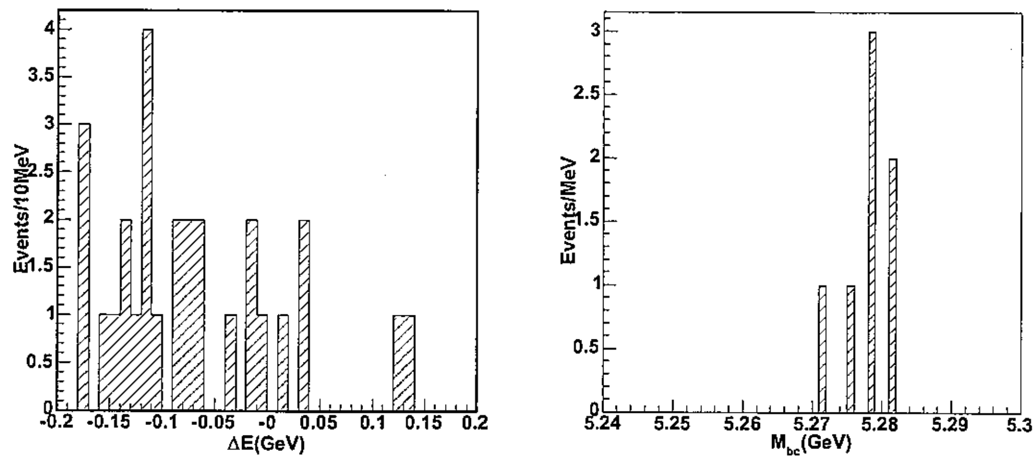

Figure 5.11: ΔE and m_{bc} distributions of "generic Mote Carlo" evnts for $B^- \to D^*_{sup}[D\pi^0]K^-$

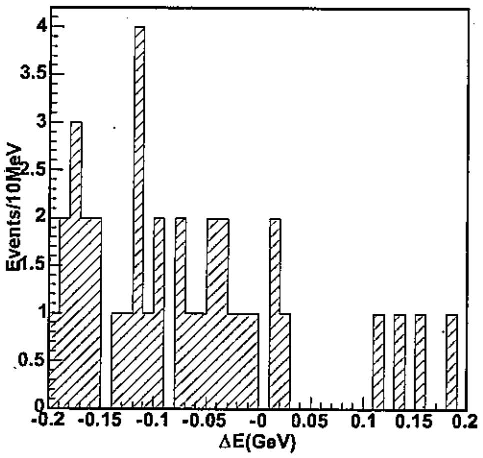

Figure 5.12: ΔE and m_{bc} distributions of "generic Mote Carlo" evnts for $B^- \to D^*_{sup}[D\gamma]\pi^-$

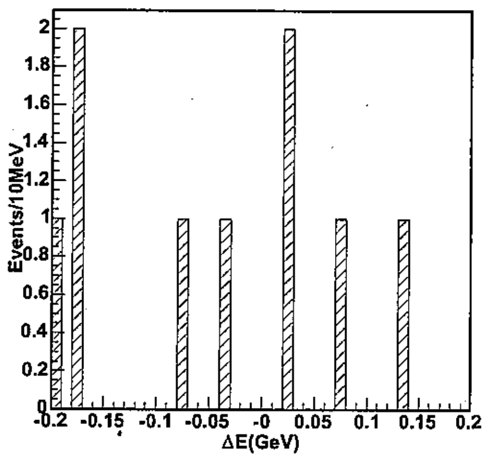

Figure 5.13: ΔE and m_{bc} distributions of "generic Mote Carlo" evnts for $B^- \to D^*_{sup}[D\gamma]K^-$

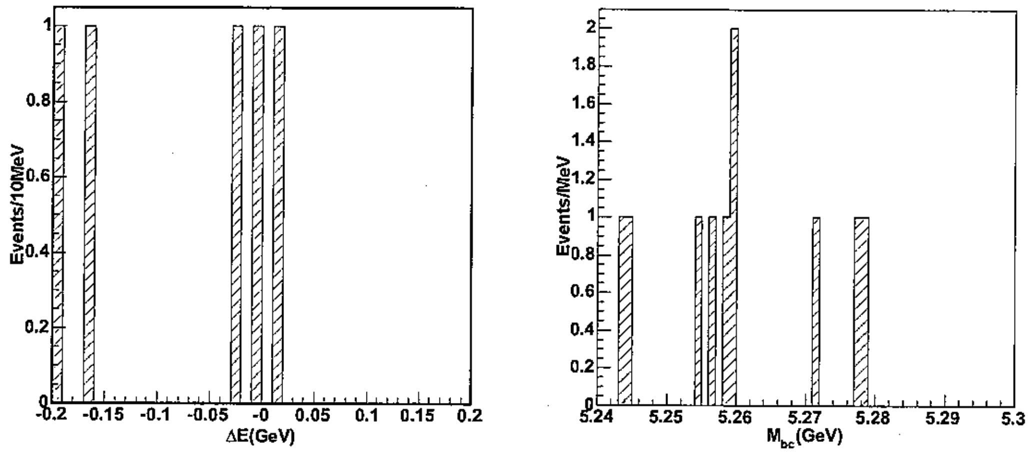

Figure 5.14: ΔE and m_{bc} distributions of "rare Mote Carlo" evnts for $B^- \to D^*_{sup}[D\pi^0]\pi^-$

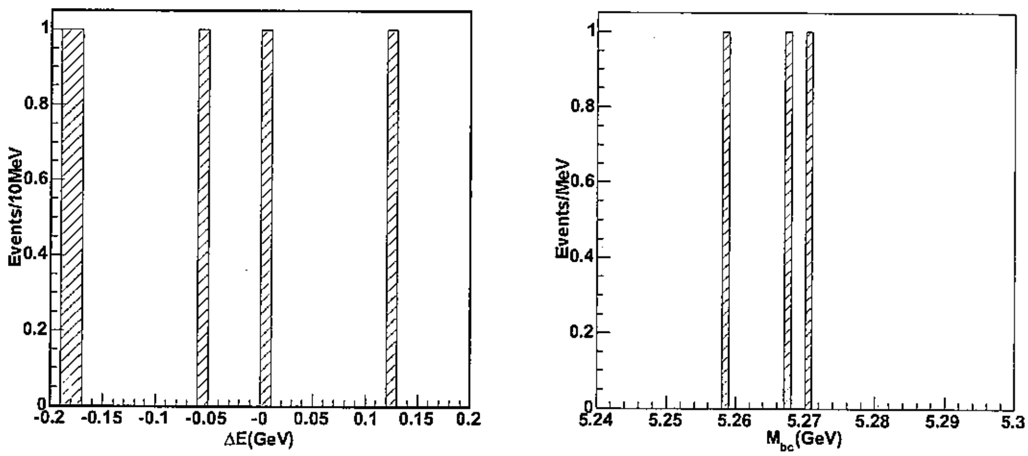

Figure 5.15: ΔE and m_{bc} distributions of "rare Mote Carlo" evnts for $B^- \to D^*_{sup}[D\pi^0]K^-$

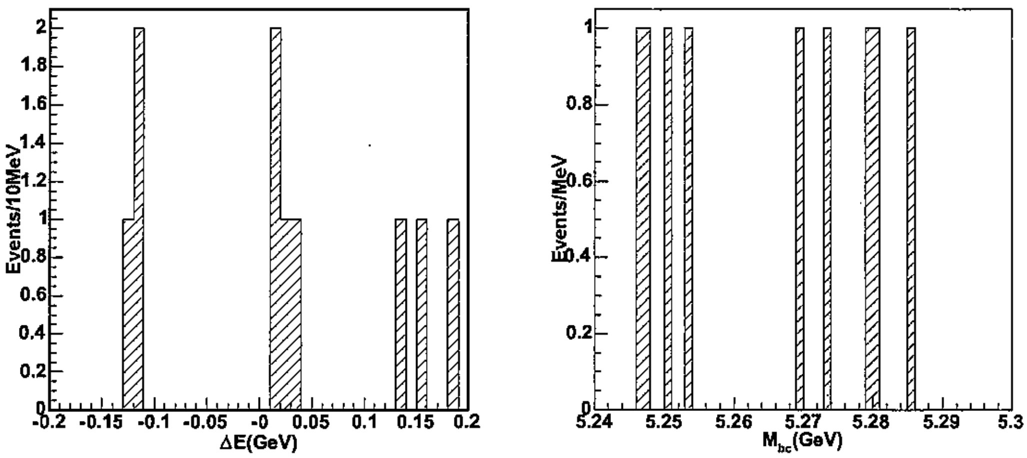

Figure 5.16: ΔE and m_{bc} distributions of "rare Mote Carlo" evnts for $B^- \to D^*_{sup}[D\gamma]\pi^-$

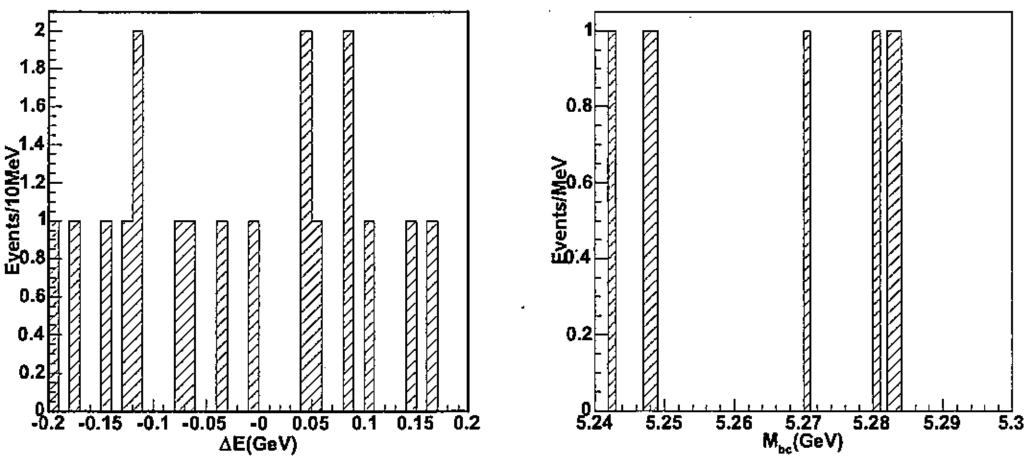

Figure 5.17: ΔE and m_{bc} distributions of "rare Mote Carlo" evnts for $B^- \to D^*_{sup}[D\gamma]K^-$

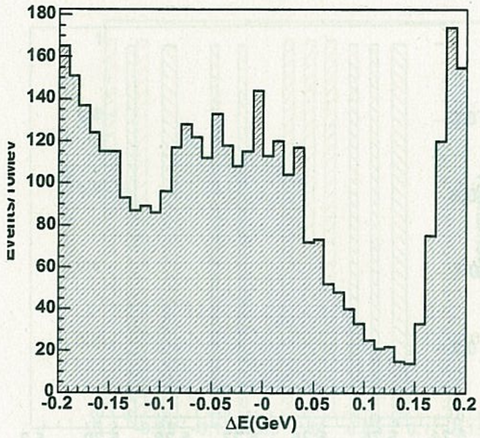

Figure 5.18: ΔE distribution of $B\bar{B}$ background for $B^- \to D^*_{fav}[D\pi^0]\pi^-$

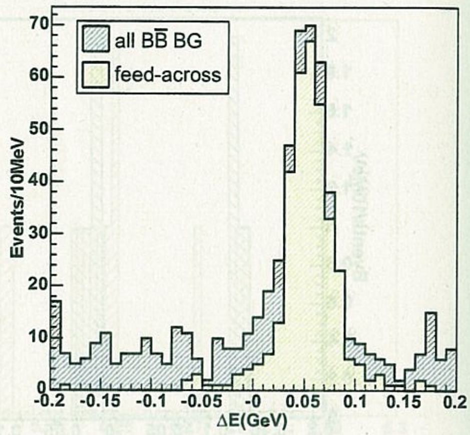

Figure 5.19: ΔE distribution of $B\bar{B}$ background for $B^- \to D^*_{fav}[D\pi^0]K^-$

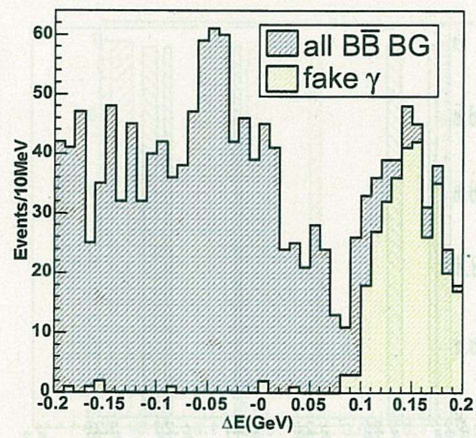

Figure 5.20: ΔE distribution of $B\bar{B}$ background for $B^- \to D^*_{fav}[D\gamma]\pi^-$

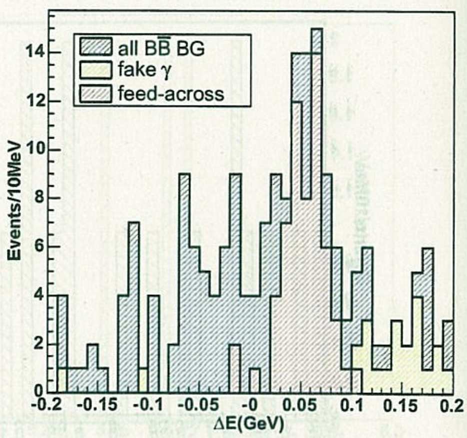

Figure 5.21: ΔE distribution of $B\bar{B}$ background for $B^- \to D^*_{fav}[D\gamma]K^-$

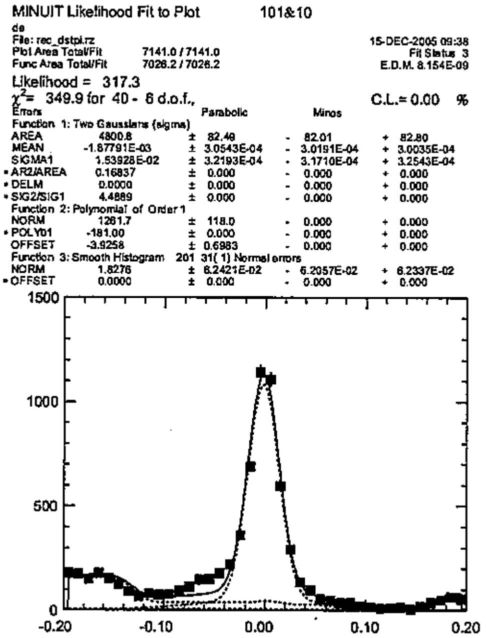

Figure 5.22: $B^- \to D^*_{fav}[D\pi^0]\pi^-$ ΔE-fit result

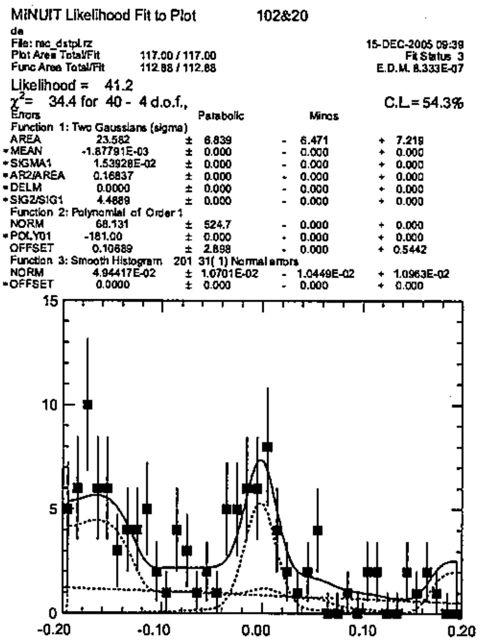

Figure 5.23: $B^- \to D^*_{sup}[D\pi^0]\pi^-$ ΔE-fit result

Mode	Efficiency(%)	Signal Yield
$B^- \to D^*_{fav}[D\pi^0]\pi^-$	10.5 ± 0.2	4801 ± 82
$B^- \to D^*_{sup}[D\pi^0]\pi^-$	11.1 ± 0.2	23.6 ± 6.8
$B^- \to D^*_{fav}[D\pi^0]K^-$	6.9 ± 0.2	176 ± 18.7
$B^- \to D^*_{sup}[D\pi^0]K^-$	7.0 ± 0.2	0.0 ± 0.0
$B^- \to D^*_{fav}[D\gamma]\pi^-$	5.9 ± 0.2	1481 ± 52
$B^- \to D^*_{sup}[D\gamma]\pi^-$	6.1 ± 0.2	4.4 ± 4.2
$B^- \to D^*_{fav}[D\gamma]K^-$	4.1 ± 0.1	43.4 ± 8.9
$B^- \to D^*_{sup}[D\gamma]K^-$	4.5 ± 0.1	2.9 ± 1.8

Table 5.2: Efficiency and signal yields.

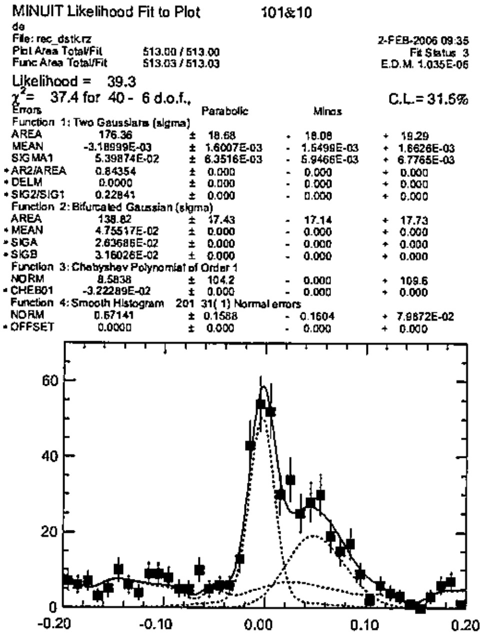

Figure 5.24: $B^- \to D^*_{fav}[D\pi^0]K^-$ ΔE-fit result

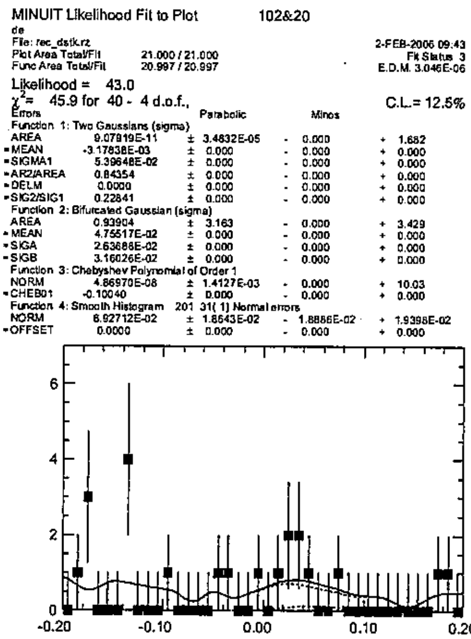

Figure 5.25: $B^- \to D^*_{sup}[D\pi^0]K^-$ ΔE-fit result

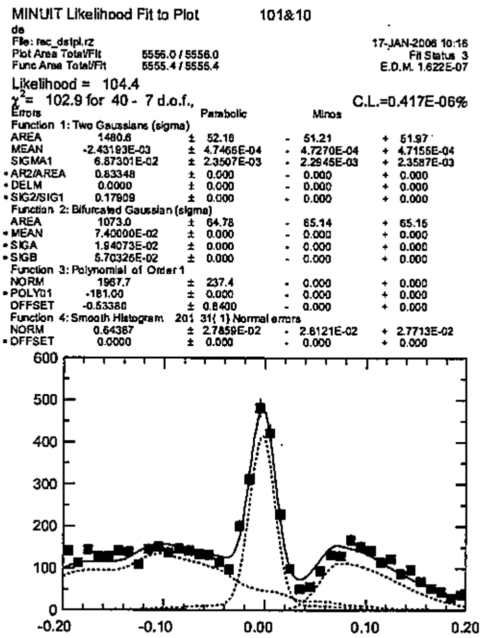

Figure 5.26: $B^- \to D^*_{fav}[D\gamma]\pi^-$ ΔE-fit result

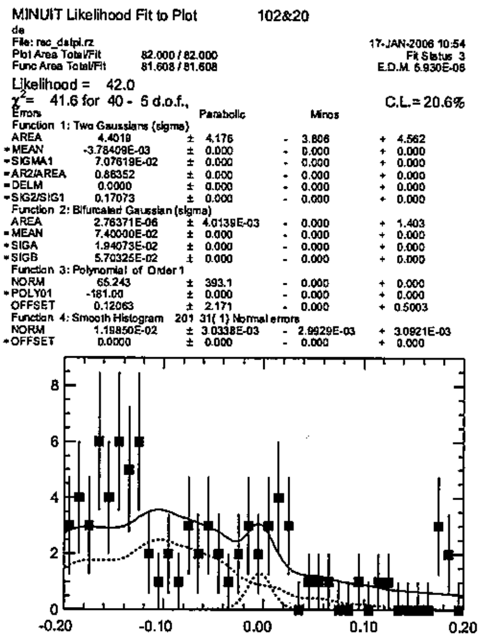

Figure 5.27: $B^- \to D^*_{sup}[D\gamma]\pi^-$ ΔE-fit result

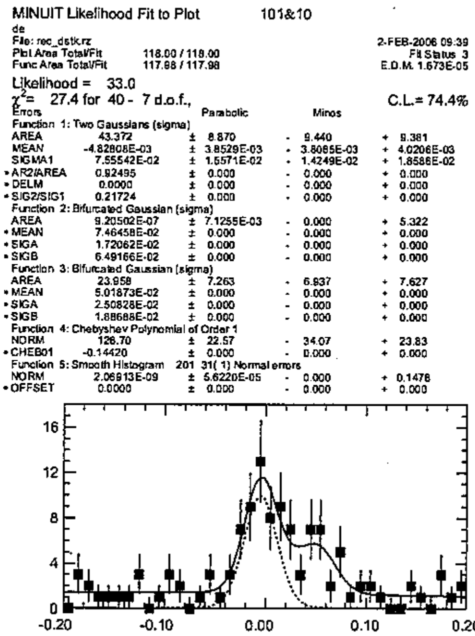

Figure 5.28: $B^- \to D^*_{fav}[D\gamma]K^-$ ΔE-fit result

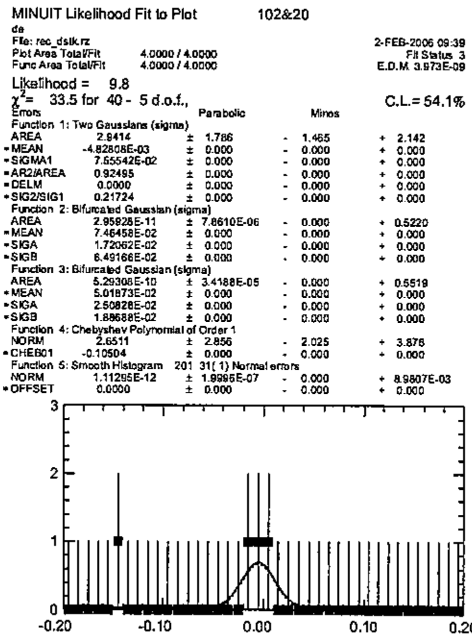

Figure 5.29: $B^- \to D^*_{sup}[D\gamma]K^-$ ΔE-fit result

5.2.2 Ratio of branching fractions R_{Dh}

In $B^- \to D^*K^-$ mode the ratio of product branching fraction defined is calcurated using the numer of signal events and efficiency listed in Table 5.2.

The ratios are obtained as

$$
\begin{aligned}
R_{D^*[D\pi^0]\pi^-} &= (4.6 \pm 1.4(stat)) \times 10^{-3}, \\
R_{D^*[D\pi^0]K^-} &= 0.0 \pm 0.0(stat) \pm 0.0(sys) \\
R_{D^*[D\gamma]\pi^-} &= (2.8 \pm 2.8(stat)) \times 10^{-3}, \\
R_{D^*[D\gamma]K^-} &= (6.7 \pm 4.3(stat)) \times 10^{-2}.
\end{aligned}
$$

In this mode using the identity

$$r^2_{B,D^*K} = \frac{R_{D^*[D\pi^0]K} + R_{D^*[D\gamma]K}}{2} - r^2_D$$

r_{B,D^*K} is calculated as

$$r_{B,D^*K} = 0.17 \pm 0.07(stat) \pm 0.04(sys)$$

The systematic error comes from each yield extractions and is estimated in the same way as $B^- \to DK^-$ analysis.

So the upper limit is set as

$$r_{B,D^*K} < 0.31 \text{ at the 90\% confidence level}$$

5.2.3 Constraint for ϕ_3

Using the value of r_{B,DK^*} and Belle measurement for $B^- \to D^*_{CP}K^-$ as bellow, a constraint for ϕ_3 and δ is determined.

$$A_1 = -0.27 \pm 0.25(stat) \pm 0.04(sys) \quad (5.1)$$

$$A_2 = 0.26 \pm 0.26(stat) \pm 0.03(sys) \quad (5.2)$$

$$R_1 = 1.43 \pm 0.28(stat) \pm 0.06(sys) \quad (5.3)$$

$$R_2 = 0.94 \pm 0.28(stat) \pm 0.06(sys) \quad (5.4)$$

The same method as $B^- \to DK^-$ analysis is used to give a constraint for $\phi - \delta$. The result as shown in Figure 5.30 is obtained.

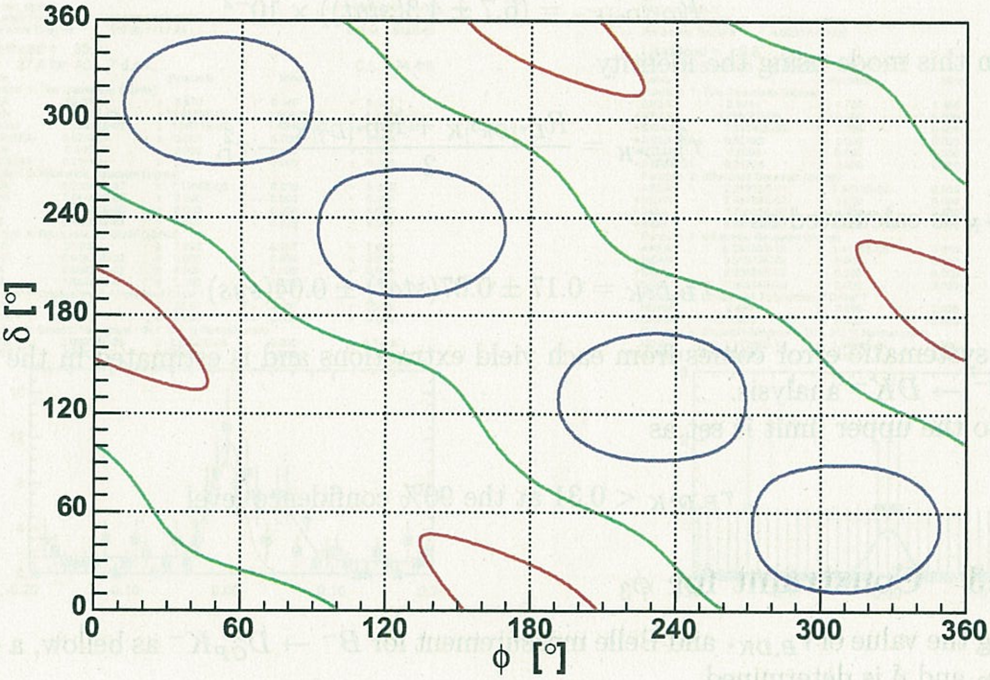

Figure 5.30: Constraint for ϕ_3 and δ

Chapter 6

Conclusions

In this thesis I searched suppressed decay modes such as $B^- \to D_{sup}K^-$, $B^- \to D_{sup}K^{*-}$ and $B^- \to D^*_{sup}K^-$. We can't find any significant signal.

So we set upper limits for $R_{Dh} = \frac{B^- \to D_{sup}h^-}{B^- \to D_{fav}h^-}$ and $r_B = |\frac{B^- \to \bar{D}^0 K^-}{B^- \to D^0 K^-}|$. Using these results and results of $B^- \to D_{CP}K^-$ analysis, we perform constraints for ϕ_3 and r_Bs. Up to now although this method doesn't give a certain constraint for ϕ_3 because of small statistics, the method of ϕ_3 measurement is established. This fact is important.

Appendix A

Cotinuum background suppression

Thrust angle

Firstly we determine the thrust axis which is maximize the projection momentums of daughter particles in signal candidate and the others. Then we calculate the angle between these axes. In the case of $B\bar{B}$ event it distributes flat. On the other hand in the case of $q\bar{q}$ event it makes peak in the edge.

Super Fox-Wolfram method / SFW

Super Fox-Wolfram method are composed of Fisher discriminant with super Fox-wolfram moments. Super Fox-Wolfram moments are defined as

$$H_n \equiv \sum_{i,j} |\vec{p_i}^*||\vec{p_j}^*|P_n(\cos\theta_{ij}) \tag{A.1}$$

where $\vec{p}^*$ is momentum in the CM system, indices distinguish particles in a event, θ_{ij} is a decay angle and P_n is n-th Legendre polynomial.

H_n is decomposed to 3 components expediently

$$H_n \equiv H_n^{ss} + H_n^{so} + H_n^{oo} \tag{A.2}$$

$$H_n^{ss} \equiv \sum_{i,j} |\vec{p_i}^*||\vec{p_j}^*|P_n(\cos\theta_{ij}) \tag{A.3}$$

$$H_n^{so} \equiv \sum_{j,k} |\vec{p_j}^*||\vec{p_k}^*|P_n(\cos\theta_{jk}) \tag{A.4}$$

$$H_n^{00} \equiv \sum_{k,l} |\vec{p_k}^*||\vec{p_l}^*|P_n(\cos\theta_{kl}). \tag{A.5}$$

where i and j represent tracks of signal candidate and k and l represent ones of remaining tracks in a event. In Belle Fisher discriminant is used using six term Fow-Wolfram moments as

$$SFW = \sum_{n=2,4} \alpha_n \frac{H_n^{so}}{H_o^{so}} + \sum_{n=1}^{4} \beta_n \frac{H_n^{oo}}{H_o^{oo}} \tag{A.6}$$

where α_n and β_n are Fisher coefficients which maximize the separation between signal and background. Here H_n for $n > 4$ is not used because of less ability of separation between signal and continuum. And H_1^{so}, H_3^{so} and H_n^{ss} are also not used because of strong correlations with M_{bc} od ΔE.

improved Super Fox-Wolfram method / KSFW

To suppress continuum background effectively KSFW is developed. KSFW is defined as

$$KSFW \equiv \sum_{l=0}^{4} R_l^{so} + \sum_{l=0}^{4} R_l^{oo} + \gamma \sum_{n=1}^{N_t} |p_{t,n}| \tag{A.7}$$

where p_t is transverse momentum, N_t is the number of tracks in a event and γ is Fisher coefficient.

- R_l^{so}
  In this method H_l^{so} is decomposed to 3 components, "charged", "neutral" and "missing" .

$$R_l^{so} \equiv \frac{(\alpha_c)_l (H_{\text{charged}})_l^{so} + (\alpha_n)_l (H_{\text{neutral}})_l^{so} + (\alpha_c)_l (H_{\text{missing}})_l^{so}}{E_{beam} - \Delta E} \tag{A.8}$$

For $l = 1$ and 3,

$$(H_{\text{charged}})_l^{so} \equiv \sum_i \sum_j \beta_l^{so} Q_i Q_j |\vec{p_j}| P_l(\cos\theta_{ij}) \tag{A.9}$$

$$(H_{\text{neutral}})_l^{so} = H_{\text{missing}} = 0 \;(\because \text{Q=0}) \tag{A.10}$$

For $l = 0, 2$ and 4,

$$(H_{\text{charged,neutral,missing}})_l^{so} \equiv \sum_i \sum_j \beta_l^{so} |\vec{p_j}| P_l(\cos\theta_{ij}) \tag{A.11}$$

The index i iterates over the tracks of signal candidate and the index j iterates over same category(charged, neutral or missing) tracks of the rest. Q_i is charge of particle i. In these equation α and β are fisher coefficients. So there are 11 parameters $((l = 0, 3) \times (\text{charged}) + (l = 0, 2, 4) \times (\text{chaged, neutral, missing}) = 2 \times 1 + 3 \times 3)$ in the $R_l^{so} opnimaizetion$

- R_l^{oo}
  For $l = 1, 3$

$$R_l^{oo} \equiv \frac{\sum_j \sum_k \beta_l^{oo} Q_j Q_k |p_j||p_k| P_l(\cos\theta_{jk})}{(E_{beam} - \Delta E)^2} \tag{A.12}$$

  For $l = 0, 2, 4$

$$R_l^{oo} \equiv \frac{\sum_j \sum_k \beta_l^{oo} |p_j||p_k| P_l(\cos\theta_{jk})}{(E_{beam} - \Delta E)^2} \tag{A.13}$$

  In these equation index j and k iterate over the rest tracks of the signal candidate. There are 5 parameters in optimaizatoin.

- $\sum_{n=1}^{N_t} |p_{t,n}|$
  This is the sum of transverse momentum in a event. This has a optimization coefficient.

This method has totally 17 (= 11 + 5 + 1) parameters. And empirically the value of "KSFW" strongly depends on mm^2 defined as

$$mm^2 = (E_{\Upsilon(4S)} - \sum_i E_i)^2 - \sum_i |p_i|^2. \tag{A.14}$$

So in optimization of these parameters mm^2 regions are divided to 7 regions ($-0.5 \sim 6.0$[GeV]).

Appendix B

Figue of merit technique

In physics analysis we need the indicator to optimize a cut value. Figure of merit(F.o.M) is a good indicator. It's defined as

$$F.o.M = \frac{S}{\sqrt{S+N}}$$

,where S is number of signal and N is number of background.

This roughly means the significance of the signal. Because if we get number of total events, $S+N$, its fluctuation is about $\sqrt{S+N}$. So if number of signal is S, its significance is represented as $S/\sqrt{S+N}$. Then by optimization based on this technique we can get signal with higher significance.

For example, let's consider ΔE-fit under the condition as

$$\begin{cases} \text{signal shape} & : & \text{gaussian} \\ \#(signal) & = & 30 \\ \sigma_{signal} & = & 0.01 \\ \text{background shape} & : & \text{constant} \\ \#(background) : N(x) & = & 7 \end{cases}$$

and make ΔE distribution sample using random numbers as Figure B.1.

Actually I do ΔE-fit for this sample and calculate the significance. And changing the integration range of background we know the range which equalize F.o.M to significance. In this sample when we integrate the background within $2.2\sigma_{signal}$ the F.o.M is equal to the signal significance.

To confirm this statically I repeat this process 1000 times as Figure B.2. By this if we integrate the background within 2.3 σ we can get the F.o.M closing to significance.

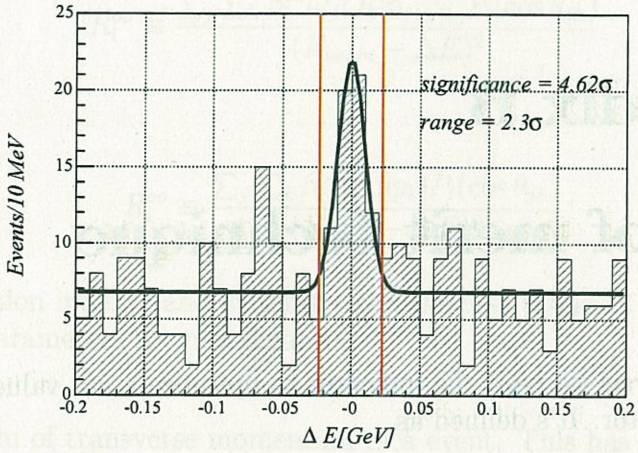

Figure B.1: ΔE distribution using random numbers.

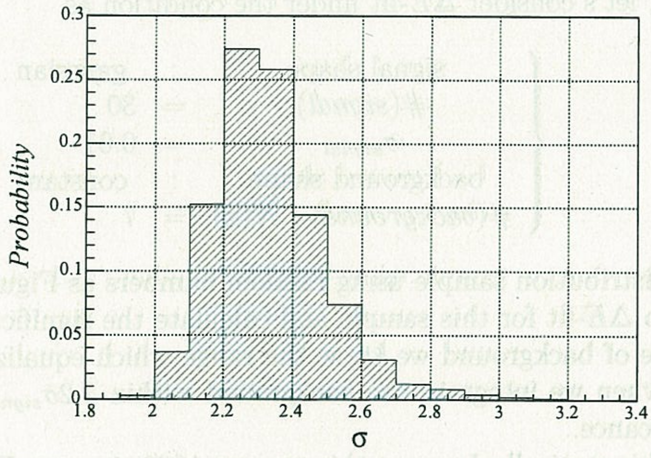

Figure B.2: Integration range of background estimation